

DEFORMATION, FRACTURE, AND HARDNESS CHARACTERISTICS  
OF COMPOUNDS OF MANGANESE WITH GROUP VI ELEMENTS

by

Paul Gordon Riewald

A dissertation submitted in partial fulfillment  
of the requirements for the degree of  
Doctor of Philosophy in  
The University of Michigan  
1968

Doctoral Committee:

Professor Lawrence H. Van Vlack, Chairman  
Professor David K. Felbeck  
Associate Professor William F. Hosford  
Assistant Professor Orville F. Kimball  
Associate Professor Donald R. Peacor



THE UNIVERSITY OF MICHIGAN  
DEPARTMENT OF CHEMICAL AND METALLURGICAL ENGINEERING  
ANN ARBOR, MICHIGAN 48104

June 14, 1968

LAWRENCE H. VAN VLACK  
ADMINISTRATIVE CHAIRMAN  
CHAIRMAN, MATERIALS AND  
METALLURGY

DONALD L. KATZ  
CHAIRMAN, CHEMICAL  
ENGINEERING

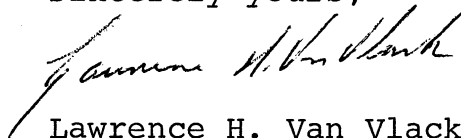
Selenium-Tellurium Development Association, Inc.  
11 Broadway  
New York, New York 10004

Dear Sirs:

The attached is a dissertation by Dr. Paul G. Riewald which was completed in May 1968 for his research work at the University of Michigan. Dr. Riewald received no personal support from the Selenium-Tellurium Development Association. However, the subject of his research was very closely associated with the sponsored work by the Selenium-Tellurium Development Association at the University of Michigan as it pertains to manganese selenide and manganese telluride and their possible use as additives to steels for free-machinability. Consequently, Dr. Riewald has agreed to permit his dissertation to become available to members of the Selenium-Tellurium Development Association. Funds for its reproduction were borne by the Association's grant to The University of Michigan. Because the enclosed material is a dissertation, it is proper that Dr. Riewald should be consulted before using it for other purposes; however, he has indicated his willingness to grant that permission freely.

As Chairman of the Department of Chemical and Metallurgical Engineering and as Chairman of Dr. Riewald's dissertation committee, I would like to solicit reactions from each of you in connection with the subject matter that is presented herein. In due course, it is anticipated that much of the material in this dissertation will be submitted for publication. We will try to make those papers available to the Selenium-Tellurium Development Association and its members.

Sincerely yours,



Lawrence H. Van Vlack  
Professor and Chairman

LHVV/ac  
Enclosure





Pages ii and iii not reproduced in this report.



## TABLE OF CONTENTS

	Page
LIST OF TABLES	vii
LIST OF FIGURES	viii
ABSTRACT	xiii
CHAPTER	
I. INTRODUCTION	1
II. LITERATURE REVIEW	3
A. Deformation and Fracture of Nonmetallics	3
1. Deformation and Fracture Mechanisms	4
2. Cohesive Strength	7
3. Plasticity	8
4. Fracture	13
B. Hardness and Hardness Testing	17
1. Vickers Hardness	18
2. Knoop Hardness	19
C. Pertinent Information on MnO, MnS, MnSe, and MnTe	21
1. Structure and Phase Relations	21
2. Other Properties	23
III. EXPERIMENTAL PROCEDURE	29
A. Raw Materials	29
B. Materials Purification	32
C. Crystal Growth	35
1. Pure Compounds	35
2. Binary Compositions	36
D. Sample Preparation	37
1. Orienting and Cutting	37
2. Mounting and Polishing	37
E. Testing and Examination Procedure	38
1. Deformation	38
2. Fracture	40
3. Temperature Effect	40
4. Low Temperature X-ray Study	42

## TABLE OF CONTENTS (Continued)

CHAPTER	Page
IV. EXPERIMENTAL RESULTS	44
A. Manganous Selenide	44
1. Plastic Deformation	44
2. Fracture	55
B. The System MnSe-MnS	57
1. Plastic Deformation	57
2. Fracture	62
3. Diamond Pyramid Hardness	64
4. Knoop Hardness	70
C. MnSe-Rich Portion of MnSe-MnTe System	77
1. Plastic Deformation	77
2. Fracture	77
3. Diamond Pyramid Hardness	77
4. Knoop Hardness	79
D. Manganous Telluride	79
1. Plastic Deformation	79
2. Fracture	85
E. MnTe-Rich Portion of MnSe-MnTe System	87
1. Plastic Deformation	87
2. Fracture	87
3. Diamond Pyramid Hardness	87
4. Knoop Hardness	88
V. DISCUSSION	89
A. Deformation Associated with the Vickers Indentation	89
B. Comparison of Deformation, Fracture, and Hardness Characteristics of Mn(Group VI) Compounds	94
C. Knoop Hardness Indentations on Anisotropic Materials	97
1. Data Available	97
2. Scope of the Problem	104
3. Treatments of Problem	106
4. Results	115
VI. CONCLUSIONS	123
APPENDIX	
I. TABULATION OF HARDNESS DATA	127
II. SUMMARY OF KNOOP HARDNESS ANISOTROPY THEORIES	131
1. Daniels and Dunn Method	131
2. Feng and Elbaum Method	131

## TABLE OF CONTENTS (Concluded)

	Page
3. One Shear Stress Method	131
4. Two Shears Method	133
5. Integrated Average Method	138
III. OTHER SYSTEMS INVESTIGATED	140
1. MnTe-MnS System	140
2. MnSe-FeSe System	140
3. MnSe-CrSe System	141
4. MnS-FeS System	141
5. MnS-CrS System	142
REFERENCES	143

## LIST OF TABLES

Table	Page
I. Knoop Hardness of MnSe	71
II. Knoop Hardness of MnS	71
III. Properties of Mn (Group VI) Compounds	96
IV. Cation-Anion Distances in Mn(Group VI) Compounds	97
V. Knoop Hardness Data for FCC and BCC Metals and MnSe	99
VI. Knoop Hardness Data for NaCl-Type Materials which Deform by $\{110\}\langle\bar{1}\bar{1}0\rangle$ Slip	100
VII. Knoop Hardness Calculations for $\{111\}\langle\bar{1}\bar{1}0\rangle$ Slip	116
VIII. Knoop Hardness Calculations for $\{110\}\langle\bar{1}\bar{1}0\rangle$ Slip	117

## LIST OF FIGURES

Figure	Page
1. Variation of yield stress with temperature for ionic crystals.	11
2. Diagram of the NiAs-type structure of MnTe.	22
3. Phase diagram of the system MnO-MnS.	24
4. Phase diagram of the system MnSe-MnS.	24
5. Phase diagram of the system MnTe-MnS.	25
6. Phase diagram of the system MnSe-MnTe.	25
7. Antiferromagnetic structure of MnO.	26
8. Apparatus used for the preparation of stoichiometric manganese sulfide.	30
9. Zone refining apparatus for the purification of manganese selenide and manganese telluride.	33
10. Technique used for hardness testing at $-196^{\circ}\text{C}$ , $-70^{\circ}\text{C}$ , and $135^{\circ}\text{C}$ .	41
11. Apparatus used to obtain low temperature X-ray powder patterns of manganese selenide.	43
12. Slip traces around Vickers indentation on the (001) surface of MnSe.	45
13. Slip traces around Knoop and Vickers indentations on the (011) surface of MnSe.	45
14. Slip traces around Vickers indentation on the (111) surface of MnSe.	46
15. Two cubic unit cells showing several low index planes and their intersections with other planes.	46
16. The (001) surface of MnSe showing cross slip on {110} planes.	48
17. Examples of Vickers impressions of unusual shapes on (a) the (001) and (b) the (011) surfaces of MnSe.	48

LIST OF FIGURES (Continued)

Figure	Page
18. Interference micrographs around Vickers indentations on the (001) surface of MnSe when the indenter diagonals are in (a) $\langle 100 \rangle$ and (b) $\langle 110 \rangle$ directions.	50
19. Concentration of slip lines around Vickers indentation on the (001) surface of MnS.	52
20. Interference micrographs around Vickers indentations on the (001) surface of MnS when the indenter diagonals are in (a) $\langle 100 \rangle$ and (b) $\langle 110 \rangle$ directions.	53
21. $\{100\}$ fracture around Vickers indentation on the (001) surface of MnSe.	56
22. Dislocation etch pits reflecting dislocations nucleated at the tip of a $\{100\}$ cleavage crack.	56
23. $\{111\}$ and $\{110\}$ slip traces around Vickers indentation on the (001) surface of 75 MnSe—25 MnS single crystal.	58
24. $\{111\}$ and $\{110\}$ slip traces around Vickers indentation on the (001) surface of 50 MnSe—50 MnS single crystal.	58
25. $\{111\}$ and $\{110\}$ slip traces around Vickers indentation on the (001) surface of 50 MnSe—50 MnS single crystal with $\{100\}$ cracking evident.	58
26. $\{111\}$ and $\{110\}$ slip traces around Vickers indentation on the (001) surface of 25 MnSe—75 MnS single crystal.	60
27. $\{111\}$ and $\{110\}$ slip traces around Vickers indentation on the (011) surface of 25 MnSe—75 MnS single crystal.	60
28. $\{110\}$ slip traces around Vickers indentation on the (001) surface of MnS.	60
29. $\{110\}$ slip traces around Vickers indentation on the (011) surface of MnS.	60
30. Dislocation etch pit rosette pattern on the (001) plane for MnS.	61



LIST OF FIGURES (Continued)

Figure	Page
31. Development of dislocation etch pit rosette pattern characteristic of $\{110\}\langle\bar{1}\bar{1}0\rangle$ slip around Vickers indentations for MnSe-MnS solid solutions.	63
32. Average diamond pyramid hardness of MnSe-MnS solid solutions at various temperatures.	65
33. Diamond pyramid hardness vs. temperature for MnSe-MnS solid solutions.	67
34. $\{111\}$ and $\{110\}$ slip traces around Vickers indentation on the (001) surface of MnS when tested under liquid nitrogen.	68
35. The (001) surface of MnSe after quenching in liquid nitrogen.	68
36. Room temperature Knoop hardnesses on (001) for MnSe-MnS solid solutions.	72
37. Room temperature Knoop hardnesses on (011) for MnSe-MnS solid solutions.	73
38. Knoop hardnesses on (001) for MnSe-MnS solid solutions at $-70^{\circ}\text{C}$ .	75
39. Knoop hardnesses on (001) for MnSe-MnS solid solutions at $135^{\circ}\text{C}$ .	76
40. Slip traces around Vickers indentation on the (001) surface of 93 MnSe—7 MnTe single crystal.	78
41. Slip traces around Knoop indentation on the (011) surface of 93 MnSe—7MnTe single crystal.	78
42. Slip traces around Vickers indentation on the (011) surface of 87 MnSe—13 MnTe single crystal.	78
43. Diamond pyramid hardnesses for MnSe-MnTe solid solutions.	80
44. Knoop hardnesses for MnSe-MnTe solid solid solutions.	81
45. Twinning around Vickers indentation on the (0001) surface of MnTe.	83

LIST OF FIGURES (Continued)

Figure	Page
46. Twinning around Knoop indentation on the (0001) surface of MnTe.	83
47. Possible orientations of $\{10\bar{1}2\}$ twin traces in the basal plane of MnTe.	84
48. Interference micrograph around Vickers impression on the (0001) surface of MnTe.	84
49. Slip traces around Vickers indentation on the $(11\bar{2}0)$ surface of MnTe.	86
50. Slip traces around Knoop impressions on the $(10\bar{1}0)$ surface of MnTe when the long axis of the indenter is in (a) the $[\bar{1}2\bar{1}0]$ and (b) the $[0001]$ directions.	86
51. View of a $\{111\}$ plane showing how flow in two $\langle 110 \rangle$ directions can result in net $\langle 112 \rangle$ flow.	90
52. (a) Dislocation or slip interaction on two adjacent $\{110\}$ planes. (b) Dislocation or slip interaction on two adjacent $\{111\}$ planes.	92
53. Comparison of Knoop hardness anisotropy behavior for several materials with cubic crystal structures.	101
54. (a) Orientation of $\{110\}$ planes. (b) View in $[00\bar{1}]$ direction with Knoop indenter in $[100]$ .	103
55. (a) Orientation of $\{111\}$ planes. (b) View in $[00\bar{1}]$ direction with Knoop indenter in $[110]$ .	103
56. (a) Orientation of $\{111\}$ planes with respect to $(1\bar{1}0)$ plane. (b) Edge view of the $(1\bar{1}0)$ plane with intersecting $\{111\}$ planes.	105
57. Diagram of Knoop indenter showing positions of force, slip plane, slip direction and axes of rotation for (A) Daniels and Dunn and (B) Feng and Elbaum methods of analysis.	107
58. Slip line field associated with the plane strain indentation of an isotropic material by an infinite wedge of included angle $130$ degrees.	110

## LIST OF FIGURES

Figure	Page
59. Standard (001) stereographic projection of a cubic crystal showing the shear stress direction and the intersection of the facets of the Knoop indenter with the plane of projection when the long axis is in the [010] direction for the "one lateral shear" method of analysis.	112
60. Standard (001) stereographic projection of a cubic crystal showing the assumed shear stress directions for facet 1 and the intersection of the Knoop indenter with the plane of the projection for the "two shears" method of analysis when the long indenter axis is in the [010] direction.	114
61. Comparison of calculated and measured Knoop hardnesses on single crystals of manganese selenide, aluminum, and silicon ferrite using the "two shears" method of analysis.	119
62. Comparison of calculated and measured Knoop hardnesses on single crystals of manganese selenide, aluminum, and silicon ferrite using the "integrated average" method of analysis.	120
63. Comparison of various methods of estimating Knoop hardness anisotropy on cubic single crystals using manganese selenide as standard.	121
64. Assumed slip line field around indenter and direction of shear stress for the "one lateral shear" method of calculation.	132
65. Stereographic projection illustrating calculational procedure for "one lateral shear" method.	132
66. Assumed slip line field around indenter and directions of shear stress for the "two shears" method of calculation.	134
67. Stereographic projection illustrating calculational procedure for "two shears" method.	134
68. Diagram of slip line field used as an aid to calculate the work done during the indentation of an isotropic material by an infinite wedge.	137
69. Hodograph for the indentation of an isotropic material by an infinite wedge of included angle 130 degrees.	137
70. Plot of minimum (1/m) vs. orientation of shear stress for the "integrated average" method of analysis.	139

## ABSTRACT

This investigation is concerned with the determination of slip mechanisms, fracture characteristics, and hardness relationships of compounds of manganese with Group VI elements. These compounds include MnO, MnS, MnSe, and MnTe, although the emphasis of this study is on MnSe, MnTe, and solid solutions in the systems MnSe-MnS and MnSe-MnTe.

Single crystals were grown by a Bridgman technique, oriented by the back-reflection Laue method and sectioned parallel to selected planes. The selected surfaces were then polished and indented with either a Vickers or Knoop diamond micro-indenter. This testing method was chosen because it was well suited to the size of the crystals utilized and readily provides information on plastic deformation and fracture mechanisms as well as on hardness. Plastic deformation mechanisms were studied by observing (1) slip traces around indentations, (2) the formation of dislocation etch pit rosette patterns, and (3) the Knoop hardness anisotropy associated with single crystal specimens. Fracture was studied by observation of cleavage planes and slip interactions around indentations. Tests were made over the temperature range  $-196^{\circ}\text{C}$  to  $135^{\circ}\text{C}$ .

Sodium chloride-type MnSe exhibits  $\{111\}\langle\bar{1}\bar{1}0\rangle$  and  $\{110\}\langle\bar{1}\bar{1}0\rangle$  as primary and secondary slip mechanisms respectively, in contrast to the  $\{110\}\langle\bar{1}\bar{1}0\rangle$  mechanism preferred by MnS and MnO. As with MnO and MnS, the primary and secondary cleavage planes for MnSe are  $\{100\}$  and  $\{110\}$  respectively. Around surface indentations MnSe shows primarily  $\{100\}$  fracture due to dislocation interactions on  $\{111\}$  slip planes in contrast to  $\{110\}$  fracture in MnS resulting from dislocation interactions on  $\{110\}$  planes.

Around Vickers indentations on MnSe and MnS, a crystallographic pile-up of material occurs which is related to flow on the crystal slip systems. While the appearance of the pile-up is similar in both MnSe and MnS, the mechanisms are different due to the different slip modes.

In the continuous solid solution system MnSe-MnS, the primary slip mechanism changes gradually with composition. Manganese selenide is much softer than manganese sulfide. Substitution of sulfide for selenide ions in MnSe results in a large positive solid solution hardening deviation. The  $\{110\}\langle\bar{1}\bar{1}0\rangle$  slip mechanism of MnS hardens much more rapidly with decreasing temperature than the  $\{111\}\langle\bar{1}\bar{1}0\rangle$  mechanism of MnSe. At liquid nitrogen temperature MnS shows an appreciable amount of  $\{111\}$  slip.

Manganese telluride, with the hexagonal NiAs-type structure, shows three modes of plastic deformation around Vickers and Knoop indentations: (1)  $\{10\bar{1}2\}$  twinning, (2) basal glide, and (3) pencil glide in  $\langle 11\bar{2}0\rangle$ . Primary and secondary cleavage planes are  $\{0001\}$  and  $\{10\bar{1}0\}$  respectively.

The Knoop indentation hardness varies with crystal orientation in a different manner for MnSe than for MnS. A rigorous analysis of Knoop hardness anisotropy and the flow of material associated with the indenter is an extremely complex problem which was not satisfactorily solved in this study. However, a theory is postulated which improves for FCC and BCC metals on the only known published attempt at analysis—that of Daniels and Dunn.

The changes in deformation, fracture, and hardness characteristics in Mn(Group VI) compounds are relatable to changes in other properties, and result from a regular decrease in the ionic character of the chemical bond in going from MnO to MnTe.



## CHAPTER I

### INTRODUCTION

This investigation was undertaken to determine plastic deformation mechanisms, fracture characteristics, and hardness relations among compounds of manganese with Group VI elements, both for the pure compounds and, where possible, for binary substitutional solid solutions. The compounds include MnO, MnS, MnSe, and MnTe although the emphasis of this work was on MnSe, MnTe, and solid solutions in the systems MnSe-MnS and MnSe-MnTe.

Such a study allows one to compare mechanical behavior to other material properties in a series of compounds in which the anion shows a systematic variation. Also, it serves as a first step in a much broader investigation on the role of these compounds, when present as inclusions in metal, on the plastic deformation behavior of the metal matrix (e.g., as in free machining steels).

A Vickers or Knoop micro-indentation hardness procedure on single crystal specimens was chosen as the principal testing method because it is well suited to the size of the crystals utilized and readily provides information on plastic deformation and fracture mechanisms as well as on hardness.

The results for each compound or solid solution system are presented in the following manner: (1) plastic deformation (slip) mechanisms, (2) fracture characteristics (due both to cleavage and slip interaction), (3) diamond pyramid (Vickers) hardness, and (4) Knoop hardness. Results are supplemented with photomicrographs and plots.

Finally, observations are rendered concerning the nature of plastic flow around and adjacent to the Vickers indenter, and attempts are made in an effort to explain the anisotropy associated with Knoop hardness tests on single crystals.



## CHAPTER II

### LITERATURE REVIEW

The following literature review summarizes previous work related to this thesis topic. It is divided into three main sections. The first covers the deformation and fracture of nonmetallic materials, while the second gives a review of hardness and hardness testing. The third section provides pertinent information on the materials considered in this investigation, namely MnO, MnS, MnSe, and MnTe.

#### A. Deformation and Fracture of Nonmetallics

Within the area of deformation and fracture of inorganic nonmetallic materials, the mechanical behavior of ionic crystals has been the most extensively studied and is probably known in greater detail than for any other crystal type (Gilman, 1961a, 1963). One reason for the relatively good understanding of ionic crystals is the simple nature of their chemical bond. Also, they can be readily cleaved to simple shapes and can be easily studied by means of direct observations of their dislocations (Gilman, 1961a).

Because the materials used in this study are predominately ionic and because MnO, MnS, and MnSe possess the NaCl-type structure on which most of the previously reported work has been concentrated, much of the following will be devoted to NaCl-type ceramic materials.

## 1. DEFORMATION AND FRACTURE MECHANISMS

Plastic deformation in crystals generally occurs by slip or twinning. Slip occurs by the relative movement of planes of atoms or ions on a slip plane  $\{hkl\}$  by the propagation of linear defects or dislocations in a slip direction  $\langle uvw \rangle$ . Deformation by twinning consists of shearing movements of the atomic planes over one another so that the twinned and untwinned portions of the crystal are joined together with a definite mutual orientation. The twinned portion is either a mirror image of the orientation of the parent crystal in a plane called the twinning plane, or related by a rotation about an axis called the twinning axis, or both (Barrett, 1952).

Rock salt-type ionic crystals usually deform by translation gliding on  $\{110\}$  planes in  $\langle 1\bar{1}0 \rangle$  directions, which are the shortest translation vectors of the crystal structure and do not require like charged ions to pass over each other (Gilman, 1961a). The  $\{110\}$  planes are favored over the more widely spaced  $\{100\}$  planes probably because glide on  $\{100\}$  is accompanied by electrostatic faulting as first explained by Buerger (1935).

Buerger (1935) and Tammann and Salge (1927) report  $\{111\} \langle 1\bar{1}0 \rangle$  as a secondary slip system in the sodium halides at higher temperatures. Chao et al. (1964a) found that  $\{111\} \langle 1\bar{1}0 \rangle$  was a secondary slip system in MnS when indented with a Vickers diamond at room temperature. Moore (1965), however, did not detect  $\{111\}$  slip around Vickers indentations in MnO.

At high temperatures, most rock salt-type crystals glide readily on  $\{100\}$  planes. Some crystals such as PbS and PbTe show  $\{100\} \langle 011 \rangle$  slip at room temperature (Buerger, 1935; Gilman, 1961a). This is due to their high ionic

polarizability and shows that there is a tendency toward more {100} slip as the ionic character of the bonding decreases.

Silver chloride and silver bromide often show little preference for any glide plane (Gilman, 1961a; Nabarro, 1964). Instead, slip appears to take place upon any plane of which the slip direction is zone axis. This is called pencil glide (Cottrell, 1953; Groves and Kelly, 1963).

Uranium carbide (Van Der Walt and Sole, 1967) and titanium carbide (Williams and Schaal, 1962; Hollox and Smallman, 1966; Van Der Walt and Sole, 1967) have the NaCl-type structure but slip primarily on {111} planes. The bond in these appears to be largely a combination of metallic and covalent as evidenced by their high melting points and good electrical conductivity.

Van Der Walt and Sole (1967) have attempted to explain the deformation of all crystals with the NaCl structure. They conclude that the behavior of ionic crystals is controlled by the electrostatic nature of their bonding, but that the behavior of covalent crystals is directly related to the metallic-nonmetallic radii ratio. Crystals with  $r/R < 0.414$  slip on {110}; for  $0.414 < r/R < 0.633$ , slip is on {111} and for  $r/R > 0.633$ , slip occurs on {100}.

Fracture occurs most easily for NaCl-type crystals by cleavage on {100} (Gilman, 1961a). Van Zeggeren and Benson (1957) calculated the surface energy of {100} to be lower than {110}. Secondary cleavage planes are {110} although no {111} cleavage has been reported (Gilman, 1961a, 1963).

Chao et al. (1964a) found that {100} cleavage is predominant in MnS but that the {110} fracture system becomes primary around surface indentations.

Such fracture develops by interaction of  $(01\bar{1})$  and  $(10\bar{1})$  slip near the  $(001)$  surface by a mechanism first proposed by Keh (1959, 1960). Chao et al. (1964a) also noted that minor amounts of  $\{110\}$  fracture can occur through the interaction of dislocation movements on the  $\{111\}$  slip planes. MnO also cleaves preferentially on  $\{100\}$  and shows  $\{110\}$  cracks normal to  $\{100\}$  around Vickers indentations (Moore, 1965).

Of the many nonmetallics not possessing a NaCl-type structure, the one material most extensively studied with regard to deformation mechanism has probably been alumina, which has a hexagonal structure. Wachtman and Maxwell (1954, 1957, 1959) found that above  $900^\circ\text{C}$ , creep can occur on the  $\{0001\}\langle 11\bar{2}0\rangle$  system. The  $\langle 11\bar{2}0\rangle$  directions in  $\text{Al}_2\text{O}_3$  are taken in the direction of close packing of interstitial holes at  $30$  degrees to a row of closely packed oxygen ions. Kronberg (1957) also found that slip occurred in  $\text{Al}_2\text{O}_3$  on  $\{0001\}\langle 11\bar{2}0\rangle$  at high temperatures. He also reported that basal twinning could be induced by mechanical deformation. Conrad (1965) found that, in the range  $1000\text{--}2000^\circ\text{C}$ , sapphire deforms plastically in tension, compression, and bending by basal slip, and that twinning occurs on  $\{0\bar{1}11\}$  when compressed. Fracture generally occurred on a  $\{0\bar{1}11\}$  twinning plane. Slip has also been found to occur above  $2000^\circ\text{C}$  on the system  $\{1\bar{2}10\}\langle 10\bar{1}0\rangle$  (Klassen et al., 1942).

Some other materials which have been investigated and for which deformation mechanisms have been identified are  $\text{SiO}_2$  (Bailey et al., 1958), diamond (Nabarro, 1964), InSb (sphalerite structure) (Nabarro, 1964),  $\text{CaF}_2$  ( $\text{CaF}_2$  structure) (Phillips, 1961; Burn and Murray, 1962),  $\text{TiO}_2$  ( $\text{SnO}_2$  structure) (Wachtman and Maxwell, 1957; Ashbee and Smallman, 1963), and CsBr (CsCl structure) (Johnson and Pask, 1964).

## 2. COHESIVE STRENGTH

The chemical binding energy of a crystal determines its maximum theoretical strength limit. A convenient measure of the chemical bond strength of crystals is provided by their elastic moduli (Gilman, 1963). Tests have shown that the cohesive strength equals about ten percent of the modulus. This is an order of magnitude greater than the highest strengths which have been observed (Stokes, 1962).

An important relationship is that between cohesive stress and interatomic spacing. This arises because the primary cause of binding is electrostatic attraction—a fact which is especially clear in ionic crystals where about 90 percent of the binding energy results from the electrostatic attraction of oppositely charged ions. The two factors most important in determining interatomic spacing are atom size and chemical valence (Gilman, 1961a, 1963). Indeed, Gilman (1963) shows that, for several types of binding and crystal structures, elastic moduli are very sensitive to interatomic spacing, often inversely proportional to the fourth power of interatomic distance. High strength is always associated with high valence and short interatomic distance.

Gilman (1963) has also shown an exponential relation between hardness and elastic modulus for covalent and metallic crystals. In both cases, the hardness is proportional to the elastic modulus, but the proportionality constants differ by a factor of 500, giving some evidence that cohesion may be strongly affected by dislocations (Gilman, 1961b). For metals, in which dislocations can move easily, the hardness is a small fraction of the modulus (about 0.5 percent), while in covalent crystals, it amounts to around 10 percent of the

modulus (Gilman, 1963). This is close to their cohesive strength and indicates that dislocations have great difficulty in moving through covalent crystals.

The effect of increased temperature in lowering the elastic modulus is quite marked and has been investigated by a number of authors (Durand, 1936; Galt, 1948; Hunter and Siegel, 1942; Stephanov and Eidus, 1956; Tannhauser et al., 1956).

Also, internal defects such as grain boundaries, cracks, and inclusions disrupt the normal short range binding and drastically lower the strength of ionic crystals (Gilman, 1963).

### 3. PLASTICITY

Characteristically, ionic crystals are brittle (Gilman, 1963). However, when natural dislocation sources are reduced by annealing and when surface defects are removed by chemical polishing, ionic crystals can undergo appreciable plastic flow before fracture (Stokes, 1962). Indeed, Gorum et al. (1958) found that FCC and BCC ionic materials are inherently ductile rather than brittle. The greatest ductility and plastic deformation is associated with NaCl-type ionic crystals and it is on this variety that most studies have been performed.

#### a. Dislocation Mechanisms

It has been proved beyond any reasonable doubt that plastic deformation in crystals takes place through the motion of dislocation lines (Gilman, 1961a). The macroscopic deformation of a crystal is governed by three factors: (1) how many dislocations are in motion, (2) their average velocity, and (3) their individual effect (i.e., Burger's vector) (Miles, 1964).

Very large numbers of dislocations are needed to obtain sizable macroscopic strains, and these large numbers of dislocations are not often initially present in the crystal but must be formed during the plastic deformation process. Crystals grown under ordinary circumstances usually contain grown-in dislocations which, as Stokes (1962) found in MgO, are quite immobile and play a passive role in most deformation processes. Dislocations can be formed homogeneously by the action of stress alone, but this process is expected to occur only at very high stresses. In real crystals, small precipitates or other discontinuities can act as stress raisers and cause heterogeneous dislocation nucleation (Gilman, 1959b). Even heterogeneous nucleation cannot account for the vast bulk of dislocations that finally participate in a large plastic deformation. These appear to be formed through regenerative multiplication by either the Frank-Read (1950) mechanism or by a multiple cross glide mechanism first proposed by Koehler (1952) and Orowan (1954). In the case of LiF, there is good evidence that the multiple cross glide process provides most of the dislocation multiplication that occurs during plastic straining (Johnston and Gilman, 1959).

Cross glide and dislocation intersections are also ways in which kinks and jogs can be formed. Seitz (1951) points out that kinks and jogs in ionic crystals can sometimes be charged.

Under some circumstances, intersecting dislocations can react to form a new dislocation. An example is the reaction  $\frac{a}{2} [0\bar{1}\bar{1}] + \frac{a}{2} [\bar{1}01] \rightarrow \frac{a}{2} [\bar{1}\bar{1}0]$ . The two dislocations lying on oblique  $\{110\}$  primary glide planes meet along a  $[\bar{1}\bar{1}\bar{1}]$  direction and unite to form a new dislocation with the primary glide

vector, but lying on a  $\{112\}$  plane. This dislocation is relatively immobile (Kear et al., 1959), and is a type of Lomer-Cottrell lock.

In MgO, slip is observed to take place by the development of dislocation bands which are usually nucleated at surface defects and widen by a dislocation multiplication mechanism. When two orthogonal dislocation bands intersect, one band produces a kinking in the other at the intersection and a crack may develop (Argon and Orowan, 1964). However, if all slip bands are parallel, or if a large number of slip bands are present, cracks become stabilized and a high ductility occurs.

#### b. Yield Stress

It was shown by Johnston and Gilman (1959, 1960) that if fresh dislocations are introduced at the surface of NaCl-type ionic crystals, the macroscopic yield stresses are determined by the stresses required to move these dislocations in the crystals. The yield stresses are not determined by (1) the stress to pull dislocations away from impurity atmospheres, (2) the stress to push dislocations through a forest of other dislocations, or (3) the stress to operate Frank-Read sources. Rather they are determined by the frictional resistance of the crystal to dislocation movement (Gilman, 1961a).

Yield stresses in ionic crystals are quite sensitive to temperature because of the sensitivity of dislocation motions to changes in temperature. This is shown in Figure 1 for LiF single crystals (Gilman, 1961a). However, it may be noted that only part of the yield stress is temperature dependent, as indicated by the fact that the curves for different LiF crystals lie paral-



rel to each other as their hardnesses vary with temperature. The hardness difference is caused by different impurity contents of the crystals.

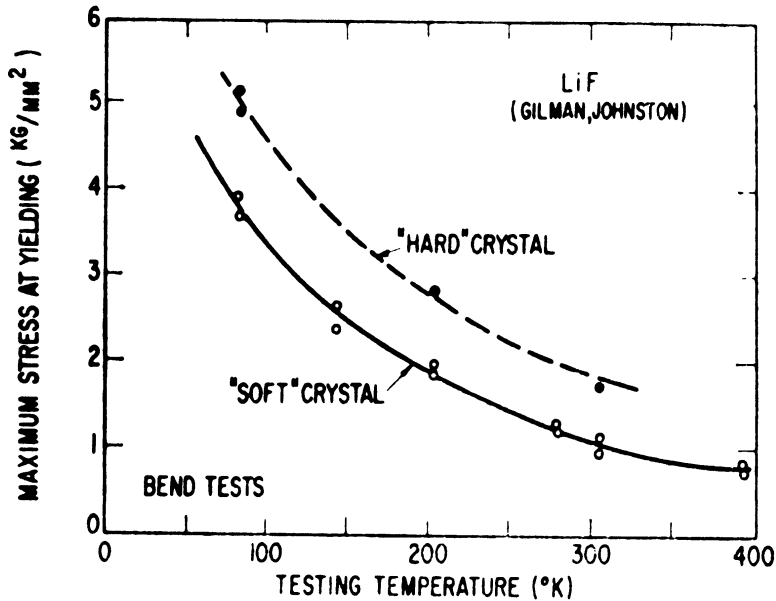


Figure 1. Variation of yield stress with temperature for ionic crystals (Gilman, 1961a).

Chao et al. (1964b) have shown that the hot hardness of pure MnS and MnS containing one percent Ca impurity in solution gives a similar behavior.

### c. Yielding Versus Slip System

An intrinsic effect of the crystal structure is the variation in yield stress with glide plane. Stepanov and Bobrikov (1957) measured this effect in NaCl single crystals between room temperature and 500°C, and found that the required stress for slip on {111} and {001} planes is higher than for {110} glide in the same  $\langle 1\bar{1}0 \rangle$  direction. Gilman (1959a) observed the same behavior in LiF crystals and concluded that, since the Burger's vectors for all these slips were  $\langle 1\bar{1}0 \rangle$  and the elastic strain energies were essentially the same, only the difference in the core structure of dislocations can explain the large dislocation mobility differences.

#### d. Plasticity and Strain Hardening

Because the number of dislocation sources in the surface controls the glide, it also controls the rate of strain hardening. As the number of interfering glide bands increases, the rate of strain hardening increases, as was demonstrated by Stokes (1962). Barriers such as impurities, boundaries, and Lomer-Cottrell locks can obstruct dislocation motion. Dislocation pile-up at a barrier can cause a "back-stress" which would oppose the applied stress. Thus the stress acting on the source and causing the generation of dislocations would tend to become neutralized (Parker, E. R., 1958). The rate of cross slip and therefore of both multiplication and debris formation increases with the stress applied to the crystal.

#### e. Plasticity Versus Surface

Surface conditions appear to have an appreciable effect on the plasticity of ionic crystals because "brittle" materials may fracture due to surface flaws before they have a chance to deform plastically. Also surface conditions can determine the distribution of slip and consequently, control the ductility in this way.

Coblentz (1903) reported that NaCl crystals can be plastically deformed after they have been wetted. This is the well-known Joffé (1924) effect which may be largely due to the removal of gross surface defects such as microcracks and products of chemical reactions rather than due to a characteristic of ionic crystals (Gorum et al., 1958; Class et al., 1959).

Milch (1909) reported that sticks of rock salt could be bent very readily after heating.

Schmid and Boas (1936) and more recently Vaughn and Davisson (1959) have found that surface conditions, per se, do not have a strong influence on the fundamental event in plasticity--the mobilities of dislocations.

f. Yielding and Impurities

Eshelby et al. (1958) found that the addition of divalent impurities to NaCl would cause maxima and minima in the yield strength versus temperature plot. Differences in ion size cause difficulties in dislocation movement. Different valences of impurities cause both charge and size effects which lock dislocations. Results show that divalent impurities in a monovalent structure are about two orders of magnitude more effective than monovalent impurities in raising the yield stress of NaCl-type crystals (Gilman, 1961a).

g. Plasticity Versus State of Stress

The ability of ionics to deform plastically is dependent on the stress state. Bridgman (1952) has shown that the introduction of large hydrostatic pressures markedly increases the ductility of metals. He (1947) has also shown that the strength and ductility of NaCl and  $Al_2O_3$  are increased by the application of hydrostatic pressure.

#### 4. FRACTURE

For a perfect crystal, the theoretical stress required for fracture along a cleavage plane is about  $E/\pi$  where  $E$  = elastic modulus normal to the cleavage plane (Gilman, 1963). Usually the stress is far smaller, as small as  $E/10^5$ . Low fracture stresses are caused by surface defects in the crystals or by plas-

tic flow which precedes fracture and which creates very high stresses in localized regions. When both plastic flow and surface defects are eliminated, ionic crystals require very high stresses to make them fracture (Stokes, 1962; Johnston, 1963).

The fracture process is considered to occur in two parts: (a) nucleation of cracks and (b) growth or propagation of cracks. Both of these will be considered separately.

#### a. Nucleation

The most important source of cracks or flaws in crystalline ceramics is the external surface. Surface deposits or reaction products can provide interfaces at which cracks may form. Stokes et al. (1960) have demonstrated that surface precipitates formed on improperly dried NaCl crystals lead to premature failure.

Evidence now seems conclusive that cracks form as a result of plastic flow in regions where the motion of dislocations is impeded by some sort of barrier (Parker, 1963). This barrier may be the intersection of glide bands or the intersection of a glide band with a boundary. In each case, a stress concentration is provided by the nonhomogeneous nature of the slip process, wherein a region of localized plastic shear is constrained within an elastically strained matrix (Johnston and Parker, 1963; Low, 1963).

Stokes (1958) and Washburn et al. (1959) concluded that cracks often form at the intersection of two slip bands in MgO crystals. Stokes (1958) attributed the crack formation to a Stroh (1954) mechanism whereby dislocations which piled-up at a kink band coalesced to nucleate a crack. Washburn et al.

(1959) associated the crack formation with a Cottrell (1953, 1958) mechanism where dislocation pile-up on two intersecting  $\{110\}$  slip bands leads to crack nucleation along a  $\{100\}$  plane. Keh et al. (1959) suggested that the mechanism for  $\{110\}$  cracks might be that dislocations on two intersecting  $\{110\}$  planes pile-up against the resultant immobile dislocation on the  $(112)$  plane with a  $[\bar{1}10]$  vector and initiate a crack in a third  $\{110\}$  plane.

Stokes et al. (1961) and Johnston (1963) showed that MgO crystals are brittle or ductile depending on the slip distribution. If, for example, deformation in MgO proceeds by nucleation and growth of a single glide band which spreads along the gauge length, the crystal may exhibit 7 percent or more plastic strain before fracture. However, if just two glide bands intersect at the onset of yielding, complete fracture can occur with very small macroscopic strain.

Work on MgO bicrystals misoriented from each other by varying amounts showed that cracks may form at a grain boundary due to a stress concentration resulting from the inability of a glide band to penetrate a neighboring grain (Johnston et al., 1962) or from the interaction of two slip bands (one from each grain) which intersected the boundary a few microns apart (Westwood, 1961).

#### b. Growth

When Griffith's (1921) theory of crack growth by the release of elastic energy is applied to NaCl-type ionic crystals, it is found that the calculated critical crack length for propagation is much larger than anything one might

expect to remain undetected in the crystal (Stokes and Li, 1963; Miles, 1964). Yet fracture still occurs. It has now been shown, however, that plastic flow is itself nucleated by the microcracks and enables them to grow (Stokes and Li, 1963; Miles, 1964).

Screw dislocations also have a large effect on crack propagation. A crack running perpendicular to a screw dislocation can split into two cracks (cleavage step) when it strikes the dislocation line (Gilman, 1961a).

The principal energy absorbing mechanisms appear to be (1) the creation of cleavage steps as the crack advances and (2) localized plastic deformation by dislocation nucleation and movement (Gilman, 1957; Amelinckx, 1958) at the tip of the crack. In single crystals, the controlling factor in the growth of cracks is the resistance to plastic deformation at the crack tip which, in turn, is influenced by temperature, composition, and microstructure (Low, 1963). The process of blunting the crack tip and replacing the concentration of elastic stress by a more diffuse distribution of stress associated with dislocations depends upon dislocation mobility. At lower velocities, the propagation of a crack is unstable (Gilman and Stauff, 1958). Appreciable amounts of plastic flow may take place if sufficient time is available after dislocations have been nucleated by a moving crack.

In the absence of cleavage step formation, dislocation nucleation, etc., a crack moves through a crystal by causing successive breakage of atomic bonds across the plane of the crack. The energy required to do this is related to the cohesive energy and is sometimes defined as the true surface energy of the crystal (Gilman, 1961a).

Cracks which form in MgO at the intersection of two orthogonal  $\{110\}$  slip bands and propagate over a  $\{110\}$  plane are often blocked by neighboring glide bands (Stokes et al., 1959). The ability of a glide band to arrest a crack was first observed in NaCl by Melankolin and Regal (1956) and stems from the fact that the crack has to cut through the screw components of a very large number of dislocations making up the band. The consequence of this crack stabilization is that the total deformation preceding fracture depends critically on the distribution of slip at the onset of yielding.

Temperature strongly influences the ease of crack propagation in ionic crystals. Raising the temperature increases the ductility of a crystal by increasing the mobilities of dislocations. Even when the dislocation mobility is essentially zero, however, as in silica or alumina at room temperature, cracks too small to propagate can grow progressively at a constant stress through the action of an active environment such as water vapor (Johnston, 1963).

#### B. Hardness and Hardness Testing

The indentation hardness test is probably the simplest method of measuring strength of materials but it is also the least understood in terms of stress and strain distribution (Keh, 1960). Indentation hardness tests have been used extensively to characterize polycrystalline materials and a large amount of literature has resulted which has been summarized in several books (Lysaght, 1949; Tabor, 1951; Mott, 1956). Some progress has been made in analyzing the stress and strain distribution of several types of indenters, but the results

cannot be applied directly to single crystals having well defined slip systems (Hill, 1950) because even the most symmetric crystals show marked anisotropy with respect to hardness and plastic flow around the indenter.

Since Vickers and Knoop hardnesses were used exclusively in this study, the review will be confined to these two tests.

## 1. VICKERS HARDNESS

The Vickers hardness test utilizes a square base diamond pyramid as the indenter. The included angle between opposite faces of the pyramid is  $136^\circ$  degrees. The diamond pyramid hardness number (DPH) or Vickers hardness number (VPH) is defined as the load divided by the surface area of the indentation, calculated from microscopic measurements of the impression diagonals, and is expressed in  $\text{kg}/\text{mm}^2$ . The versatility of the test is due to the fact that it provides a continuous hardness scale, for a given load, from very soft to very hard materials (Dieter, 1961). Theoretically, the DPH should be independent of applied load, but in reality it decreases with increasing loads up to about 1 kg (Bückle, 1959). Care should thus be taken to specify loads when reporting microhardness readings (i.e., results for loads less than 1 kg).

Of the many factors which affect the quality of microhardness readings, the most important are: (1) preparation of the specimen (polishing is necessary), (2) vibration, (3) measurement of the impression, (4) load and loading rate, (5) shape of the indenter, and (6) sensitivity of equipment (Bückle, 1959).

Hardness can become a measure of the yield stress or the ease with which dislocations can move through a crystal. Westbrook (1958a) found that the



yield stress of NaCl was related to its Vickers hardness as:  $Y.S. = H_V/35$ , where Y.S. is the yield stress in  $\text{kg}/\text{mm}^2$  and  $H_V$  is the Vickers hardness in the same units. A linear relation between hardness and elastic modulus for other NaCl-type crystals has been shown by Gilman (1961a). Empirical correlations have also been obtained between hardness and (1) melting point (Westbrook, 1958b; Wolff, 1958), (2) surface energy of the indented material (Kuznetsov, 1957; Kolsky, 1957), and (3) the energy needed to create new surfaces at fractures (Roesler, 1956).

Marsh (1963) has tried to draw a consistent picture between the DPH and the general mechanical behavior of glasses and other highly elastic isotropic materials. Tolansky and Nickols (1949, 1952) and Bückle (1954, 1959) found that Vickers indentations gave distorted impressions on single crystals of tin and aluminum and that material pile-up around the indentations is crystallographically directional and independent of the indenter orientation.

Warrick (1963) studied the change in hardness of NaCl with temperature from room temperature to  $1075^\circ\text{F}$ . The hardness of MnS, as well as of certain types of iron and steel, has been determined between  $20^\circ$  and  $1000^\circ\text{C}$  by Chao et al. (1964b).

Keh (1960) innovated the use of etch pit techniques to study the deformation patterns around Vickers indentations in MgO at various temperatures. Chao et al. (1964a) studied dislocation rosettes and slip in MnS single crystals by this technique.

## 2. KNOOP HARDNESS

The Knoop indenter is a diamond pyramid in which the included conical

angles subtended by the longer and shorter edges, respectively, are  $172^{\circ}30'$  and  $130^{\circ}$ . In the plane of the specimen, the indentation has the shape of a parallelogram in which the longer diagonal is about seven times the shorter diagonal (Tabor, 1951). The construction is such that very little elastic recovery takes place in the direction of the long diagonal. The long diagonal becomes the basis of the hardness measurement which is defined as:  $H_K = W/A$ , where  $H_K$  = Knoop hardness number,  $W$  = dead weight load applied and  $A$  = unrecovered projected area of the impression.

Because of the shape of the Knoop indenter, the hardness numbers are influenced by the orientation of the indenter on single crystal specimens. This hardness anisotropy of single crystals has been investigated by numerous authors on materials such as Al (Petty, 1963; Garfinkle and Garlick, 1967), Ti (Feng and Elbaum, 1958; Partridge and Roberts, 1964), Mg (Schwartz et al., 1961; Partridge and Roberts, 1964), Zn (Daniels and Dunn, 1949; Partridge and Roberts, 1964), Fe (Daniels and Dunn, 1949), Cd (Partridge and Roberts, 1964), Co (ibid.), Be (ibid.), Os (ibid.), W (Garfinkle and Garlick, 1967), and Nb (ibid.). In addition, Chao et al. (1964b) and Moore (1965) have measured the orientation dependence of Knoop hardness on the (001), (011), and (111) surfaces of MnS and MnO respectively. Because of the complex nature of this deformation problem, none of the authors has stated a successful quantitative theory to explain their results.

Daniels and Dunn (1949), who investigated the hardness anisotropy on single crystals of silicon ferrite and zinc, are the only persons who have attempted to formulate a theory to explain this behavior. Their analysis is based on

calculating a resolved shear stress on slip planes and in slip directions assuming that four tensile forces act in directions parallel to the steepest slope of each facet of the indenter and cause material to move to the surface. This assumption has been the subject of some criticism (Mebs, 1949).

### C. Pertinent Information on MnO, MnS, MnSe, and MnTe

#### 1. STRUCTURE AND PHASE RELATIONS

The MnS and MnSe utilized in this investigation have the face-centered cubic NaCl-type structure. Both show two other unstable allotropic modifications (Baroni, 1938; Taylor and Kagle, 1963): a cubic zincblende (sphalerite) structure and a hexagonal wurtzite form. Manganese oxide also has the NaCl structure. Manganese telluride at room temperature has a hexagonal NiAs structure depicted in plan view in Figure 2, with a  $c/a$  ratio of 1.621. The difference between the NaCl and NiAs structure is merely one of stacking anion and cation layers. For the NaCl structure the sequence is AcBaCbAcB etc... along  $\langle 111 \rangle$  while for the NiAs structure it is AcBcAcBc etc... along  $\langle 0001 \rangle$ . The capital letters represent anion layers and the lower case letters, layers of the smaller cations. The exact crystal structure of MnTe may not be of the simple NiAs variety, however, because of the possible "super-lattice" often associated with NiAs-type materials as outlined by Wyckoff (1965). In addition, the problem is further complicated by a slight amount of nonstoichiometry in MnTe as reported by Johansen (1958). He found that the compound was a tel-

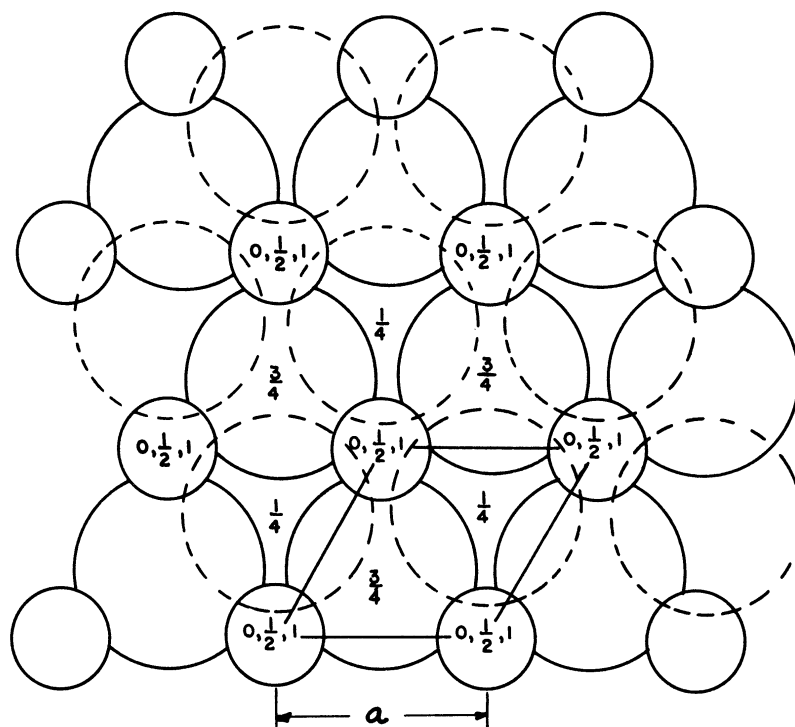


Figure 2. Diagram of the hexagonal NiAs-type structure of manganese telluride looking down the c-axis. The smaller circles represent manganese atoms and the larger, tellurium. The numbers at the centers of the circles designate fractional distances above base level along the c-axis.

lurium excess material with a composition range  $\text{MnTe}_{1.002}$  to  $\text{MnTe}_{1.013}$ . To a very good approximation, however, the structure may be assumed to be the simple NiAs-type. MnTe transforms to the NaCl structure above  $1040^\circ\text{C}$  (Johnston and Sestrich, 1961).

The systems Mn-S, Mn-Se, and Mn-Te all show two compounds—MnS and  $\text{MnS}_2$ , MnSe and  $\text{MnSe}_2$ , and MnTe and  $\text{MnTe}_2$  (Furberg, 1953; Hansen, 1958), respectively, all of which appear to be very nearly of stoichiometric composition. Blitz et al. (1933) state that the  $\text{Mn}^{+2}$  ion is very stable and it is therefore to be expected that MnTe and  $\text{MnTe}_2$ , in contrast to analogous compounds of related metals, have a very small homogeneity range. Kelly (1939) and Kiessling (1966, 1967) report that both MnS and MnSe are stoichiometric.

The system MnO-MnS was studied by Chao et al. (1963) and their results are presented in Figure 3. Mehta et al. (1967) studied the MnS-MnSe system and found a continuous series of solid solutions as shown in Figure 4. Tien et al. (1967) investigated the system MnTe-MnS and found the results shown in Figure 5. Panson and Johnston (1964) and Makovetski and Sirota (1964) studied the system MnTe-MnSe, although the latter authors determined solid solubility limits at a temperature of 800°C only. The diagram of Panson and Johnston (1964) is shown in Figure 6 where it is seen that there is extensive solid solubility above 550°C and that above 1040°C a single phase solid solution of the NaCl-type structure exists for all compositions. Kiessling et al. (1966, 1967) have investigated the solid solubility limits at 1150°C for systems of the type (Mn, Me)S and (Mn, Me)(S,Se) where Me represents the metal Ti, V, Cr, Fe, Co, or Ni. This limit was found to vary continuously with a maximum for Cr and Fe substituted in the MnS, MnSe, and  $\text{MnS}_{0.5}\text{Se}_{0.5}$  lattices.

## 2. OTHER PROPERTIES

The compounds of manganese with Group VI elements are all antiferromagnetic with Néel temperatures as shown in the following table (Squire, 1939; Kittel, 1957):

Compound	Néel Temp. (°K)
MnO	122
MnS	145-154
MnSe	150-165
MnTe	307

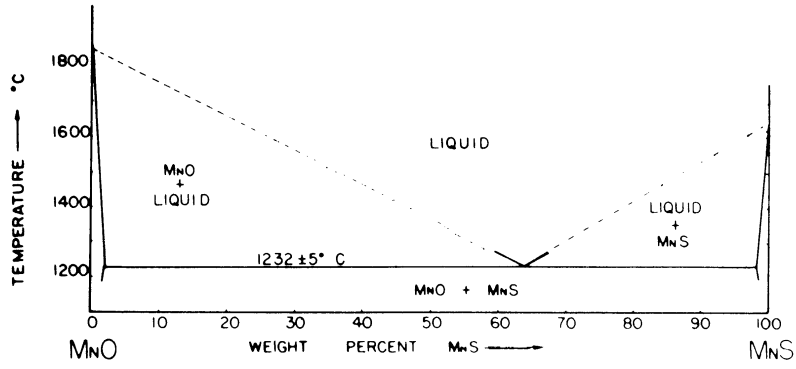


Figure 3. The system MnO-MnS.  
(Chao et al., 1963).

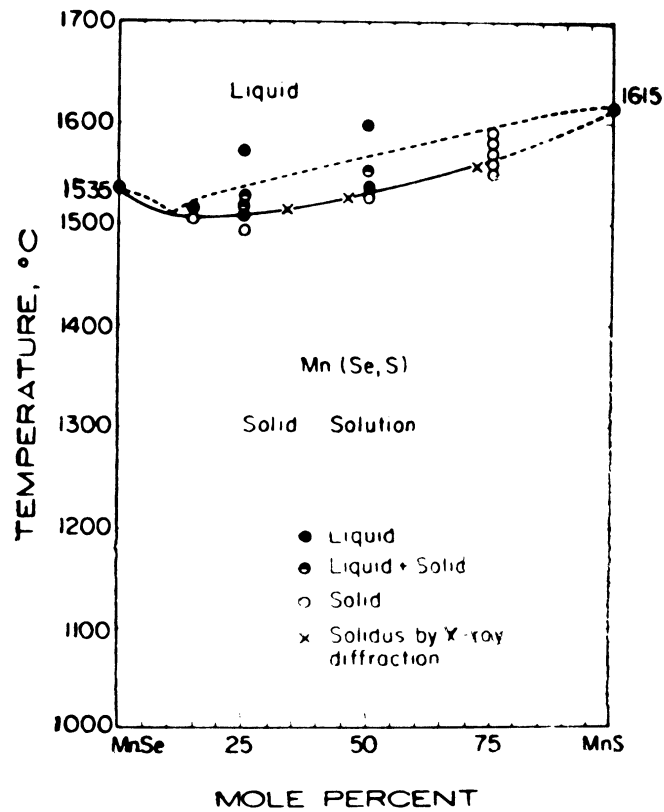


Figure 4. The system MnSe-MnS  
(Mehta et al., 1967).

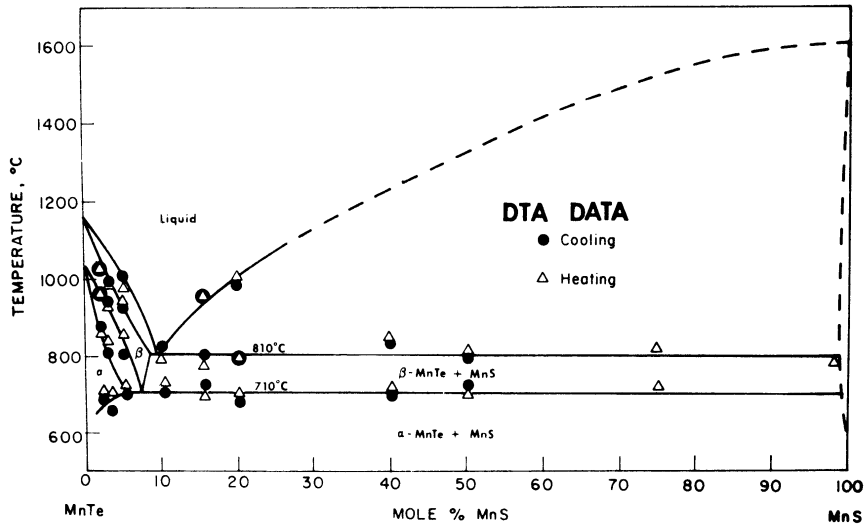


Figure 5. The system MnTe-MnS (Tien *et al.*, 1967).

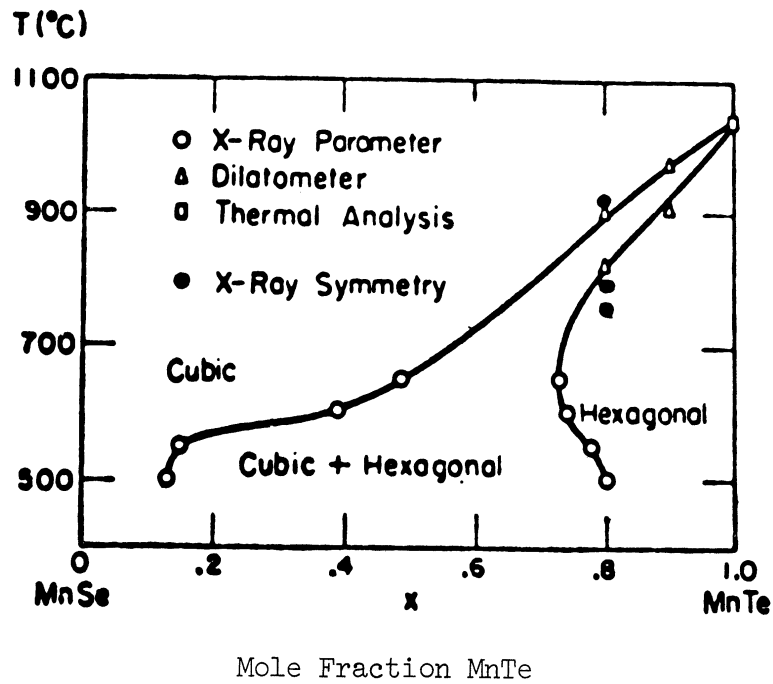


Figure 6. The system MnSe-MnTe (Panson and Johnston, 1964).

Above the Néel temperature, the magnetic moments of the  $\text{Mn}^{+2}$  ions are randomly oriented and the material appears paramagnetic. For  $\text{MnO}$ ,  $\text{MnS}$ , and  $\text{MnSe}$  below their Néel temperatures, the magnetic moments of the  $\text{Mn}^{+2}$  line up anti-parallel along the  $\langle 100 \rangle$  directions giving a magnetic unit cell with twice the dimensions of the chemical unit cell as shown in Figure 7.

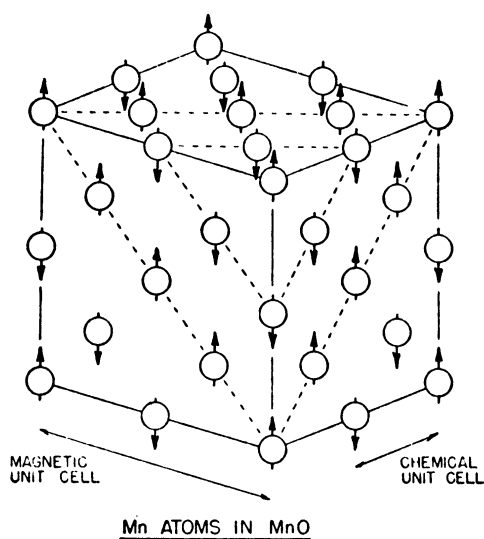


Figure 7. Antiferromagnetic structure of  $\text{MnO}$  below its Néel temperature. Only Mn ions are shown (Shull et al., 1951).

The antiferromagnetism may also result in a slight distortion of the unit cell from cubic symmetry. Changes from FCC symmetry to (1) a slightly distorted FCC (i.e., rhombohedral) cell have been observed for  $\text{MnO}$  (Tombs and Rooksby, 1950; Shull et al., 1951),  $\text{MnS}$  (Tombs and Rooksby, 1951),  $\text{NiO}$  (Tombs and Rooksby, 1951; Slack, 1960), and  $\text{FeO}$  (Tombs and Rooksby, 1950) and to (2) a tetragonal structure in the case of  $\text{CoO}$  (Tombs and Rooksby, 1950; Greenwald, 1953).

Greenwald (1953) and Grazhdankina and Gurfel (1958) have investigated the thermal expansion of  $\text{MnTe}$  by X-ray lattice parameter measurements and both found a sharp contraction in the c-axis at around  $310^\circ\text{K}$  on cooling. The a-axis con-



tinued to change linearly with temperature. This is due to the antiferromagnetic transformation at this temperature and suggests that the magnetic moments of the  $\text{Mn}^{+2}$  ions are parallel to the c-axis but anti-parallel to each other on successive (0001) planes.

Also investigated have been the magnetic susceptibilities of  $\text{MnO}$  (Bizette et al., 1938; Banewicz et al., 1961),  $\text{MnS}$  (Squire, 1939; Banewicz and Lindsay, 1956),  $\text{MnSe}$  (Squire, 1939; Lindsay, 1951; Banewicz et al., 1961), and  $\text{MnTe}$  (Squire, 1939; Banewicz et al., 1961). Of particular interest are the susceptibility results of Lindsay (1951) and the thermal expansion results of Makovetski and Sirota (1963) for  $\text{MnSe}$ . Lindsay's magnetic susceptibility measurements show a large thermal hysteresis in the range  $-196^{\circ}\text{C}$  to  $25^{\circ}\text{C}$  and a dependence of susceptibility on field strength—phenomena which are not observed in  $\text{MnS}$  (Banewicz and Lindsay, 1956). He proposes a theory to explain this in terms of three phases which hypothetically exist in the experimental temperature range and which possess different susceptibilities. He does not explain the nature of these phases.

Makovetski and Sirota (1963) noted anomalous behavior in the thermal expansion coefficient at low temperatures and attributed it to a polymorphic change in addition to the known antiferromagnetic transformation. X-ray diffraction patterns were taken at room temperature and at  $197^{\circ}\text{K}$  after quenching in liquid nitrogen. At  $197^{\circ}\text{K}$  several additional peaks appear but the authors do not speculate on the nature of this "second phase."

Kelly (1939) also observed anomalies in the specific heat-temperature curve for  $\text{MnSe}$ . The temperatures specified by Lindsay (1951), Makovetski and

Sirota (1963), and Kelly (1939) for the anomalous behavior differ significantly in each case. More recently, however, Makovetski and Sirota (1966) have reported that MnSe transforms to the sphalerite (cubic ZnS) modification at low temperatures.

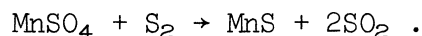
Thermal expansion coefficients have been measured for MnO (Moore, 1965), MnS (Moore, 1965), MnSe (Makovetski and Sirota, 1963), and MnTe (Greenwald, 1953; Grazhdankina and Gurfel, 1958).

## CHAPTER I

### EXPERIMENTAL PROCEDURE

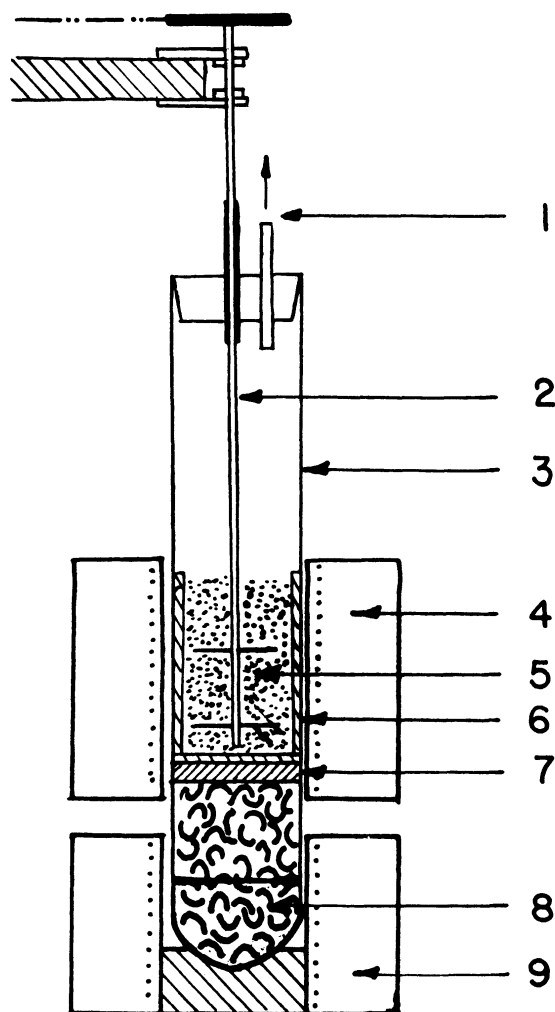
#### A. Raw Materials

Manganous sulfide (MnS) was prepared by the sulfur deoxidation of reagent grade manganous sulfate ( $\text{MnSO}_4 \cdot \text{H}_2\text{O}$ ) of 99.6% purity in an apparatus shown schematically in Figure 8 (Chao et al., 1964a; Moore, 1965). Sulfur was vaporized at 410-430°C and one atmosphere pressure in a vycor tube and contacted the  $\text{MnSO}_4$  powder at 900°C. The inside of the vycor tube was lined with graphite felt around the  $\text{MnSO}_4$  charge and the charge itself was held on a piece of graphite resting on alumina saddles. The following reaction appears to be appropriate:



Chao's (1964a) analysis of the green NaCl-type MnS prepared in this way showed  $36.8 \pm 0.2\%$  sulfur compared with 36.9% for stoichiometry. To prevent the slow oxidation of the MnS powder to  $\text{MnSO}_4$ , the product was melted and solidified under vacuum into ingots weighing about 60 grams each.

Manganese selenide was prepared in a way similar to that used by Kelly (1939), Panson and Johnston (1964), and Mehta et al. (1967). Manganese metal powder and selenium powder, 100 mesh or more, were mixed in appropriate portions, placed in a vacuum degassed graphite crucible and encapsulated in a pyrex tube under a vacuum of about 10 microns. This was reacted at 600°C for several days.



- |                             |   |
|-----------------------------|---|
| 1. SO <sub>2</sub> exhaust  | 6. Graphite felt liner  |
| 2. Stirrer                  | 7. Perforated graphite disk<br>on support of Al <sub>2</sub> O <sub>3</sub> saddles |
| 3. Vycor reaction tube      | 8. Liquid sulfur  |
| 4. Upper furnace, 900°C     | 9. Lower furnace,<br>410-430°C  |
| 5. MnSO <sub>4</sub> charge |   |

Figure 8. Apparatus used for the preparation of stoichiometric manganese sulfide.

The manganese powder was prepared by triply vacuum distilling 99.9% electrolytic manganese to remove oxides and then crushing under a nitrogen atmosphere.

High purity selenium shot supplied by Canadian Copper Refiners Limited was also crushed under a nitrogen atmosphere. A typical analysis of the selenium was:

Hg	0.5	ppm
Te	1	ppm
Pb	1	ppm
Fe	0.5	ppm
Cu	0.08	ppm

The MnSe prepared in this way was kept in the pyrex tube until ready for use. In general, 0.5 to 1% excess selenium over the stoichiometric amount was used in the initial MnSe reaction. This excess Se could be conveniently removed by placing the MnSe at the far end of a vycor tube attached to a vacuum pump. This end was then heated to 800°C and the excess Se drawn off.

X-ray examination revealed no other phases but microscopic examination revealed minor amounts of MnO in spite of precautions taken during MnSe preparation.

Manganese telluride was prepared in a manner exactly analogous to that used for MnSe. A typical analysis of the high purity tellurium shot, also supplied by the Canadian Copper Refiners Limited, was:

Se	370	ppm
Pb	5	ppm
Cu	0.3	ppm
Al	2	ppm
Mg	1	ppm

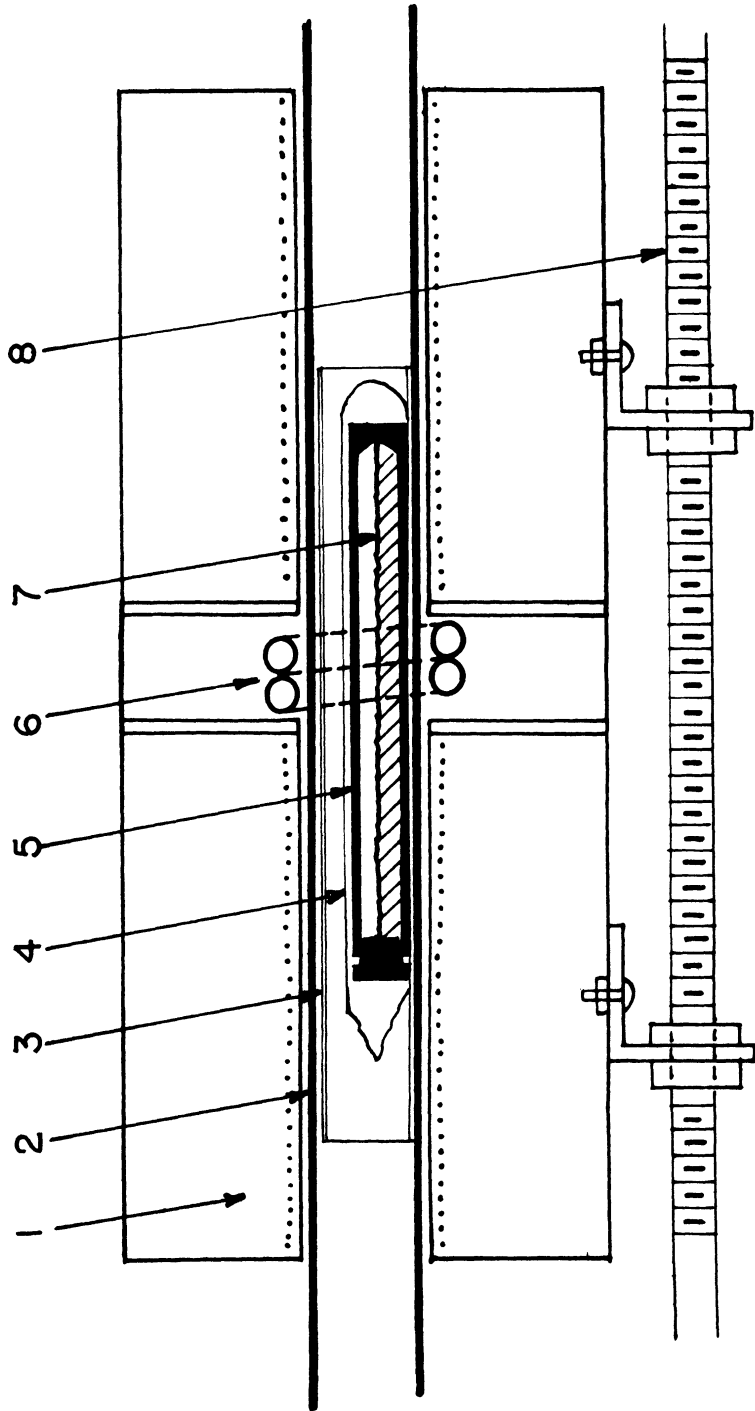
The MnTe also revealed minor amounts of MnO on microscopic examination. The reaction:  $\text{Mn} + \text{Te} \rightarrow \text{MnTe}$  was more exothermic and uncontrollable than that for MnSe but the graphite crucible provided an effective heat sink.

## B. Materials Purification

Manganous sulfide was further purified by a zone refining procedure. About 60 grams of the previously solidified MnS were crushed and remelted under a purified argon atmosphere in a graphite boat within a horizontal moving coil induction furnace. After four or five passes at a speed of 3 in./hr, the MnS developed a coarsely crystalline grain size. Microscopic and X-ray examination revealed no other phases and X-ray data, extrapolated to  $\theta = 90^\circ$  using the Nelson-Riley factor,  $\frac{1}{2} (\cos^2\theta/\sin\theta + \cos^2\theta/\theta)$ , gave a lattice parameter of 5.224Å compared with 5.224Å reported by ASTM (Card 6-018), 5.225Å given by Chao et al. (1964a), and 5.2236Å reported by Wyckoff (1965).

Manganese selenide and manganese telluride were also purified by a zone refining technique using an apparatus like that shown in Figure 9. Both MnSe and MnTe, when melted in graphite under argon at one atmosphere total pressure, slowly decomposed to elemental Se or Te with the formation of manganese carbide. The manganese carbide decomposed upon exposure to air into a complex hydrated manganese oxide.

It was necessary, therefore, to seal the graphite crucible containing the MnSe or MnTe in a fused silica tube under a pressure of about 200 mm of purified nitrogen. With this procedure, a back pressure of Se or Te was built



1. Secondary furnace, 650-700°C.
2. Moving vycor tube.
3. Fused silica protecting tube.
4. Fused silica encapsulating tube.
5. Graphite crucible.
6. Two turn induction coil.
7. Sample to be zone refined.
8. Screw drive mechanism.

Figure 9. Schematic diagram of zone refining apparatus for the purification of manganese selenide and manganese telluride.

up which prevented the reaction of Mn with the crucible. The partial pressure of nitrogen was necessary when zone refining MnSe so that, at the zone refining temperature, a total pressure slightly greater than one atmosphere existed within the fused silica tube. The tube was thus prevented from slowly collapsing around the graphite crucible.

The secondary furnace around the two-turn induction coil was necessary to prevent cracking of the fused silica tube due to phase changes in devitrified material on cooling (General Electric Co., 1964). This furnace was maintained at 650°C for MnTe and 700°C for MnSe.

Eight to ten passes were made at a speed of 3 in./hr for both MnSe and MnTe. In each case the first 60 percent of the resultant ingot was used as the purified raw material.

Microscopic examination revealed no other phases in either MnSe or MnTe except for an occasional inclusion which apparently was MnO. Chao et al. (1963) showed that the maximum solubility of MnO in MnS is only 1.7 weight percent. Therefore, it can reasonably be assumed that, because of the much larger ion size differences involved (ionic radii:  $O^{-2} = 1.32\text{\AA}$ ,  $S^{-2} = 1.74\text{\AA}$ ,  $Se^{-2} = 1.91\text{\AA}$ , and  $Te^{-2} = 2.11\text{\AA}$ ) (Van Vlack, 1964), the oxide solid solubility in MnSe at room temperature is very small and would be smaller yet in MnTe. Furthermore, Chao et al. (1964b) found that the effect of MnO on the hardness of MnS was small from room temperature to 1000°C. On this basis, it is assumed that the very small amounts of MnO encountered have very little effect on the properties studied.



X-ray powder patterns gave a lattice parameter for the NaCl-type MnSe of  $a_0 = 5.463\text{\AA}$  which compares with  $5.462\text{\AA}$  reported by ASTM (Card 11-683) and  $5.45\text{\AA}$  by Taylor and Kagle (1963). Manganese telluride, which has a hexagonal NiAs-type structure gave  $a_0 = 4.138\text{\AA}$  and  $c_0 = 6.706\text{\AA}$ . This compares with average values of  $a_0 = 4.137\text{\AA}$  and  $c_0 = 6.706\text{\AA}$  as reported by ten separate authors.

Chemical analyses were performed on MnSe and MnTe using methods described by Kriege and Theodore (1966) and Vogel (1961). Manganese was determined by an EDTA titration using Eriochrome Black T as indicator and selenium and tellurium were determined gravimetrically by precipitation from  $\text{SO}_2$  saturated solutions. The reader is referred to the original articles for procedural details.

For MnSe, the results gave 40.5 to 41.3% Mn and 59.4 to 60.0% Se by weight. Stoichiometric MnSe is 41.0% Mn and 59.0% Se. Kelly (1939), Kiessling et al. (1967), and Panson and Johnston (1964) report nearly stoichiometric MnSe.

For MnTe the results gave 30.0 to 30.4% Mn and 69.5 to 69.8% Te by weight compared with 30.1% Mn and 69.9% Te theoretically.

### C. Crystal Growth

#### 1. PURE COMPOUNDS

The MnS as zone purified provided grains of sufficient size to be used in the single crystal studies.

With the MnSe or MnTe about 30 grams of the material was placed in a 5 in. long x  $3/8$  in. I.D. vacuum degassed graphite crucible and encapsulated

under a pressure of 200 mm of purified nitrogen in a fused silica tube. This tube was placed in a larger vycor tube and the whole assembly lowered through an induction coil at the rate of about  $3/8$  in./hr. This produced single crystals of sufficient size to be used in this study.

The growth of single crystals of MnTe proved to be difficult because MnTe undergoes an inversion from a NaCl-type structure to a hexagonal NiAs-type on cooling below  $1040^{\circ}\text{C}$  (Johnston and Sestrich, 1961; Tien et al., 1967). In addition, a sharp contraction of the c-axis occurs at  $307-310^{\circ}\text{K}$  due to an antiferromagnetic transformation (Greenwald, 1953; Grazhdankina and Gurfel, 1958). As a result, good quality single crystals were not obtained. Rather, a coarse-grained structure was found in which individual grains tended to be misoriented from each other by, at most, 8 to 10 degrees. For instance, when looking at a (0001) back-reflection Laue photograph, bands of spots were seen rather than rows of single spots, the total band scatter being 8 to 10 degrees at most. This could be described as a coarse mosaic structure. Quite often a "crystal" would show only two or three separate mosaic parts differing by not more than  $\pm 3$  degrees from a mean value. These crystals were used whenever possible.

## 2. BINARY COMPOSITIONS

For single crystals of other than the pure compounds, the individual components were crushed to around 50 mesh, mixed in the desired portions, placed in a graphite crucible, and sealed in fused silica as before. Each of the compositions was chemically analyzed for Se or Te or both Se and Te by the methods

already outlined (Vogel, 1961; Kriege and Theodore, 1966) utilizing at least two samples for each analysis. Compositions in single phase regions of the systems MnS-MnSe and MnSe-MnTe were studied.

#### D. Sample Preparation

##### 1. ORIENTING AND CUTTING

Single crystals were cleaved from the solidified ingots, placed in a graphite crucible, sealed in a vycor tube under a vacuum of 10 microns, and annealed for 12 hours at 1000°C.

Following the annealing treatment the crystals were mounted on a goniometer and oriented to the desired crystal plane by the Laue back-reflection technique. They were then transferred, maintaining orientation, to another holder and slices cut with a 0.010 in. thick rubber bonded alumina wheel on a Dimet cut-off machine.

For the cubic structures (001), (011), and (111) planes were studied and the orientations were accurate to within 2 degrees. Investigated in the hexagonal systems were the (0001), (10 $\bar{1}$ 0), and (11 $\bar{2}$ 0) planes. These orientations were accurate to within about 8 to 10 degrees.

##### 2. MOUNTING AND POLISHING

The samples were mounted in bakelite (or solder for low temperature testing) preparatory to polishing. Samples were polished on 400 and 600 grit silicon carbide paper and then on 8 micron and 1/2 micron diamond wheels. Next they were polished with Linde B alumina powder under alcohol on a Syntron

vibratory polisher and etched with a solution of composition 1% conc.  $H_2SO_4$ , 1% phosphoric acid, and 1% of a solution of saturated oxalic acid. Repolishing with 1/2 micron diamond paste and Linde B on the Syntron followed twice more. Because of the softness of the samples (about that of pure Cu or pure Fe) this procedure proved necessary to obtain good surfaces and to remove residual stresses. Subsequent Laue photographs showed no significant residual stresses in the crystals.

Many electrolyte solutions were tested in an effort to develop an electrolytic polishing technique but none proved satisfactory.

Throughout the polishing procedure the samples were checked for parallelism of opposite faces of the mounting material. This was necessary to insure good hardness measurements.

#### E. Testing and Examination Procedure

##### 1. DEFORMATION

The mounted and polished samples were then indented with either a Vickers or Knoop diamond indenter on a Wilson Tukon Hardness Tester and the hardness measured. For the Vickers test the loads used were 200 or 500 grams while for the Knoop test, 100 or 200 grams. The long axis of the Knoop indenter was made parallel to the several low index crystallographic directions on each of the planes tested.

Upon microscopic examination in obliquely reflected light, slip lines were directly observable around the indentations. By noting the angles which these slip traces made with each other and with known crystallographic direc-

tions, and by plotting these traces for a given plane on a stereographic projection according to the method described in Barrett (1952), one could determine the indices of all planes capable of making such traces. By comparing the results from the different crystallographic surfaces, one could uniquely determine the plane or planes upon which slip occurred.

Slip mechanisms were also studied by dislocation etch pit techniques on the (001) plane of MnSe, MnS, and compositions in the system MnS-MnSe. Chao et al. (1964a) developed an etchant for MnS of composition 1%  $H_3PO_4$ , 1%  $H_2SO_4$ , and 1% of a saturated oxalic acid solution which showed a preference for etching edge dislocations intersecting {100} surfaces. The etchant also appeared to work well on {100} of MnSe, giving etch pits, as in MnS, composed of the four {101} facets which intersect a {100} surface at 45 degrees. The etchant was generally ineffective in showing dislocations on surfaces other than the cube faces. By observing dislocation etch pit rosettes around the indentations, insights into the slip mechanism could be obtained and changes in the slip system followed.

A third method utilized to study slip was that of observing Knoop hardness variations as a function of indenter orientation and sample composition. Knoop hardnesses showed anisotropic effects and were found to change relative to each other as well as in absolute value as primary slip systems changed.

An interferometric technique was also used to study flow and pile-up around Vickers indentations on MnS, MnSe, and MnTe.

## 2. FRACTURE

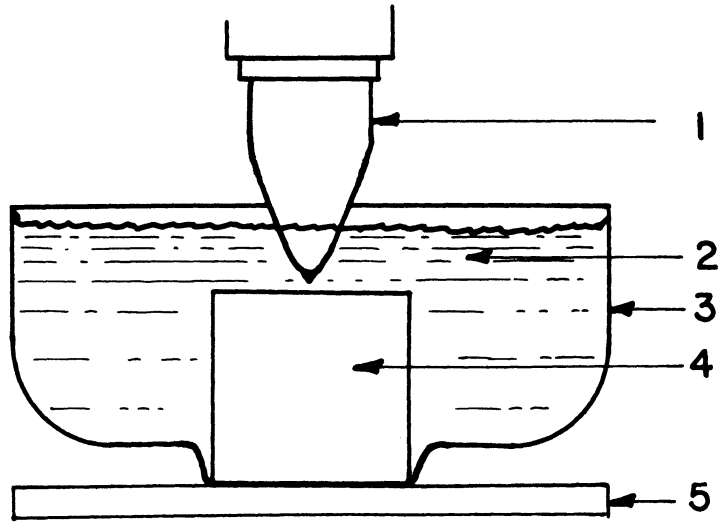
Fracture was studied by attempting to induce cleavage on several of the crystallographic planes of the samples and by noting fracture surfaces on crushed fragments. Also, if fracturing was in evidence around indentations, the type of fracturing was noted and attempts were made to relate this to slip interactions.

## 3. TEMPERATURE EFFECT

In addition to measurements at room temperature, Vickers and Knoop hardness tests were attempted for MnS, MnSe, and MnS-MnSe binary compositions at temperatures of 135°C, -70°C, and -196°C. For these tests, the sample mounts were cemented in a stainless steel cup and the cup filled with a suitable liquid which covered the top of the specimen and at least 1/8 of an inch of the bottom portion of the indenter. A schematic diagram of the apparatus is shown in Figure 10.

In the 135°C tests, a small heating coil was placed around the sample and the sample covered with vacuum pump oil. Hardnesses at room temperature with the specimen immersed in oil did not differ from those obtained in air.

For low temperature tests it was found necessary to mount the samples in solder in order to prevent sample deformation by the squeezing action of the bakelite mold. Bakelite has a thermal expansion coefficient of  $40 \times 10^{-6}/^{\circ}\text{C}$  (Van Vlack, 1964) compared with  $18.5 \times 10^{-6}/^{\circ}\text{C}$  for MnSe (Makovetski and Sirota, 1963), and  $14 \times 10^{-6}/^{\circ}\text{C}$  for MnS (Moore, 1965). This resulted in the sample being exposed to a large compressive stress on cooling, sufficient to cause it



1. Indenter.
2. Oil, alcohol or liquid nitrogen.
3. Insulated stainless steel cup.
4. Sample and mount.
5. Transite board.

Figure 10. Diagram showing technique used for hardness testing at  $-196^{\circ}\text{C}$ ,  $-70^{\circ}\text{C}$ , and  $135^{\circ}\text{C}$ .

to deform in the mold. This does, however, provide an interesting way to study plastic deformation mechanisms in low yield strength materials.

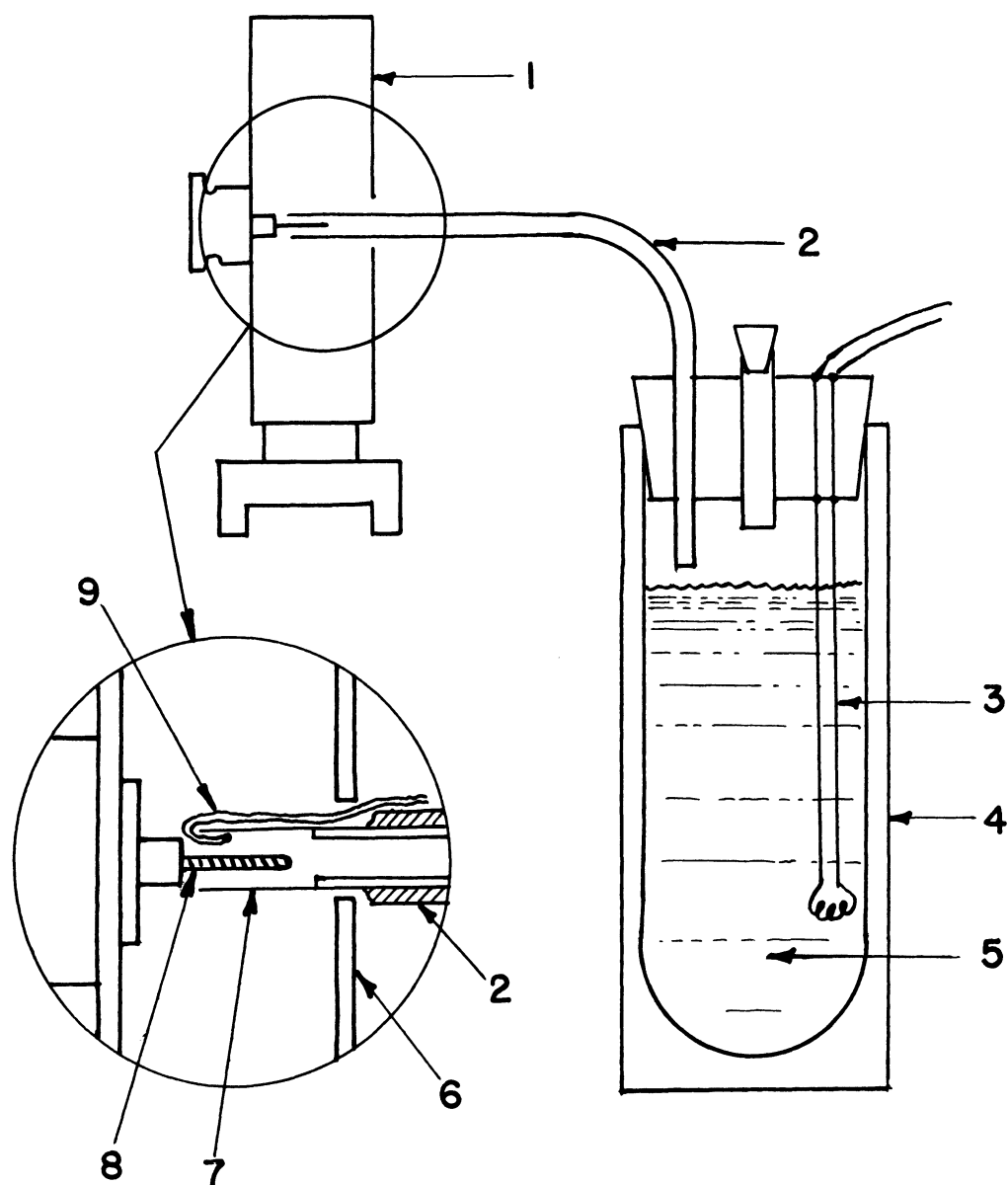
In the  $-70^{\circ}\text{C}$  tests, specimens were immersed under an alcohol-dry ice mixture. Room temperature hardnesses under alcohol agreed with those found in air.

Those tests at  $-196^{\circ}\text{C}$  were made under liquid nitrogen.

#### 4. LOW TEMPERATURE X-RAY STUDY

Finally, low temperature Debye-Scherrer X-ray diffraction patterns at  $-84^{\circ}\text{C}$  and  $-130^{\circ}\text{C}$  were obtained in an attempt to explain anomalous behavior in MnSe at low temperatures as observed in this study and previously by Kelly (1939), Lindsay (1951), and Makovetski and Sirota (1963). An ordinary Debye-Scherrer camera was modified to allow nitrogen vapor to pass over the specimen. The temperature was controlled by adjusting the current input to a small heating coil immersed in a dewer of liquid nitrogen. This in turn controlled the rate of vaporization of nitrogen which would then pass out of the dewer and over the sample. The lowest temperature attainable was  $-135^{\circ}\text{C}$ . This was measured with a chromel-alumel thermocouple placed directly over the specimen in an apparatus shown schematically in Figure 11.





- |                                  |  |
|----------------------------------|--|
| 1. Debye-Scherrer powder camera. | 6. Plastic cover with opaque liner on Debye-Scherrer camera. |
| 2. Insulated copper tubing.      | 7. Cellophane window.  |
| 3. Heating coil.                 | 8. Sample in 0.3 mm capillary tube.                          |
| 4. Dewar.                        | 9. Chromel-alumel thermocouple.                              |
| 5. Liquid nitrogen.              |  |

Figure 11. Schematic diagram of apparatus used to obtain low temperature X-ray powder patterns of manganese selenide.

## CHAPTER IV

### EXPERIMENTAL RESULTS

#### A. Manganous Selenide

##### 1. PLASTIC DEFORMATION

###### a. Mechanism

The observation of slip traces around Vickers indentations on the (001), (011), and (111) planes of MnSe revealed that the primary glide planes are {111}. The slip directions were taken to be the close-packed directions on these planes, giving a Burgers vector  $\frac{a}{2} \langle 110 \rangle$ . The slip mechanism {111}  $\langle \bar{1}10 \rangle$  corresponds to that found in FCC metals and in the NaCl-type compounds uranium carbide (Van Der Walt and Sole, 1967) and titanium carbide (*ibid.*). This is in contrast to the {110}  $\langle \bar{1}10 \rangle$  primary glide mechanism found in MnO (Moore, 1965), MnS (Chao *et al.*, 1964a), and, indeed, in most NaCl-type materials where the chemical bonding is largely ionic. Figures 12, 13, and 14 show the slip lines around Vickers and Knoop indentations on the (001), (011), and (111) planes of MnSe respectively.

On the (001) plane (Figure 12), the slip lines extended in  $\langle 110 \rangle$  directions. This is consistent with the intersections of {111} planes as may be seen from Figure 15, which shows two cubic unit cells together with several low index planes. On the (011) plane, the traces were in  $[0\bar{1}1]$  and  $\langle 112 \rangle$  directions (Figure 13a shows only  $[0\bar{1}1]$  traces) and unequivocally identified

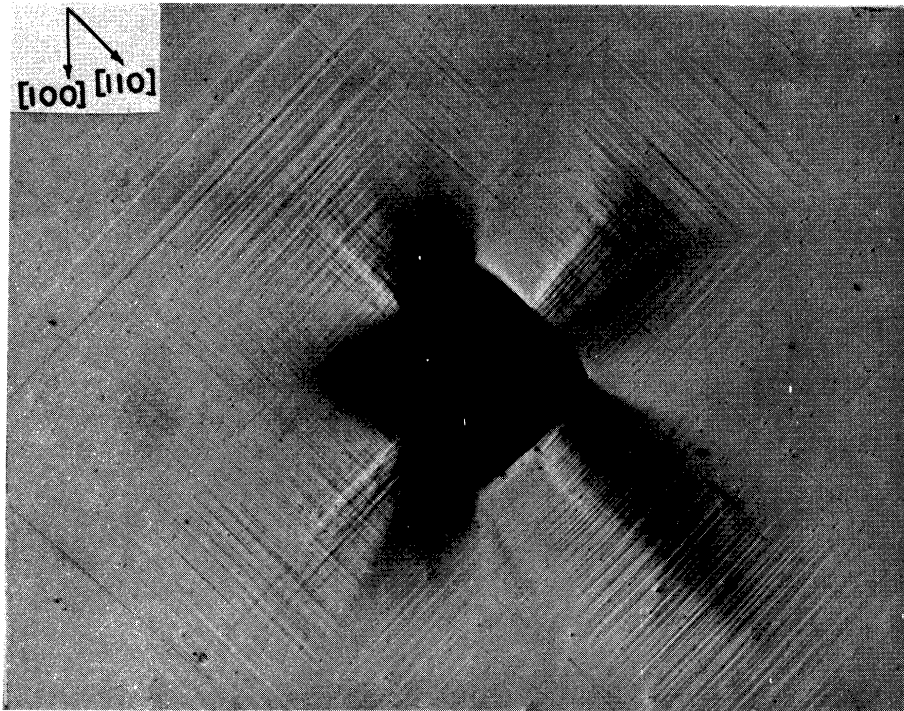
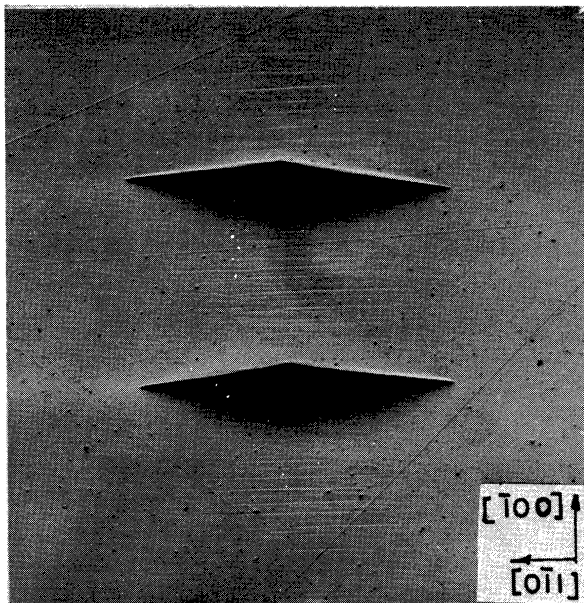
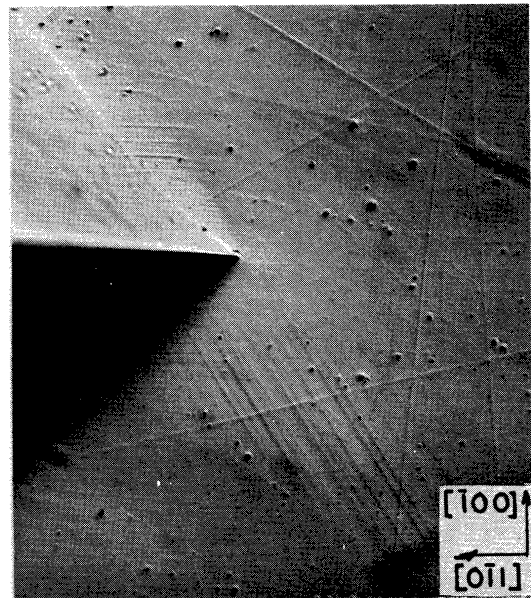


Figure 12. Slip traces around Vickers indentation (500 gm load) on the (001) surface of MnSe single crystal. Oblique lighting. X200.



(a) X250



(b) X500

Figure 13. Slip traces around Knoop and Vickers indentations on the (011) surface of MnSe single crystal. Oblique lighting.

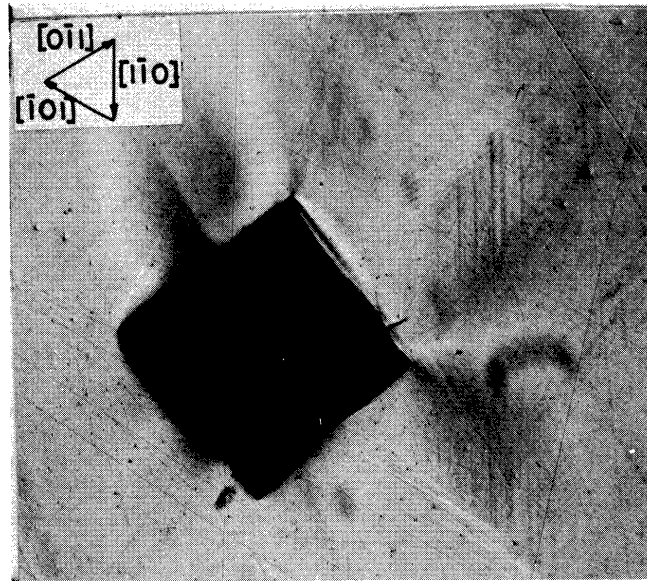


Figure 14. Slip traces around Vickers indentation (500 gm load) on the (111) surface of MnSe single crystal. Oblique lighting. X250.

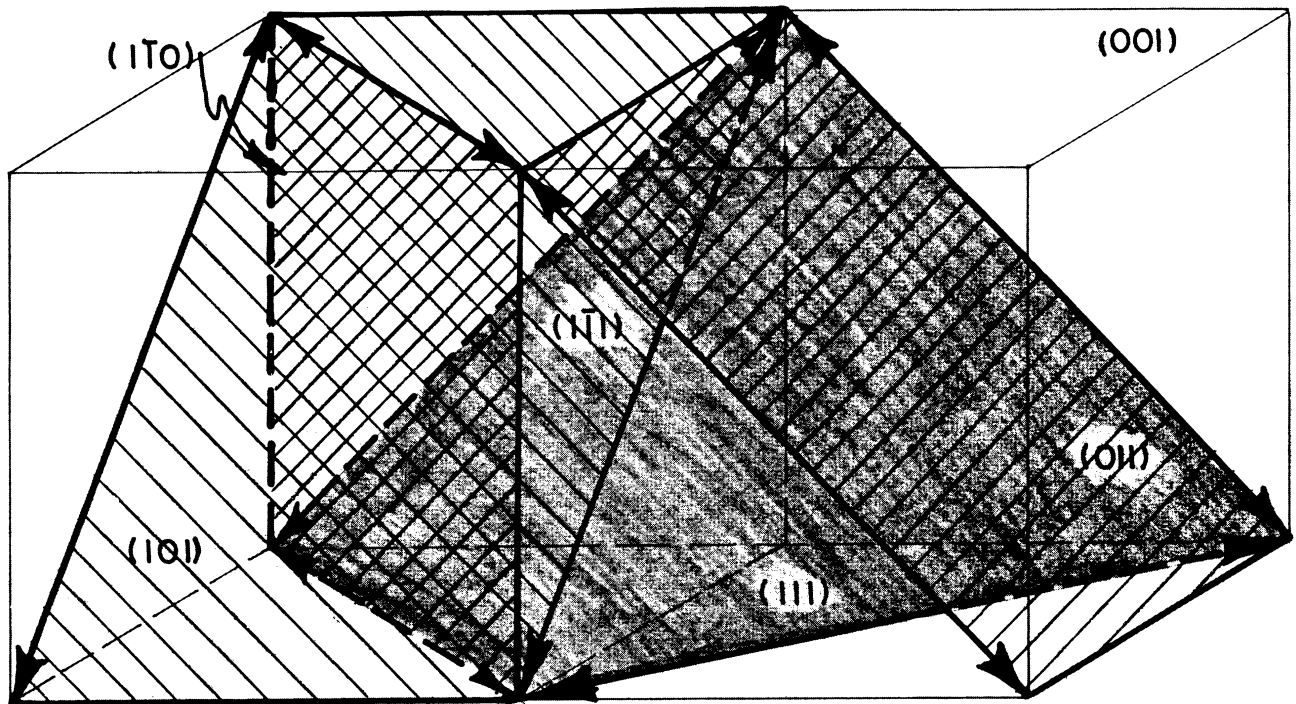


Figure 15. Two cubic unit cells showing several low index planes and their intersections with other planes.

the slip planes as  $\{111\}$ . Slip lines on the  $(111)$  plane were in  $\langle 110 \rangle$  directions, consistent with  $\{111\}$  slip, but they do not provide any additional information since slip on either  $\{100\}$  or  $\{110\}$  planes would also show the same traces.

Chao et al. (1964a) found that the primary slip mechanism in MnS was  $\{110\} \langle 1\bar{1}0 \rangle$  with a secondary mechanism  $\{111\} \langle 1\bar{1}0 \rangle$ . With MnSe,  $\{110\} \langle 1\bar{1}0 \rangle$  slip was observable as a secondary mechanism as seen in Figure 16. The lines in  $\langle 110 \rangle$  directions are attributable to  $\{111\}$  slip while the traces in  $\langle 100 \rangle$  directions connecting the  $\langle 110 \rangle$  lines reveal where cross slip on  $\{110\}$  planes has occurred. The specimen shown in Figure 16 was mounted in bakelite and quenched to  $-70^\circ\text{C}$  in an alcohol-dry ice solution. The differential thermal contraction between the bakelite ( $\alpha = 40 \times 10^{-6}/^\circ\text{C}$  (Van Vlack, 1964)) and MnSe ( $\alpha = 18.5 \times 10^{-6}/^\circ\text{C}$  (Makovetski and Sirota, 1963)) was sufficient to create a compressive stress in the MnSe great enough to cause deformation in certain regions.

#### b. Pile-up and Sinking-in Around the Indenter

For certain orientations of the Vickers diamond pyramid relative to the surface of indentation, impressions of unusual shape were observed. Two examples are shown in Figures 17a and 17b for indentations on the  $(001)$  and  $(011)$  planes respectively. Bückle (1954, 1959) observed the same shaped impression as shown in Figure 17a on the cube face of an aluminum single crystal when the indenter was oriented with its diagonals in  $\langle 110 \rangle$  directions relative to the surface. Using an interferometric technique to observe surface contours, he concluded that the star-shape was not due to extensive elastic recovery, but

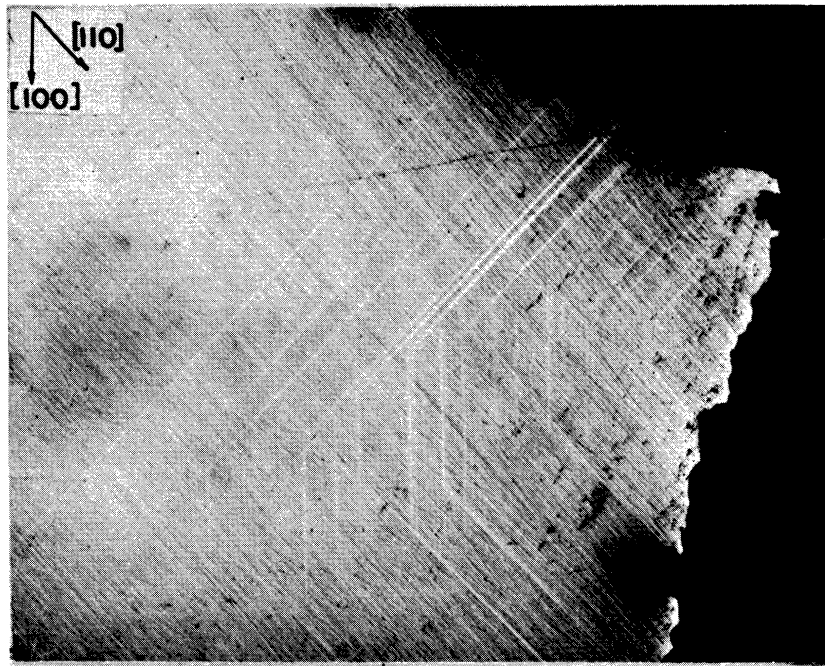


Figure 16. The (001) surface of MnSe single crystal mounted in bakelite and quenched to  $-70^{\circ}\text{C}$ . Slip traces due to  $\{111\}$  glide and  $\{110\}$  cross slip are evident. X250.

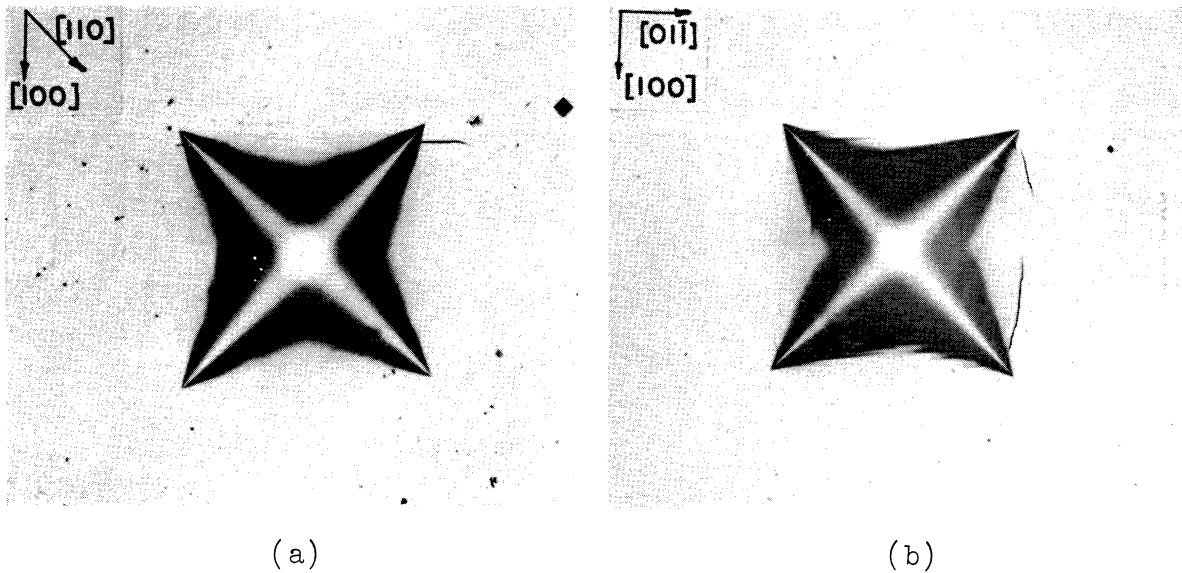


Figure 17. Examples of Vickers impressions of unusual shape on (a) the (001) and (b) the (011) surfaces of MnSe single crystals for certain orientations of the indenter. X500.

rather, was caused by a directional piling-up and sinking-in of material displaced by the indenter.

Interference photomicrographs of Vickers impressions on the (001) surface of MnSe also revealed extensive piling-up and sinking-in of material around the indentations. Figures 18a and 18b show these elevation contours for impressions in which the indenter diagonals were in  $\langle 100 \rangle$  and  $\langle 110 \rangle$  directions respectively. Figure 18a is the same indentation as that shown in Figure 12. These figures indicate four hills or piled-up regions out  $\langle 110 \rangle$  directions on the (001) surface and regions where a sinking-in occurred in  $\langle 100 \rangle$  directions. That the areas in  $\langle 110 \rangle$  directions were actually at a higher elevation was confirmed by microscopic focusing measurements performed at high magnification. The behavior is independent of indenter orientation and is thus a crystallographic phenomenon. The apparent abnormal pile-up in the lower right of both pictures is due to a slight "out-of-levelness" possessed by the specimen during the indentation process but is not indicative of any intrinsic effect associated with the hardness test itself.

Thus, the indenter penetrating the surface causes crystallographic plastic flow leading to a piling-up and sinking-in, the form of which depends upon the symmetry of the slip systems of the crystal. The manner in which the indenter cuts these regions determines the shape of the impression.

A consequence of this preferential pile-up is that, on the (001) surface, for instance, most of the slip traces were seen where the most extensive pile-up occurred and significantly fewer were visible elsewhere.

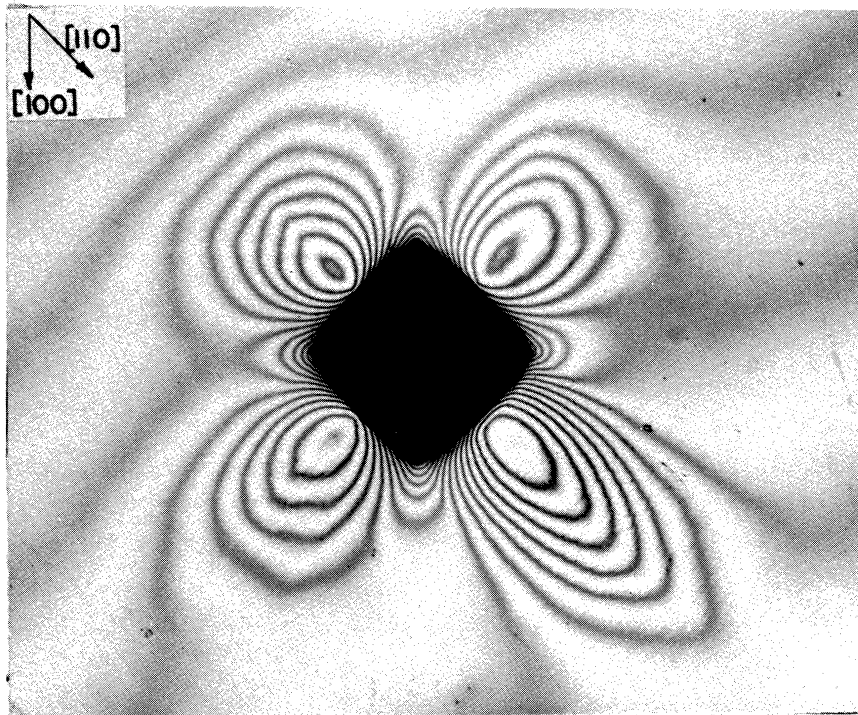
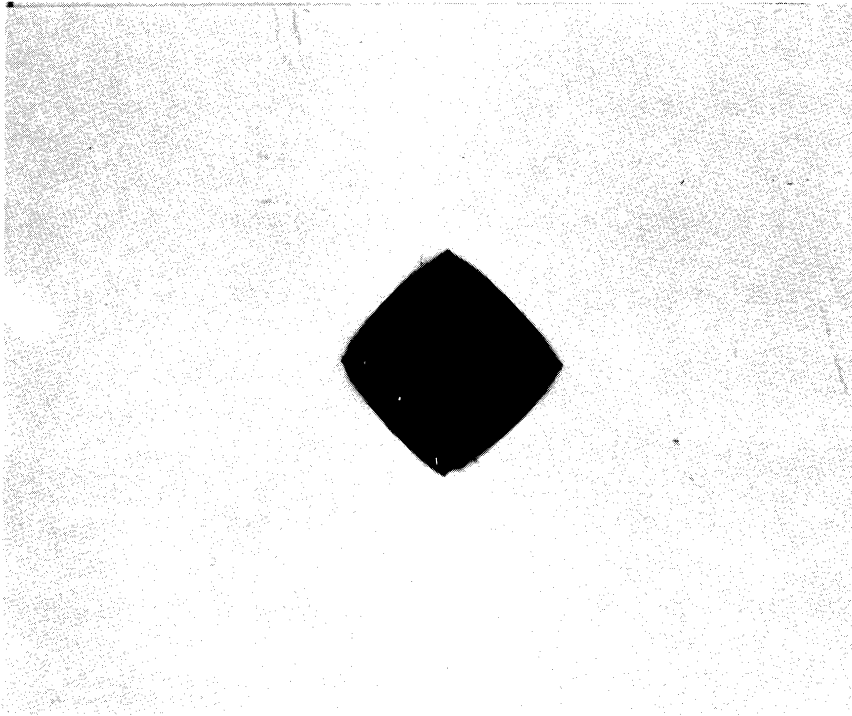


Figure 18(a). Interference micrograph around Vickers indentation (500 gm load) on the (001) surface of MnSe. Indenter diagonals are in  $\langle 100 \rangle$  directions. The top photograph shows more clearly the shape of the impression. X200.



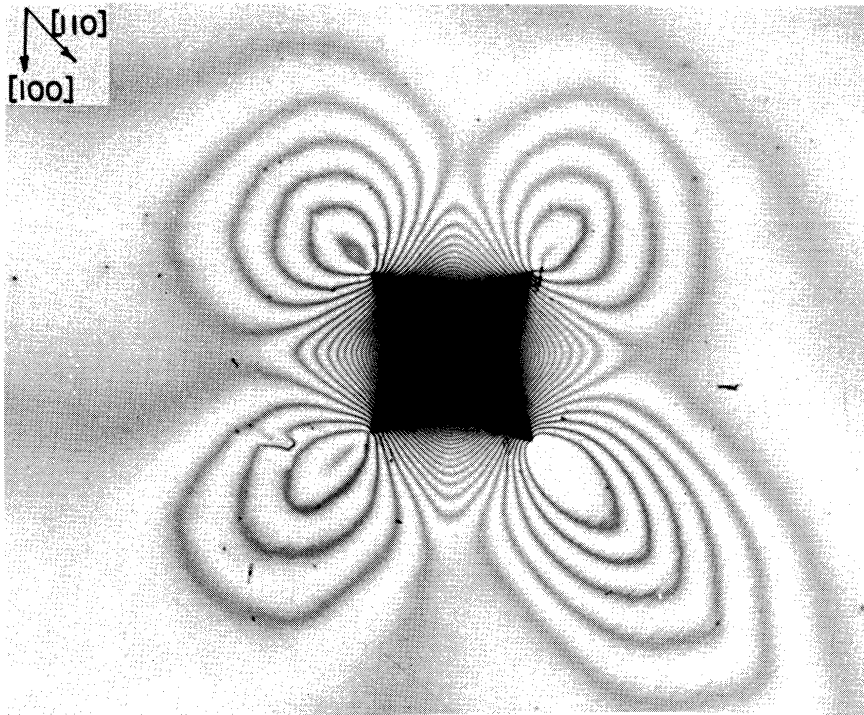
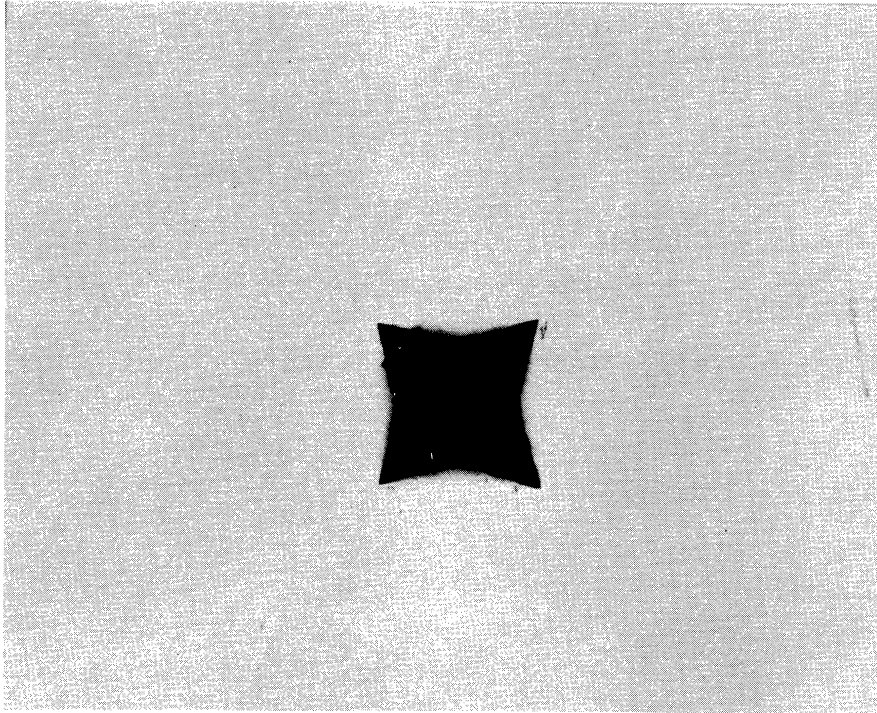


Figure 18(b). Interference micrograph around Vickers indentation (500 gm load) on the (001) surface of MnSe. Indenter diagonals are in  $\langle 110 \rangle$  directions. The top photograph shows more clearly the shape of the impression. X200.

The concentration of slip lines in certain regions is not unique to MnSe however. It was observed by Keh (1960) in MgO at high temperatures and in MnS utilized in this study, both of which have  $\{110\}\langle\bar{1}\bar{1}0\rangle$  as the primary glide mechanism. For example, a Vickers indentation on (001) of MnS is shown in Figure 19. Keh (1960) also observed by interferometry four hills of material in  $\langle 110 \rangle$  directions around indentations on (001) of MgO. This was also detected on MnS as shown in Figures 20a and 20b where the indenter diagonals were in the  $\langle 100 \rangle$  and  $\langle 110 \rangle$  directions respectively. In Figure 20a, the pile-up concentrated at the center of the sides of the indentation with no detectable sinking-in in the  $\langle 100 \rangle$  directions. When the indenter was rotated 45 degrees (Figure 20b), material was found to be piled-up all around the indentation, but again the most extensive pile-up occurred out  $\langle 110 \rangle$ .

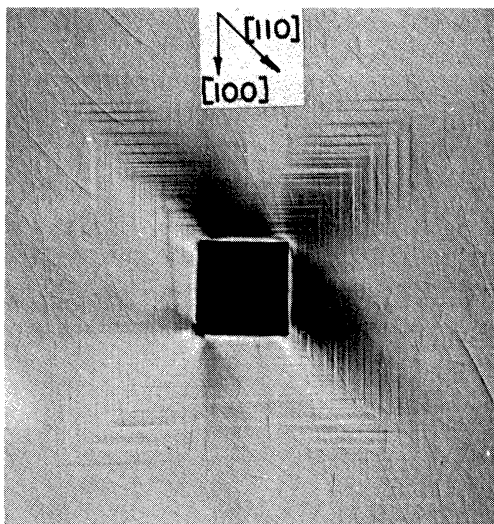


Figure 19. Concentration of slip lines around Vickers indentation (1000 gm load) on the (001) surface of MnS single crystal. Oblique lighting. X150.

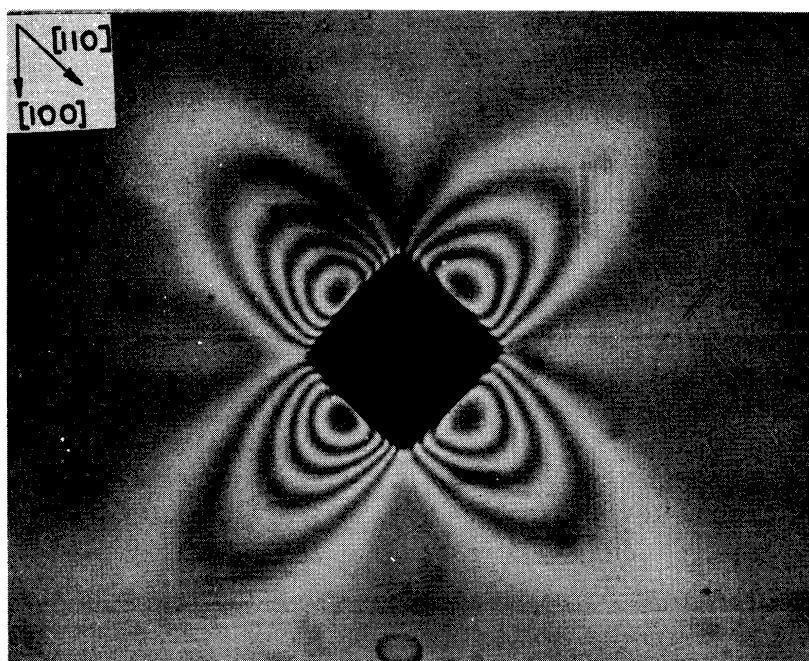
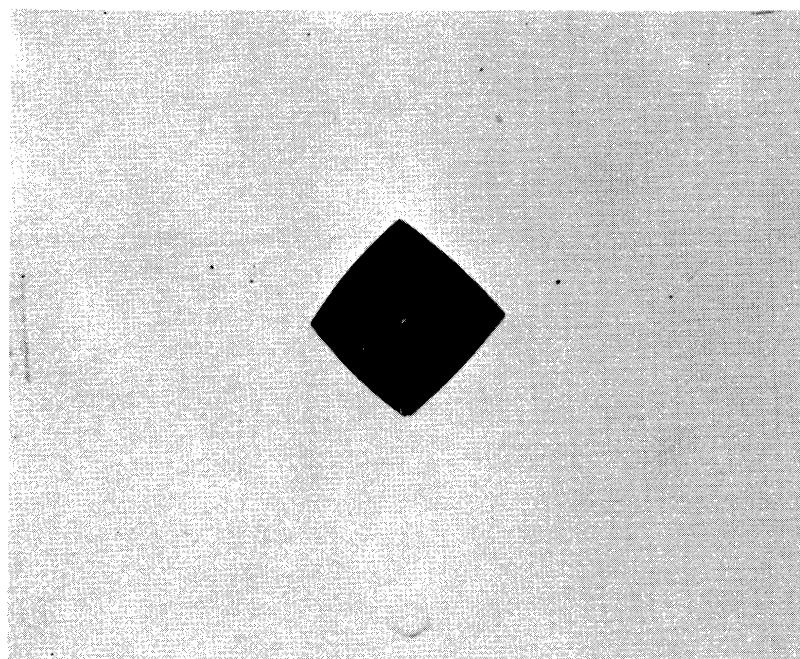


Figure 20(a). Interference micrograph around Vickers indentation (1000 gm load) on the (001) surface of MnS. Indenter diagonals are in  $\langle 100 \rangle$  directions. The top photograph shows more clearly the shape of the indentation. X250.

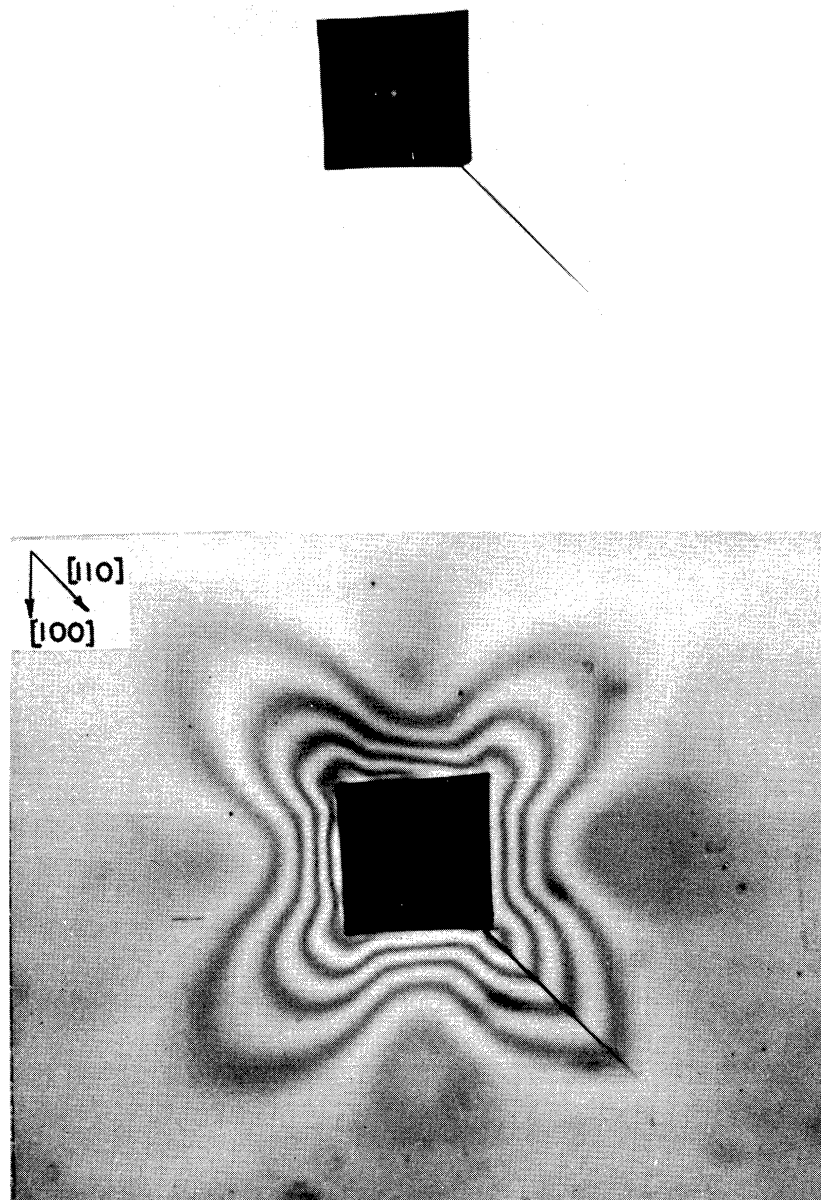


Figure 20(b). Interference micrograph around Vickers indentation (1000 gm load) on the (001) surface of MnS. Indenter diagonals are in  $\langle 110 \rangle$  directions. The top photograph shows more clearly the shape of the indentation. X250.

## 2. FRACTURE

Manganous selenide shows fracture primarily as {100} cleavage in crushed fragments with some secondary {110} cleavage also evident. Chao et al. (1964a) found these same results for MnS and indeed, these observations are directly relatable to the behavior of other materials with the NaCl-type structure (Gilman, 1961a).

Surface indentation tended to produce primarily {100} fracture as may be seen in Figure 21. It should be noted that the cracks are not concentrated at the center of the indentation edges where the greatest sinking-in occurred and consequently where one might expect the greatest "parting" tendency to be, but rather, they are concentrated near the corners of the impression in regions where perpendicular intersecting slip traces are also concentrated. These areas are the ones into which most of the displaced material has been moved and the ones where more complicated problems involving the flow of material arise. Consequently, it is likely that the {100} cracking is the result of a slip or dislocation interaction mechanism rather than simply a {100} tension cleavage crack. This will be considered in more detail in the Discussion section.

In addition to the {100} fracture, minor amounts of {110}<sub>90°</sub> (i.e., a {110} plane at 90 degrees to the plane of indentation) fracture were also observed.

An interesting observation was made on a sample etched with an aqueous solution of composition 1% conc. H<sub>2</sub>SO<sub>4</sub>, 1% H<sub>3</sub>PO<sub>4</sub>, and 1% of a solution saturated with oxalic acid used to reveal dislocation etch pits. Lines of dislocations were seen emanating from the tip of a {100} cleavage crack (Figure 22). The

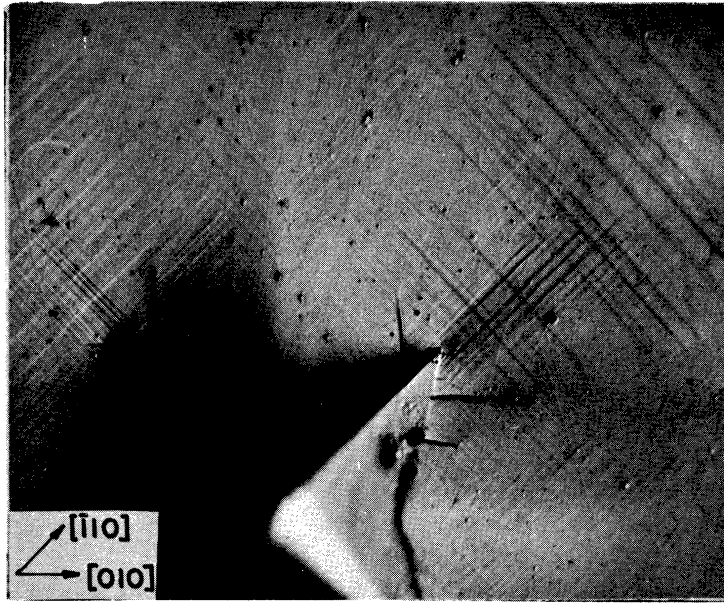


Figure 21.  $\{100\}$  fracture around Vickers indentation on the  $(001)$  surface of MnSe single crystal. Oblique lighting. X450.



Figure 22. Dislocation etch pits in  $(001)$  surface reflecting dislocations nucleated at the tip of a  $\{100\}$  cleavage crack in MnSe. X250.

dislocations apparently were nucleated at the tip of the crack in an effort to replace the concentration of elastic stress by a more diffuse distribution of stress associated with dislocations (Low, 1963).

## B. The System MnSe-MnS

### 1. PLASTIC DEFORMATION

#### a. Slip Traces

Manganous selenide and manganous sulfide were found to form a continuous series of single phase solid solutions (Mehta et al., 1967). The lattice parameter varied linearly with composition. Since each possesses a different primary glide mechanism,  $\{111\}\langle\bar{1}\bar{1}0\rangle$  for MnSe and  $\{110\}\langle\bar{1}\bar{1}0\rangle$  for MnS, it becomes possible to investigate the change in mechanism with composition.

While  $\{110\}\langle\bar{1}\bar{1}0\rangle$  slip was observed as a secondary mechanism in MnSe, it was not detected as slip traces around Vickers indentations. With as little as 10 a/o (atomic percent) substitution of sulfide in selenide, however, traces due to  $\{110\}\langle\bar{1}\bar{1}0\rangle$  slip were detected. As the sulfide content increased, the amount of  $\{110\}$  slip became more pronounced. Figure 23 shows slip traces on the  $\{001\}$  surface of a sample of composition 75 a/o MnSe-25 a/o MnS. Those traces in  $\langle 100 \rangle$  directions forming a square pattern are due to  $\{110\}$  slip while those in  $\langle 110 \rangle$  are the result of  $\{111\}$  slip. Figures 24 and 25 show impressions on the cube face of samples of composition 50 a/o MnSe-50 a/o MnS. Again traces due to both types of slip are visible but the amount of  $\{110\}$  glide has increased. The apparent variability in the density of the slip



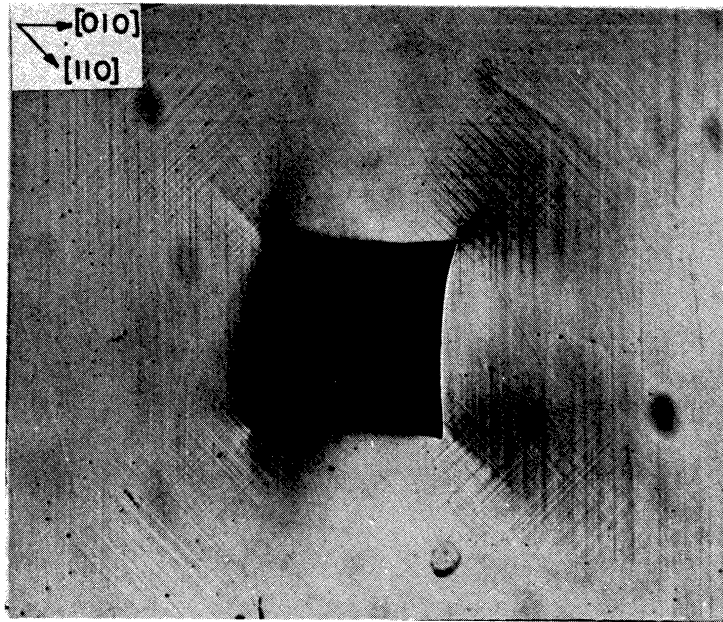


Figure 23.  $\{111\}$  and  $\{110\}$  slip traces around Vickers indentation (1000 gm load) on the (001) surface of 75 MnSe—25 MnS single crystal. Oblique lighting. X250.

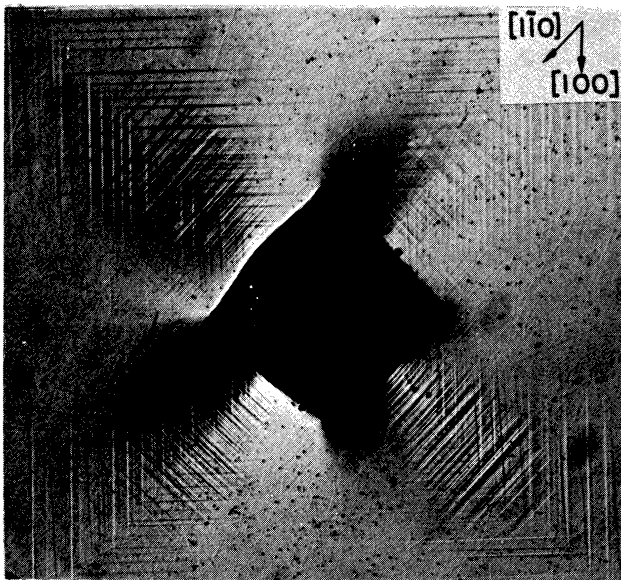


Figure 24.  $\{111\}$  and  $\{110\}$  slip traces around Vickers indentation (500 gm load) on the (001) surface of 50 MnSe—50 MnS single crystal. Oblique lighting. X250.

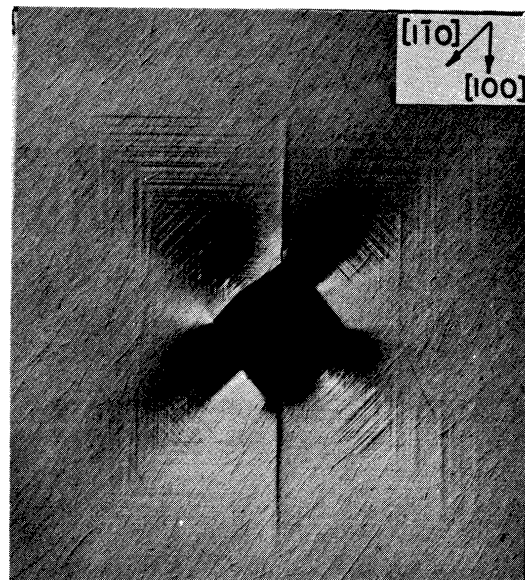


Figure 25. Similar to Figure 24 but showing a  $\{100\}$  crack. X150.



lines on different sides of the indenter is due to the oblique lighting technique used to illuminate the specimen. Figures 26 and 27 display the (001) and (011) surfaces of a sample of composition 25 a/o MnSe-75 a/o MnS while Figures 28 and 29 reveal the (001) and (011) surfaces of pure MnS, which show no evidence of {111} slip. Thus the primary slip mechanisms were found to change gradually with composition, both mechanisms being operative for all intermediate values studied.

#### b. Dislocation Etch Pit Rosette Patterns

It was also possible to follow the change of glide mechanism by the observation of dislocation etch pit rosette patterns around the Vickers indentations. This technique has been used successfully by Keh (1960) on MgO single crystals and by Chao et al. (1964a) on MnS. Figure 30 shows this dislocation etch pit rosette pattern on the cube face of MnS as taken from Chao et al. (1964a) and may be interpreted as follows.

The indenter displaces MnS along the {110} planes in  $\langle 110 \rangle$  directions, and, in effect, provides a dislocation "loop" which swings under the indentation emerging on the other side. Both edge and screw dislocations are identified, the edge dislocations emerging perpendicular to the {001} surface and extending out  $\langle 110 \rangle$  directions on that surface and the screw dislocations emerging at 45 degrees to {001} and extending in  $\langle 100 \rangle$  directions. For MnS, the edge dislocations are more readily etched than the screw dislocations and are revealed acceptably only on the cube plane. This apparently is a consequence of the stability of the surface to the etchant which was an aqueous solution of composition 1% conc.  $\text{H}_2\text{SO}_4$ , 1%  $\text{H}_3\text{PO}_4$ , and 1% of a saturated solution of oxalic acid.

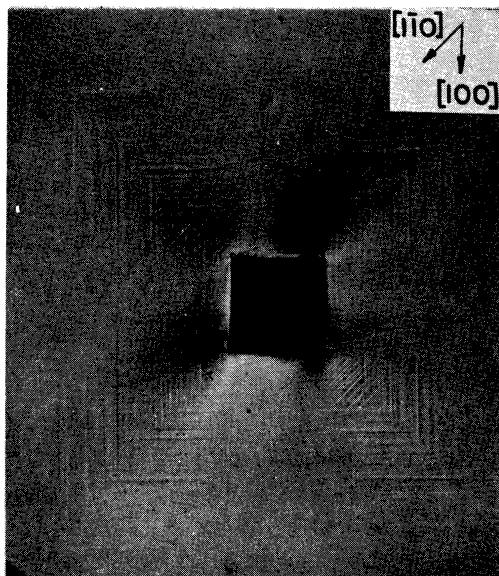


Figure 26

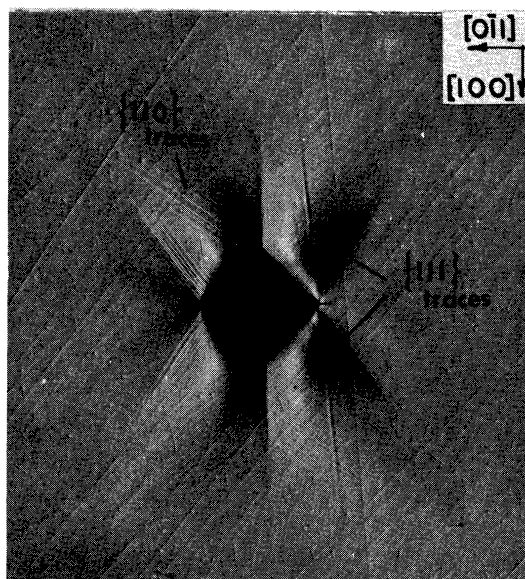


Figure 27

Figures 26 and 27.  $\{111\}$  and  $\{110\}$  slip traces around Vickers indentations (1000 gm load) on the (001) and (011) planes, respectively, of 25 MnSe—75 MnS single crystals. Oblique lighting. X150.

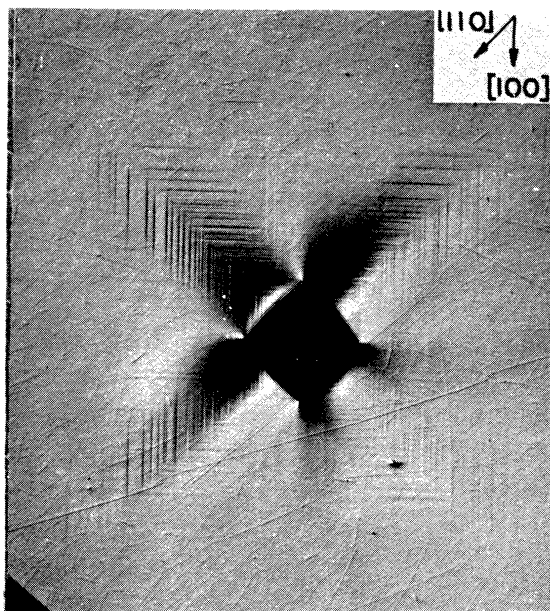


Figure 28

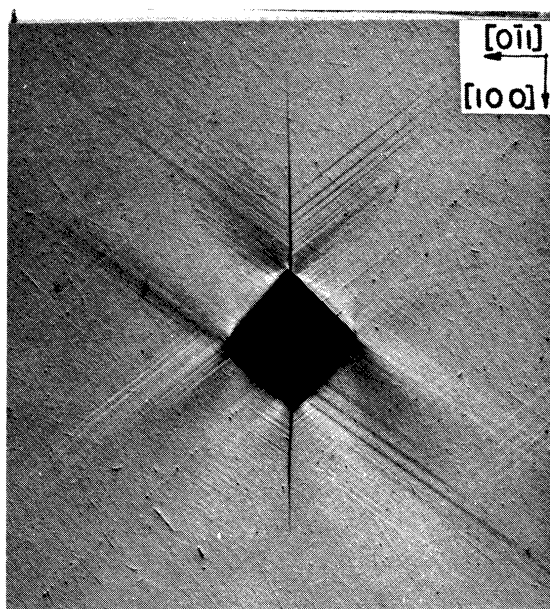


Figure 29

Figures 28 and 29.  $\{110\}$  slip traces around Vickers indentations (1000 gm load) on the (001) and (011) planes, respectively, of MnS single crystals. Oblique lighting. X150.

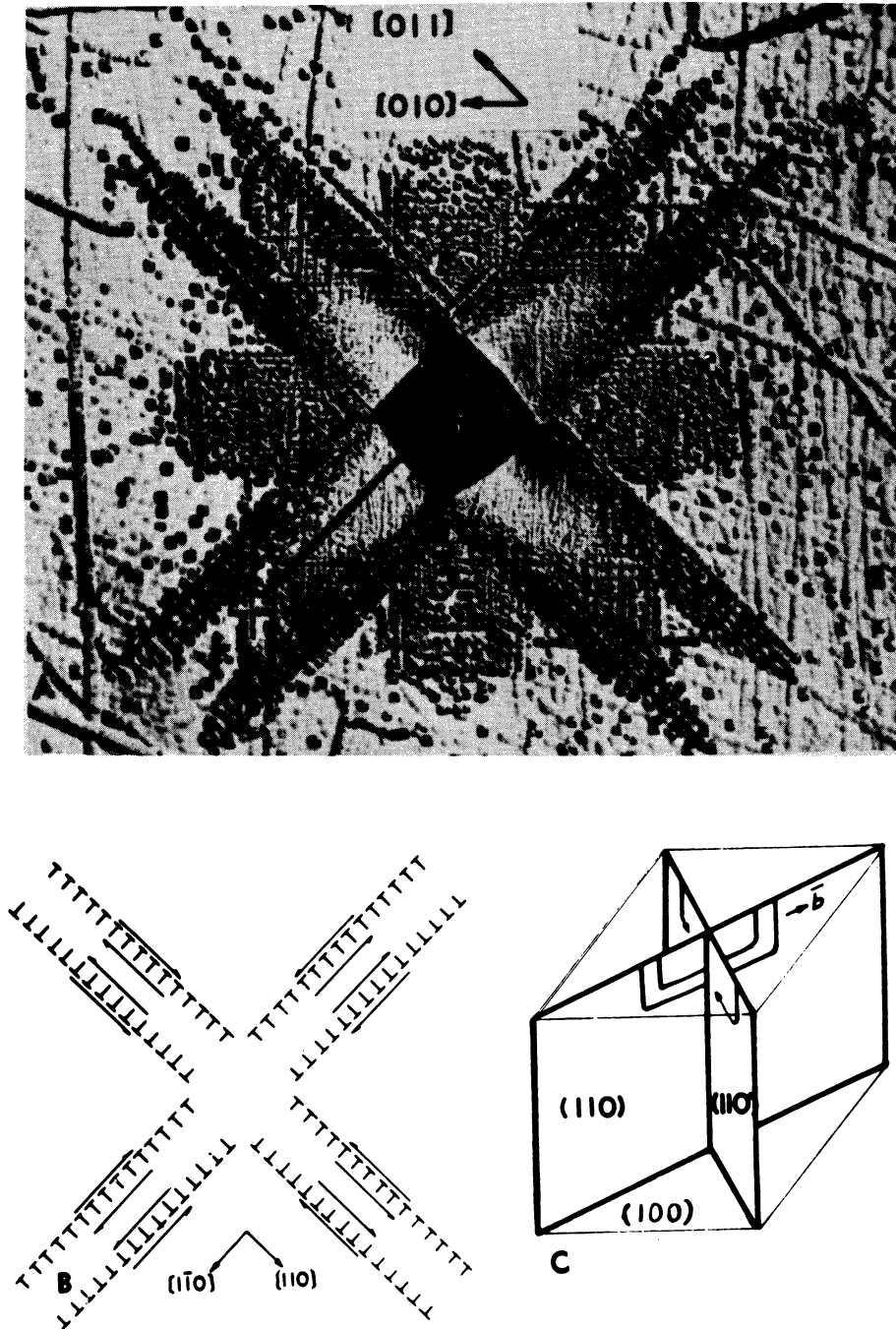


Figure 30. Dislocation etch pit rosette pattern on (001) for MnS. (A) Etched after indentation. X280. (B) Edge dislocations on the  $\{110\}_{90^\circ}$  planes. (C)  $\{110\}_{90^\circ}$  planes and dislocation lines. Burgers vector  $\vec{b}$  is along  $\langle 110 \rangle$ . (Chao *et al.*, 1964a).

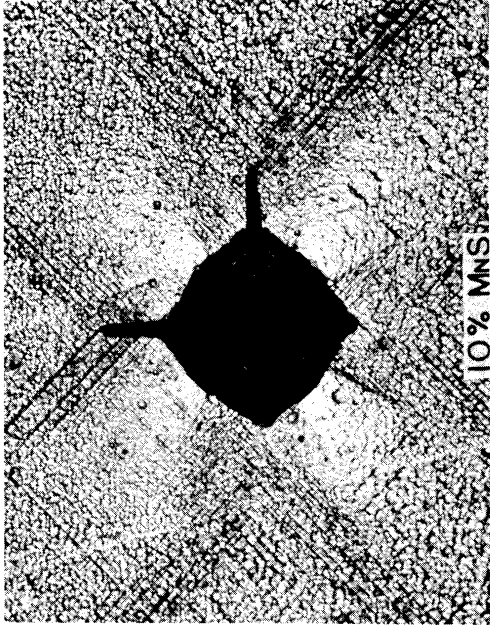
This same etchant also revealed dislocations on the cube faces of MnSe as evidenced by the appearance of random dislocations, small angle boundaries and, for instance, dislocations nucleated at the tip of a moving cleavage crack (Figure 22). Crystal faces other than {001} failed to reveal good etch pits.

Around Vickers impressions on MnSe, however, no rosette pattern developed although random dislocations and small angle boundaries were still in evidence (Figure 31a). Further investigation led to the conclusion that the dislocation mechanism was as important as the surface stability in determining the etchability of the dislocations; that is, apparently only those dislocation lines intersecting {001} with glide plane {110} could be satisfactorily revealed by these etching techniques.

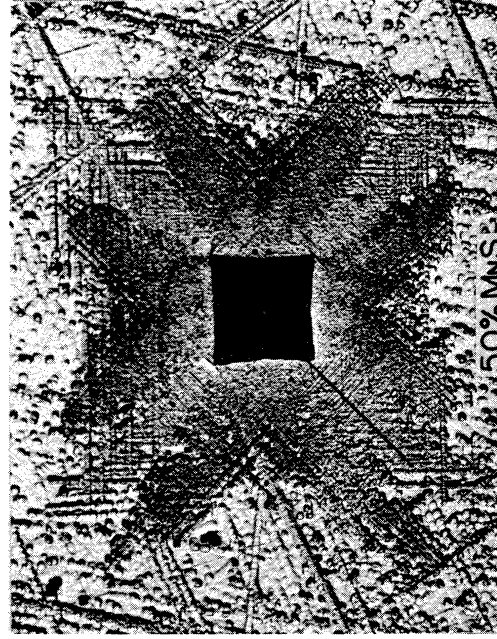
This allowed a study of the change in slip mechanism by observing the development of the rosette pattern characteristic of  $\{110\}\langle\bar{1}\bar{1}0\rangle$  glide. The results are shown in Figures 31a, 31b, 31c, and 31d for Vickers indentations on the (001) plane of MnSe, 90 a/o MnSe-10 a/o MnS, 75 a/o MnSe-25 a/o MnS, and 50 a/o MnSe-50 a/o MnS specimens respectively. The gradual development of the rosette pattern confirms the previous conclusion of a gradual change of primary slip mechanism with composition.

## 2. FRACTURE

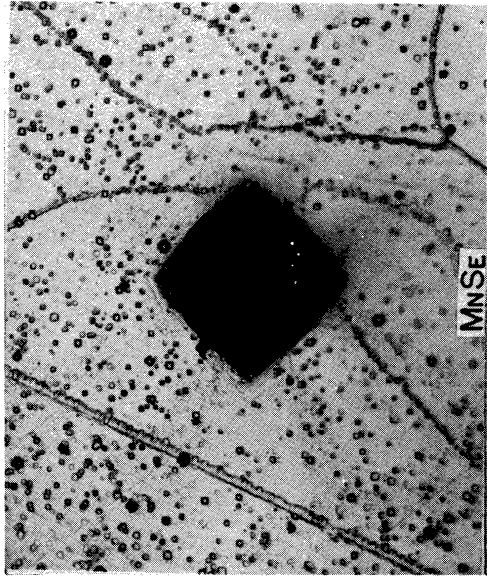
The fracture modes associated with surface indentation also appeared to vary gradually with composition from primarily {100} fracture for MnSe to {110} fracture for MnS. For example, in a specimen of composition 90 a/o MnSe-10 a/o MnS (Figure 31b), {100} fracture was evident while in 50 a/o MnSe-50 a/o MnS



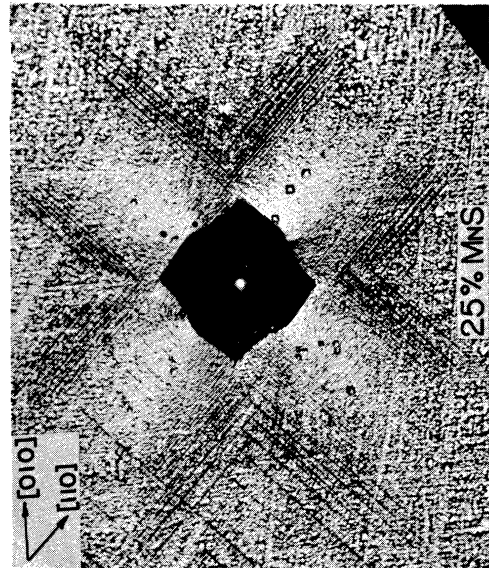
(b)



(d)



(a)



(c)

Figure 31. Development of dislocation etch pit rosette pattern characteristic of  $\{110\}\langle\bar{1}10\rangle$  slip around Vickers indentations for MnSe-MnS solid solutions. X250.

samples both {100} and {110} fracture were observed (Figures 25 and 31d respectively).

### 3. DIAMOND PYRAMID HARDNESS

Figure 32 shows the variation of diamond pyramid or Vickers hardness with composition for MnSe-MnS solid solutions at  $-70^{\circ}\text{C}$ , room temperature, and  $135^{\circ}\text{C}$ . No additional slip mechanisms were found over this  $205^{\circ}\text{C}$  temperature range and it was impossible to tell if significantly different amounts of {110}  $\langle 1\bar{1}0 \rangle$  or {111}  $\langle 1\bar{1}0 \rangle$  glide took place with the temperature variation by the observation of slip traces alone.

Since indentations produced distorted impressions due to pile-up around the indenter, especially on (001) in MnSe, the diagonals varied slightly in length depending on the orientation of the indenter relative to the surface. For (001) tests, the hardnesses reported were measured with the indenter diagonals in  $\langle 100 \rangle$ , giving an impression like that shown in Figure 18a. Under these conditions, the Vickers hardnesses on the (001), (011), and (111) planes were the same within the  $\pm 4\%$  limits of the experimental error.

Manganese selenide is softer than manganese sulfide ( $47 \text{ kg/mm}^2$  vs.  $145 \text{ kg/mm}^2$  at  $20^{\circ}\text{C}$ ). In addition there is a large positive deviation from linearity in the solid solution hardening which accompanies the substitution of sulfide for selenide ions. The substitution of selenide for sulfide ions also produces a positive, although somewhat smaller, deviation. There is no special significance attached to the maximums which appear other than that they represent an averaging out of the two solid solution hardening effects.

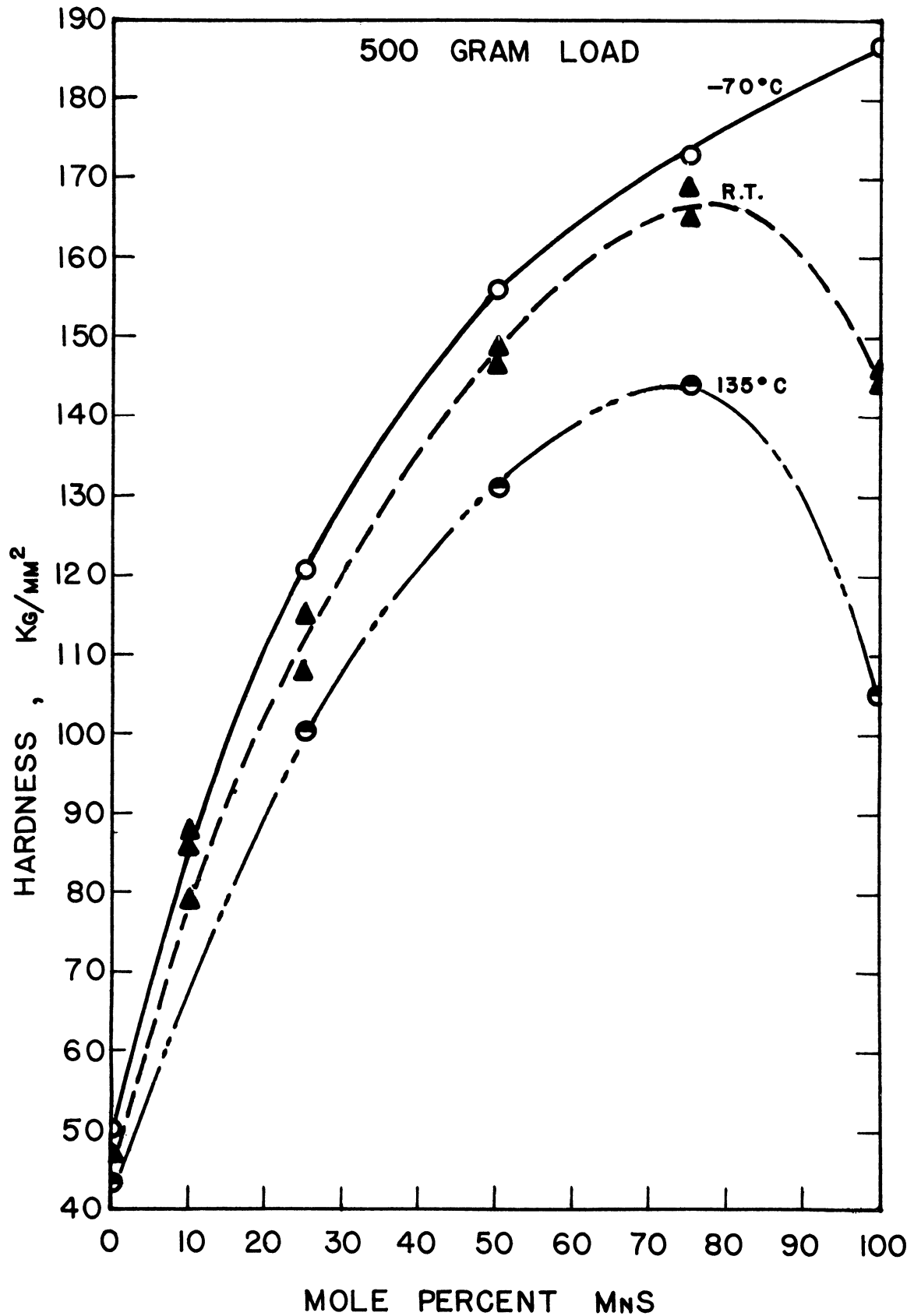


Figure 32. Average diamond pyramid hardness of MnSe-MnS solid solutions at various temperatures.

It is also evident that the hardness of MnSe is much less sensitive to temperature than that of MnS. The behavior of MnSe apparently is similar to that of FCC metals which maintain their ductility down to very low temperatures. The hardness of the selenide changed about 0.04%/°C while for the sulfide it varied about 0.14%/°C based on room temperature hardness values.

A cross-plot of the hardness vs. temperature curves is shown in Figure 33. For MnS, satisfactory hardness results were obtained at liquid nitrogen temperature (-196°C). It was found that the DPH dropped off somewhat from its previously linear DPH-temperature behavior. Observation of the impressions made under liquid nitrogen showed significant amounts of {111} slip with extensive {110}<sub>90°</sub> cracking. This is shown in Figure 34. Once again it should be pointed out that the oblique lighting technique enhances the visibility of some slip traces but decreases the visibility of others.

The {111} slip traces can be explained as follows. The {110}< $\bar{1}\bar{1}0$ > slip mechanism, characteristic of MnS, apparently hardens much more with decreasing temperature than the {111}< $\bar{1}\bar{1}0$ >, and it thus becomes possible to reach temperatures where {111}< $\bar{1}\bar{1}0$ > slip, the secondary mechanism at room temperature, can be just as easily activated in appreciable amounts as {110}< $\bar{1}\bar{1}0$ > glide.

The hardness-temperature curve for MnS agrees well with the hot hardness results of Chao et al. (1964b) over the temperature range in common.

Attempts were also made, without success, to study MnSe and the other compositions at liquid nitrogen temperature. When MnSe was cooled to -196°C either by quenching or slow cooling, whether mounted or unmounted, the surface was striated and cracked, similar to that which is shown in Figure 35. The



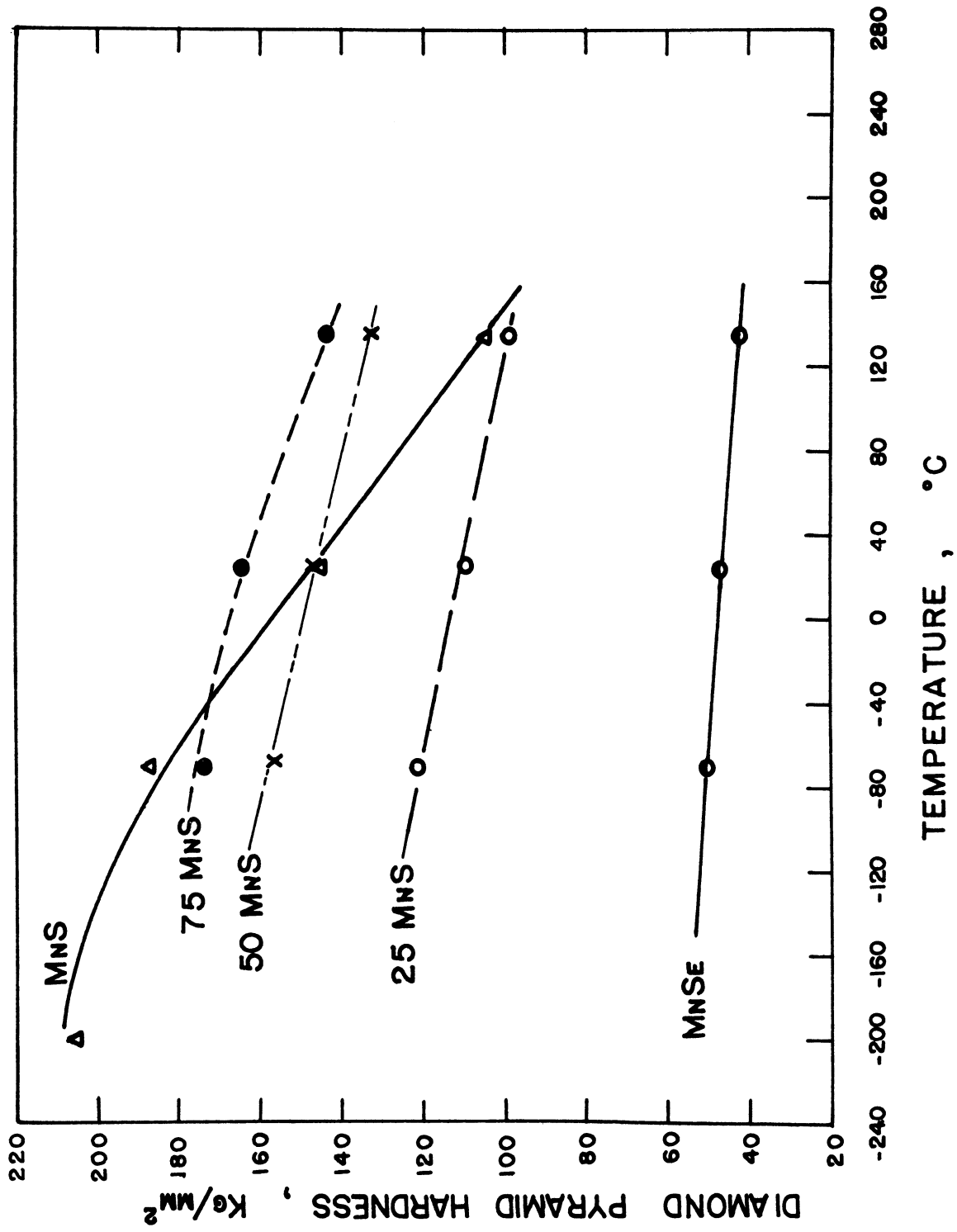


Figure 33. Diamond pyramid hardness vs. temperature for MnSe-MnS solid solutions.

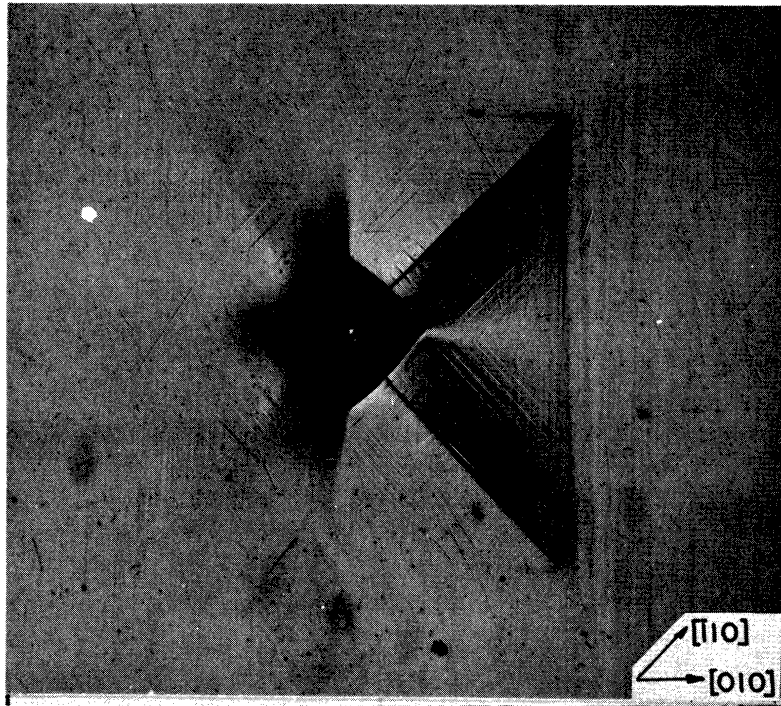


Figure 34. Vickers impression (500 gm load) made under liquid nitrogen on the (001) surface of MnS single crystal. Oblique lighting. X250.

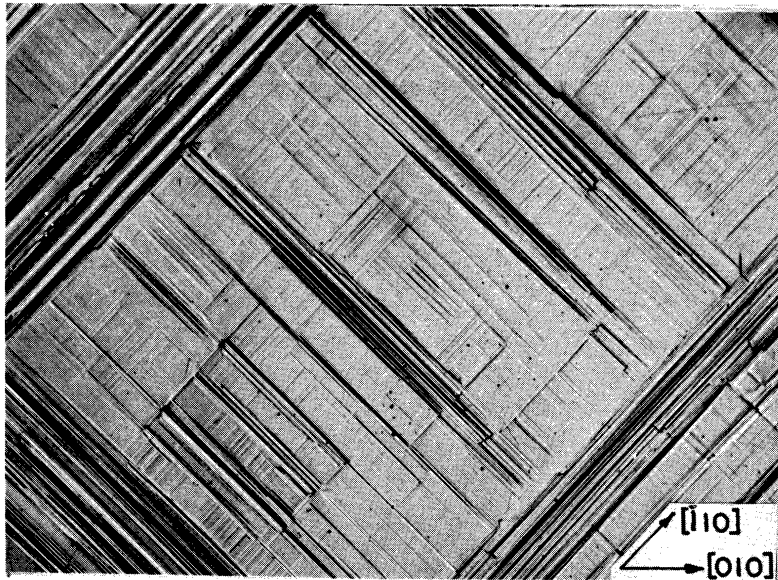


Figure 35. The (001) surface of MnSe after quenching in liquid nitrogen. X250.

room temperature hardness after cycling was around  $80 \text{ kg/mm}^2$  while at  $-196^\circ\text{C}$  it measured about  $300 \text{ kg/mm}^2$ . Similar results, but less drastic, were also obtained with the other compositions except for MnS.

This suggests the possibility of a polymorphic phase change in addition to the antiferromagnetic transformation already known to exist. This explanation was offered by Lindsay (1951) and Makovetski and Sirota (1963) in an effort to explain anomalous behavior in low temperature magnetic susceptibility and thermal expansion measurements. Neither was able to explain the nature of any second phase.

In a more recent paper, however, Makovetski and Sirota (1966), using neutron diffraction, discovered that MnSe transforms to its sphalerite (cubic ZnS) modification at low temperatures. They found, in experiments at  $-158^\circ\text{C}$ , that both the antiferromagnetic form of  $\alpha$ -MnSe (NaCl-type) and  $\beta$ -MnSe (sphalerite modification) were present together, and that the amount of each varied depending on the thermal history of the sample.

Attempts were made to obtain low temperature back-reflection Laue X-ray photographs of single crystals of MnSe by dripping liquid nitrogen on them during exposure. These results were inconclusive. A slightly different looking cubic pattern was found which may have been twinned but which, for the most part, corresponded quite closely to that found at room temperature. It was found that the crystal could be repeatedly cycled and still remain as a single crystal. However, because of the small region of the stereographic net covered by the photograph and because of the similarity of the two patterns, no conclusive results could be obtained.

An attempt was also made to get a diffractometer trace of a powder specimen while cooling with liquid nitrogen. This too was not successful.

The best results were obtained by blowing evaporated nitrogen gas over a powder specimen in a Debye-Scherrer camera as shown previously in Figure 11. Relatively good temperature control was attained ( $\pm 4^\circ\text{C}$ ), but the lowest temperature achieved was  $-130^\circ\text{C}$  and a powder pattern at that temperature showed no new phases. In fact, although the lines on the photograph were sharp, no line splitting or broadening was observed resulting from a slight atom shift characteristic of the antiferromagnetic transformation (Shull et al., 1951; Tombs and Rooksby, 1950, 1951) which is supposed to take place about  $-120^\circ\text{C}$ . It was possible to calculate the thermal expansion coefficient from lattice parameter measurements. This was  $18.5 \times 10^{-6}/^\circ\text{C}$  and agrees well with a value  $18.0 \times 10^{-6}/^\circ\text{C}$  determined by Makovetski and Sirota (1963).

#### 4. KNOOP HARDNESS

The variation of Knoop hardness with orientation of the long axis of the indenter on anisotropic materials is a well known phenomenon (see Literature Review). On single crystal specimens, the hardness anisotropy is some complicated function of the particular slip systems of the crystal most favorably oriented to accommodate the shape change imposed by the indenter. Because of the difference in primary slip mechanism, this function is different for MnSe than for MnS. The room temperature Knoop hardness results for these materials are tabulated in Tables I and II, where it is seen, for instance, that, on the (001) plane, MnSe is softer when the long axis of the indenter is parallel to  $\langle 110 \rangle$  than when it is aligned in  $\langle 100 \rangle$ . The reverse is true for MnS.

TABLE I

## KNOOP HARDNESS OF MnSe

Plane of Indentation	Direction of Long Axis of Indenter			
	$\langle 100 \rangle$	$\langle 110 \rangle$	$\langle 111 \rangle$	$\langle 112 \rangle$
{001}	65.	43.		
{011}	73.	48.	54.	54.
{111}		57.		57.

TABLE II

## KNOOP HARDNESS OF MnS

Plane of Indentation	Direction of Long Axis of Indenter			
	$\langle 100 \rangle$	$\langle 110 \rangle$	$\langle 111 \rangle$	$\langle 112 \rangle$
{001}	122	142		
{011}	119	142	142	140
{111}		140		140

Recently, Garfinkle and Garlick (1967) observed that the variation of Knoop hardness with crystallographic orientation depended mainly on the direction of the long axis and not on the plane of the indentation; that is, if  $\langle uvw \rangle$  is a hard direction on one plane, it will also be a hard direction on another plane. This is seen to be approximately true for MnSe and MnS also, even though "hard" and "soft" directions are reversed for each.

It thus becomes possible to follow the transition of primary glide mechanism in the MnSe-MnS solid solution series by plotting the Knoop hardnesses for two indenter orientations. Room temperature results are shown in Figures 36 and 37 for two indenter orientations on the (001) and (011) planes. The

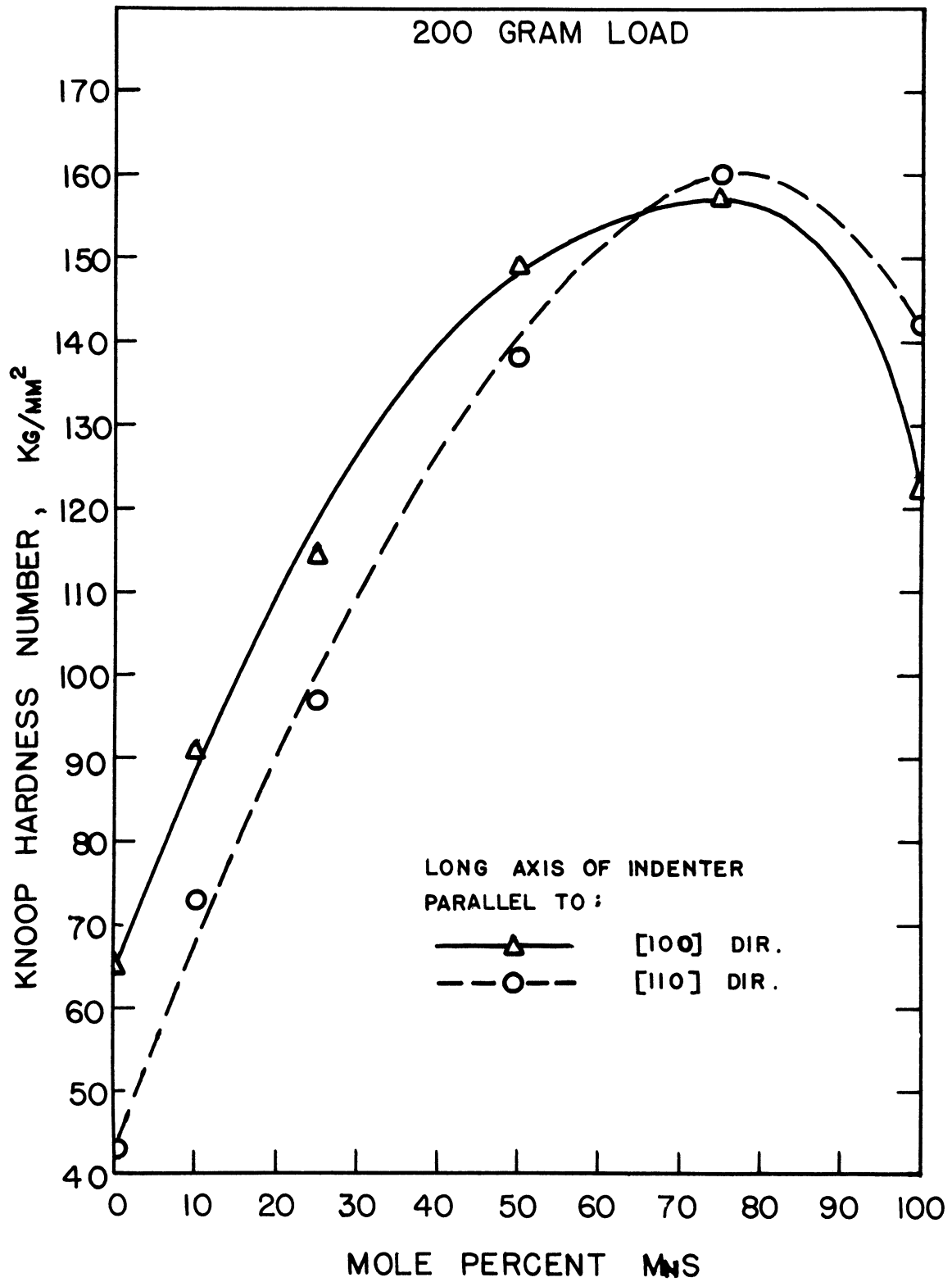


Figure 36. Room temperature Knoop hardnesses on (001) for MnSe-MnS solid solutions.

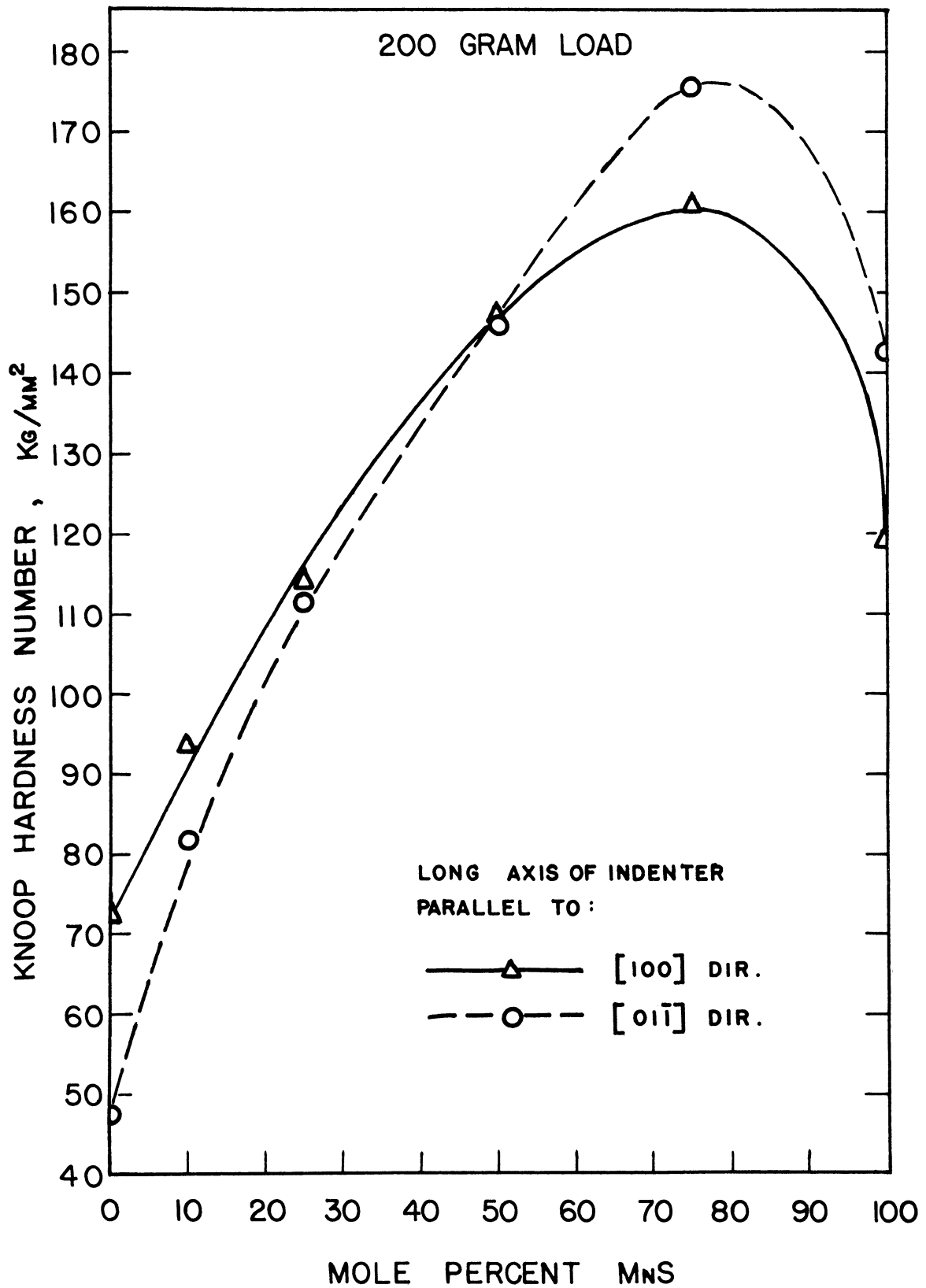


Figure 37. Room temperature Knoop hardnesses on (011) for MnSe-MnS solid solutions.

behavior shown on both plots is essentially the same—a cross-over occurs and the general shape of the curves is like that for the Vickers hardness vs. composition plot.

Figure 38 indicates that similar tests at  $-70^{\circ}\text{C}$  on the (001) plane showed a slight increase in the hardness of the selenide but a marked increase in the sulfide hardness, and resulted in a shift of the cross-over point of the two curves toward higher percentages of MnS. Conversely, Figure 39 shows that increasing the temperature lowered the hardness of MnSe slightly, drastically lowered the hardness of MnS from its room temperature value, and shifted the cross-over to the left.

Again the results show the  $\{110\}\langle\bar{1}\bar{1}0\rangle$  glide mechanism to be much more temperature sensitive than the  $\{111\}\langle\bar{1}\bar{1}0\rangle$ . This would mean that, with decreased temperature, the  $\{111\}\langle\bar{1}\bar{1}0\rangle$  system should give a greater contribution to the overall deformation for all compositions and the cross-over should be shifted to the right—the effect actually observed. Alternately, at higher temperatures, the Knoop anisotropy characteristic of  $\{110\}\langle\bar{1}\bar{1}0\rangle$  slip should extend over a greater range of compositions as  $\{110\}\langle\bar{1}\bar{1}0\rangle$  deformation becomes greater and the cross-over should be shifted to the left—again the effect actually observed. The results appear consistent.

It is interesting to speculate on the nature of the deformation associated with Knoop indentations on single crystal specimens and to try to postulate relative hardnesses as a function of indenter orientation. This is an extremely complicated problem and its consideration will be reserved for the Discussion portion of this work.



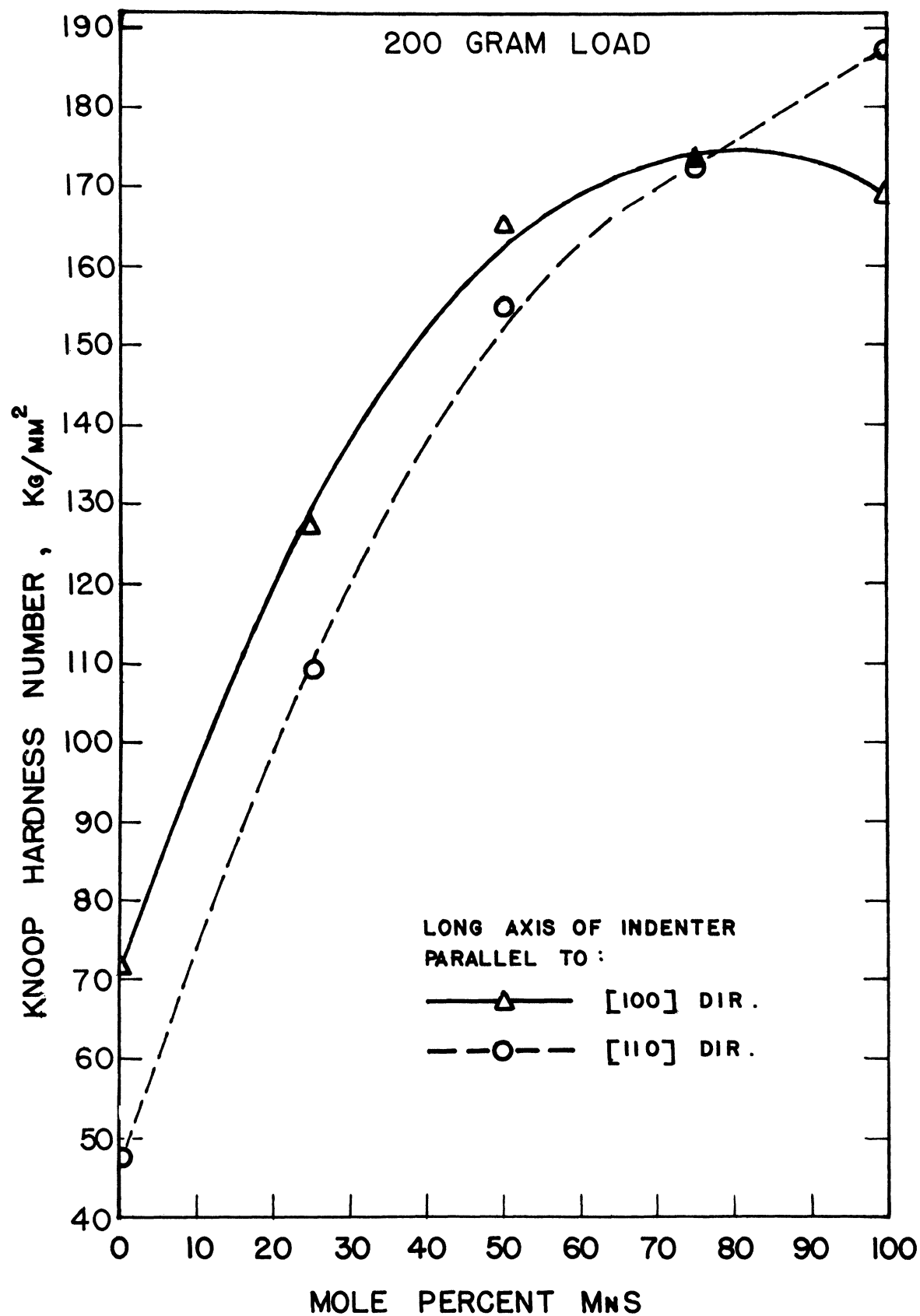


Figure 38. Knoop hardnesses on (001) for MnSe-MnS solid solutions at  $-70^{\circ}\text{C}$ .

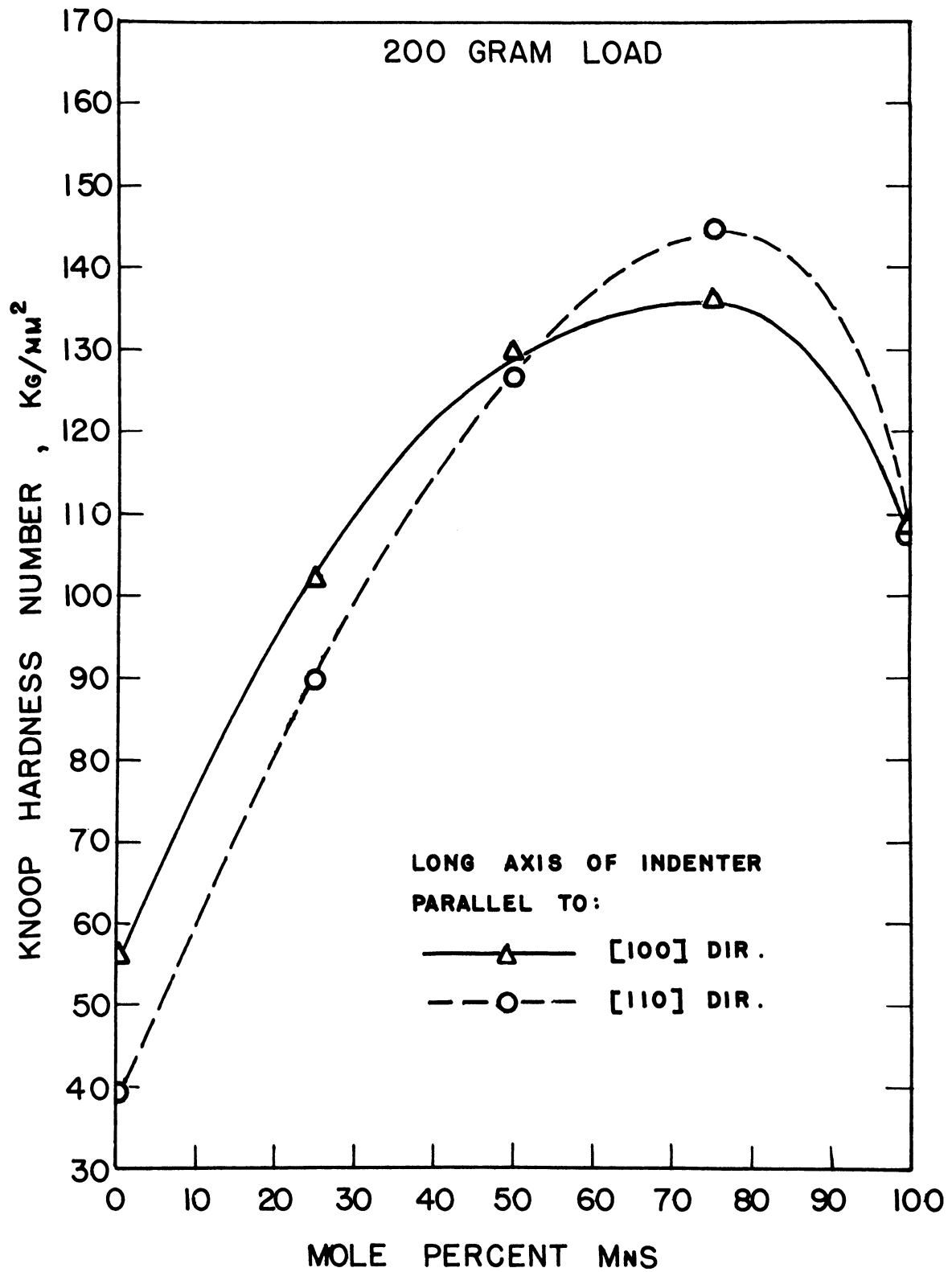


Figure 39. Knoop hardnesses on (001) for MnSe-MnS solid solutions at 135°C.

## C. MnSe-Rich Portion of MnSe-MnTe System

## 1. PLASTIC DEFORMATION

Panson and Johnston (1964) studied the system MnSe-MnTe (Figure 6) and found that tellurium could be substituted for selenium in the MnSe lattice to the extent of about 15 a/o at temperatures below 500°C.

In this investigation, samples containing 7 a/o and 13 a/o MnTe were studied and both compositions showed slip traces due to  $\{111\}\langle\bar{1}\bar{1}0\rangle$  and  $\{110\}\langle\bar{1}\bar{1}0\rangle$  glide. Figure 40 is a Vickers indentation on the (001) plane of a 93 a/o MnSe-7 a/o MnTe specimen where it was found that  $\{110\}$  glide was somewhat more extensive than that observed in 90 a/o MnSe-10 a/o MnS samples. Figure 41 of a Knoop impression on the (011) plane of a sample of the same composition, however, revealed traces due only to  $\{111\}$  slip. This is a consequence of the ease of accommodating most of the lateral displacement caused by the indenter by simple  $\{111\}$  slip on each side of it. Figure 42 shows slip traces around a Vickers indentation on the {011} plane of an 87 a/o MnSe-13 a/o MnTe sample where both  $\{111\}$  and  $\{110\}$  glide are evident.

## 2. FRACTURE

As with pure MnSe, both compositions showed primarily  $\{100\}$  cleavage with some  $\{110\}$  cleavage evident in crushed fragments. Around surface indentations it was found that  $\{110\}_{90^\circ}$  fracture occurred somewhat more frequently than the  $\{100\}$  fracture characteristic of MnSe, especially in the 13 a/o MnTe samples.

## 3. DIAMOND PYRAMID HARDNESS

While the Vickers hardness was essentially the same on the (001), (011),

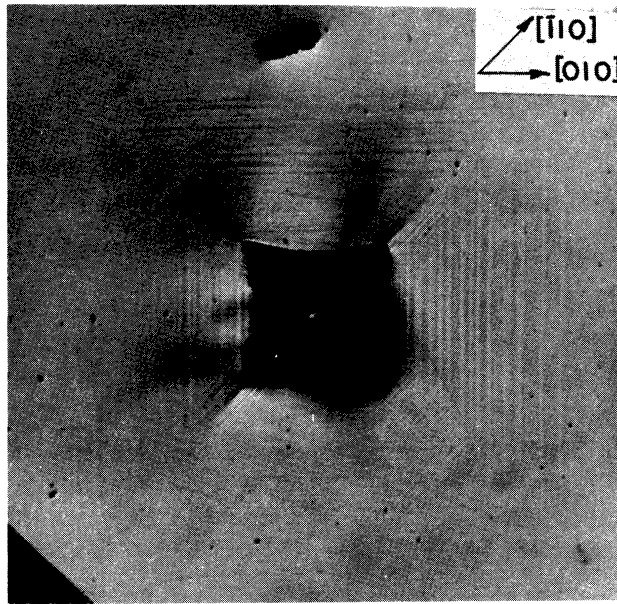


Figure 40. Slip traces around Vickers impression (500 gm load) on the (001) surface of 93 MnSe—7 MnTe crystal. Oblique lighting. X250.

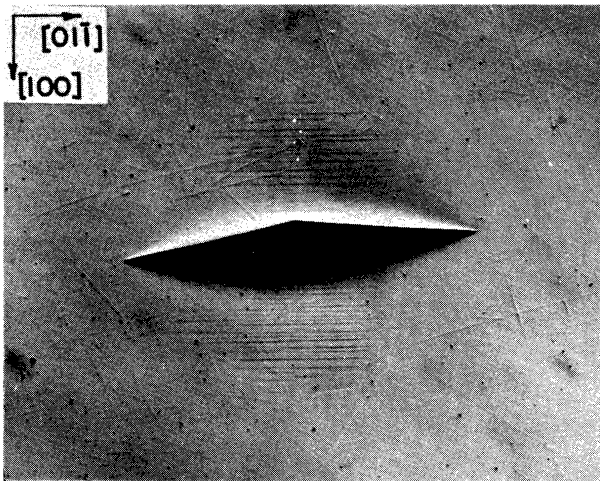


Figure 41. Slip traces around Knoop indentation on the (011) surface of 93 MnSe—7 MnS crystal. Oblique lighting. X250.

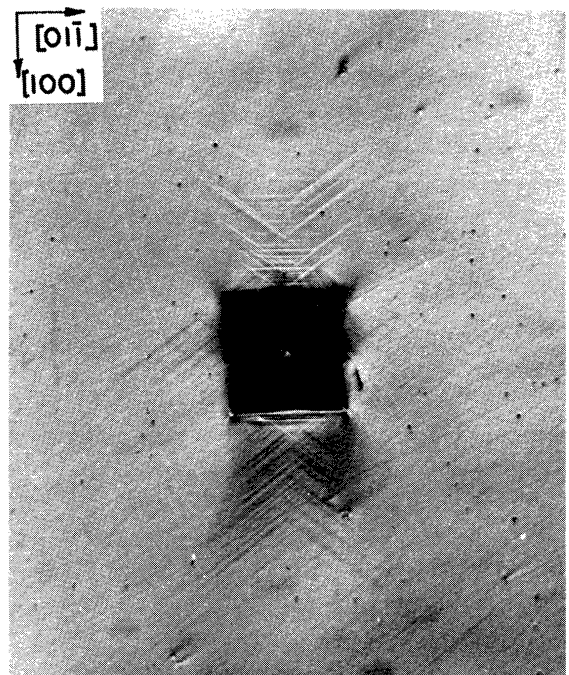


Figure 42. Slip traces around Vickers indentation (500 gm load) on the (011) surface of 87 MnSe—13 MnTe crystal. Oblique lighting. X250.

and (111) planes, the values for the two compositions were higher than the values observed for comparable substitutions of sulfide for selenide ions. This is shown graphically in the left hand portion of Figure 43. The size of the tellurium ion is 2.11Å (Goldschmidt) vs. 1.91Å for the selenide ion and 1.74Å for the sulfide. Thus, the size difference between S<sup>-2</sup> and Se<sup>-2</sup> (based on the Se<sup>-2</sup> radius) is 8.9% while that between Te<sup>-2</sup> and Se<sup>-2</sup> is about 10.5%. This slightly larger mismatch in the case of the telluride ion may be enough to cause the higher rate of hardening observed.

#### 4. KNOOP HARDNESS

The Knoop hardness results for both compositions followed the pattern observed for Vickers hardness. The left side of Figure 44 gives results for the (001) plane where, as with pure MnSe, the hardness is lowest when the long axis of the indenter is aligned parallel to <110>. Also, like the Vickers hardness results, the rate of hardening is greater than that observed during the substitution of sulfide for selenide ions. Similar results were found on the (011) plane.

### D. Manganous Telluride

#### 1. PLASTIC DEFORMATION

Three modes of plastic deformation were observed in MnTe. Indentation of the basal plane produced patterns which could be attributed to {10 $\bar{1}$ 2} twinning and which were exactly like those observed by Partridge and Roberts (1964) on single crystals of magnesium. Twinning on {10 $\bar{1}$ 2} planes is common

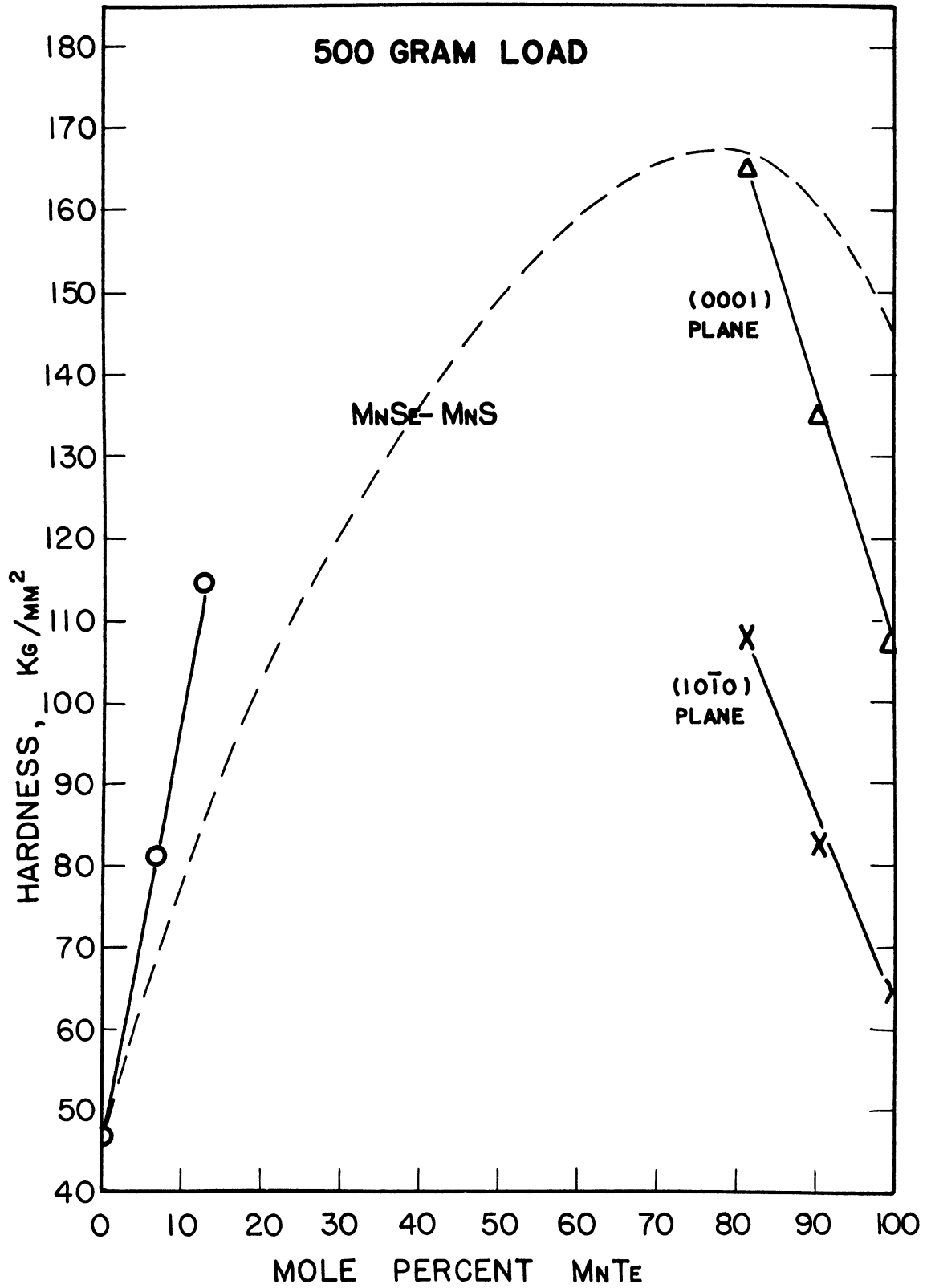


Figure 43. Diamond pyramid hardnesses for  $\text{MnSe-MnTe}$  solid solutions with results for the  $\text{MnSe-MnS}$  system added for reference.

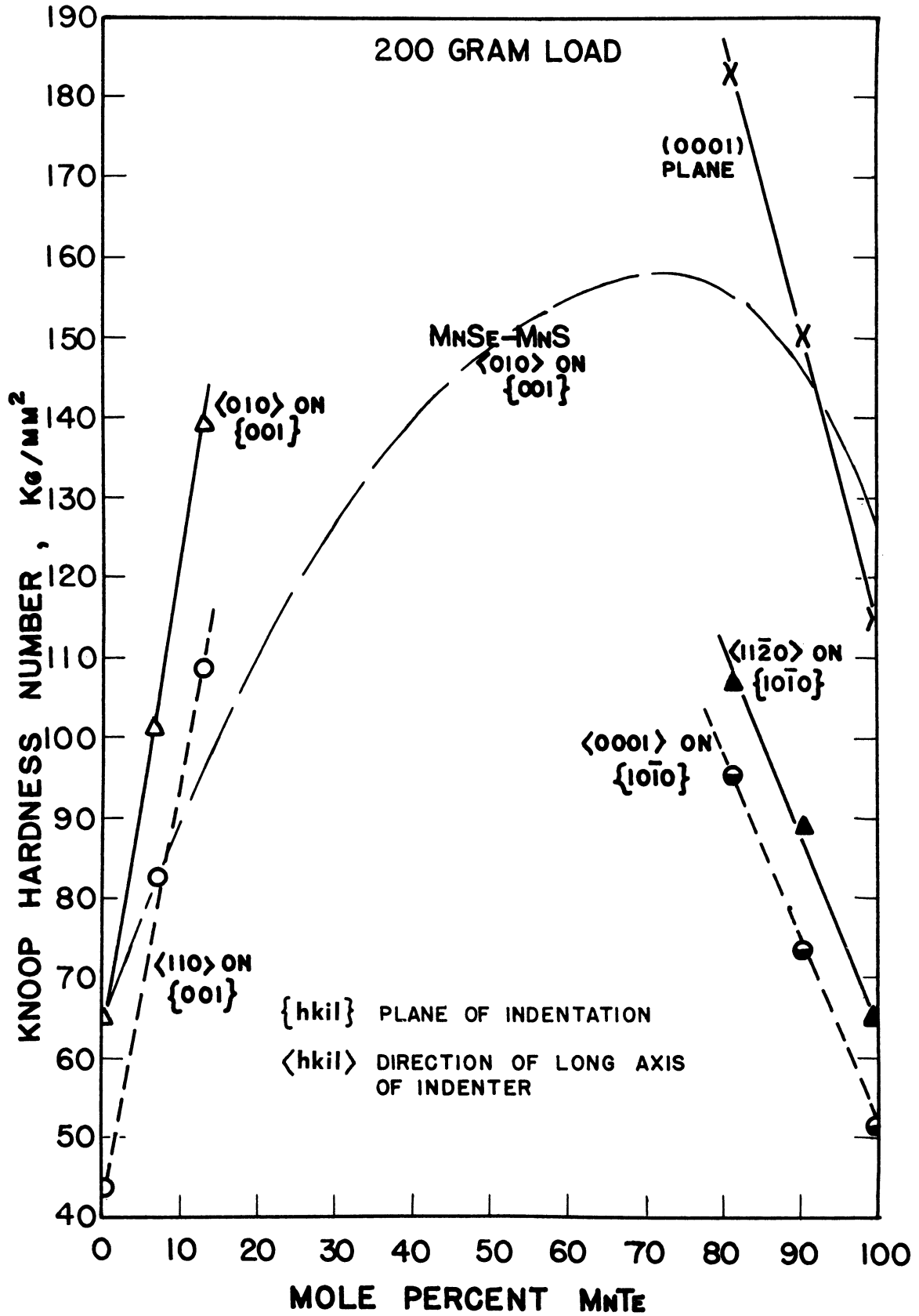


Figure 44. Knoop hardnesses for MnSe-MnTe solid solutions. Some results for the MnSe-MnS system are added for reference.

with HCP metals (Barrett, 1952) and geometric construction has shown that it can also occur in the compound MnTe. Basal indentations are shown in Figures 45 and 46 and the possible orientations of  $\{10\bar{1}2\}$  twin traces on the basal plane in Figure 47. The appearance of the twinning on only one side of the indenter reflects a slight misorientation of the surface which, as explained previously, because of the difficulty in growing the crystals, was accurate for the basal planes to within only about three or four degrees. It was noted that different twin systems could be activated by changing the orientation of the indenter on the surface. While reoriented twinned material may provide planes that are more favorably oriented for further deformation by slip, no slip traces were observed in these regions. In fact, no slip traces at all were seen on the basal plane, giving evidence for a  $\langle 11\bar{2}0 \rangle$  slip vector.

Interference photomicrographs showing surface contours around Vickers impressions on (0001) revealed that a general sinking-in or compaction took place all around the indentation (Figure 48). The interference fringes showed 6-fold symmetry with the sides of the hexagon rotated 30 degrees from  $\langle 11\bar{2}0 \rangle$  directions. Twinned regions were higher than untwinned regions which is as expected since  $\{10\bar{1}2\}$  twinning produces an elongation along the c-axis with  $c/a < \sqrt{3}$ . The few piled-up regions that were observed (e.g., points A and B in Figure 48) occurred at or near locations of extensive twinning. The reason(s) for the general sinking-in is not understood however.

Vickers indentations on  $(10\bar{1}0)$  and  $(11\bar{2}0)$  planes revealed extensive amounts of basal slip as indicated by traces parallel to  $[\bar{1}100]$  in Figure 49. Also observable in Figure 49 are semicircular wavy lines extending out  $[\bar{1}100]$  direc-



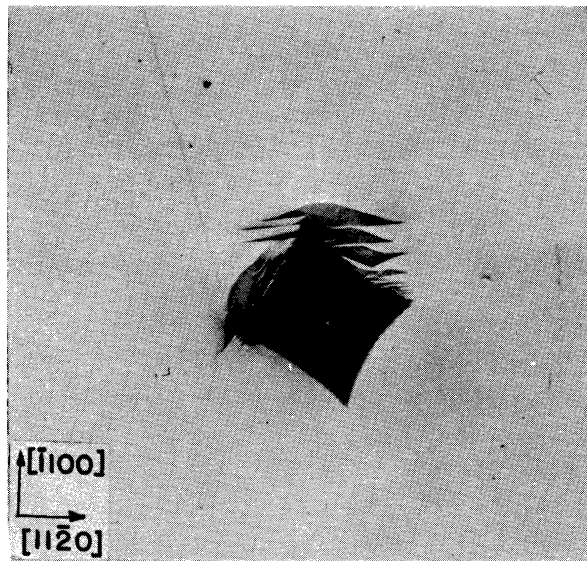


Figure 45. Twinning around Vickers indentation (500 gm load) on the (0001) surface of MnTe crystal. Oblique lighting. X250.

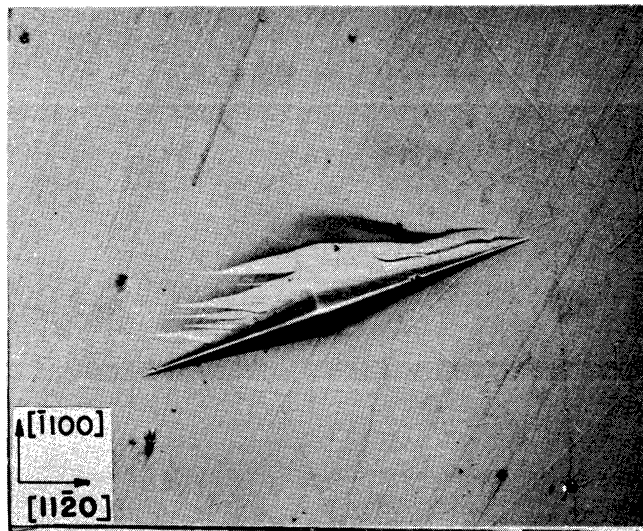


Figure 46. Twinning around Knoop impression on the (0001) surface of MnTe crystal. Oblique lighting. X500.

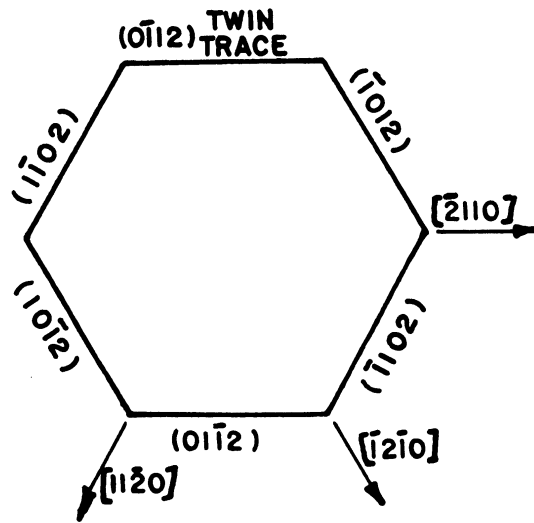


Figure 47. Possible orientations of  $\{10\bar{1}2\}$  twin traces in the basal plane of MnTe.

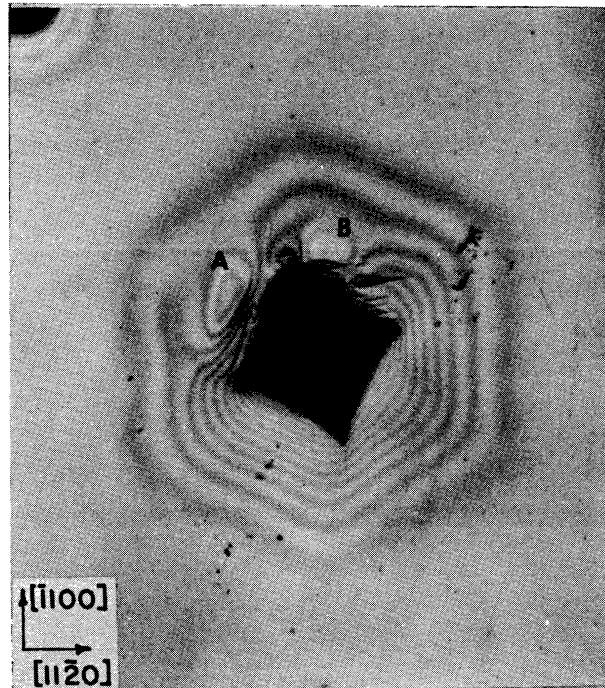


Figure 48. Interference micrograph around Vickers impression on the  $(0001)$  surface of MnTe. X250.

tions. This is shown more dramatically for two orientations of the Knoop indenter on  $(10\bar{1}0)$  in Figures 50a and 50b. In Figure 50a, with the indenter parallel to  $[\bar{1}2\bar{1}0]$ , the basal slip is observed, but for the indenter rotated 90 degrees, the wavy slip lines are seen. These are attributed to pencil glide—that is, slip taking place on numerous planes having the slip direction, which most probably is  $\langle 11\bar{2}0 \rangle$ , as zone axis. Deformation by simultaneous slip on many planes using a common slip direction may also be described as extensive cross slip and is quite common at elevated temperatures for many materials (e.g., Mg (Bakarian and Mathewson, 1943) and Al (Petty, 1963)). Wavy slip lines have also been observed at room temperature in AgCl (Gilman, 1961a), AgBr (Gilman, 1961a),  $\alpha$ -Fe (Barrett, 1952), and Hg (Greenland, 1937). Manganese telluride itself is quite soft (DPH = 65) and consequently is labeled as a material in which dislocations can move fairly easily. It thus becomes apparent that MnTe provides the additional slip systems necessary to accommodate the indenter by this sort of extensive cross slip mechanism, otherwise called pencil glide.

No twinning was evident on the prism planes.

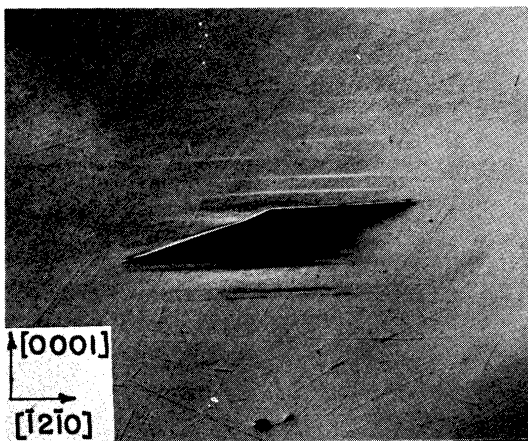
## 2. FRACTURE

The primary cleavage plane in MnTe was  $\{0001\}$  and fracture on this plane revealed bright shiny surfaces. It was also possible to induce  $\{10\bar{1}0\}$  cleavage with a knife edge revealing a lusterless surface. Both types of fracture were evident in crushed fragments.

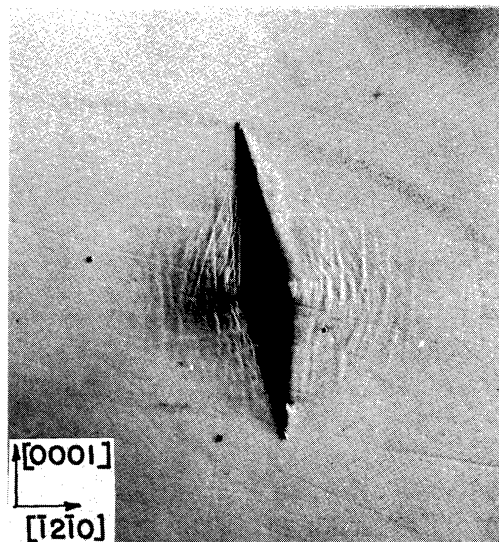
Around surface indentations, both  $\{0001\}$  and  $\{10\bar{1}0\}$  fracture were common at low indenter loads, but irregular cracking, which could not be inter-



Figure 49. Slip traces around Vickers indentation (500 gm load) on the  $(11\bar{2}0)$  surface of MnTe. Oblique lighting.  
X150.



(a)



(b)

Figure 50. Slip traces around Knoop impressions on  $(10\bar{1}0)$  surfaces of MnTe single crystal with (a) long axis almost parallel to  $[\bar{1}2\bar{1}0]$  and (b) long axis about parallel to  $[0001]$ . Oblique lighting.  
X250.

preted, developed at higher loads.

### E. MnTe-Rich Portion of MnSe-MnTe System

#### 1. PLASTIC DEFORMATION

Figure 6 indicates that the maximum solid solubility of manganese selenide in the telluride at room temperature is less than 20 a/o. Two compositions studied in the single phase region were 91 a/o MnTe-9 a/o MnSe and 81 a/o MnTe-19 a/o MnSe and both showed the same three modes of plastic deformation as found in pure MnTe, namely,  $\{10\bar{1}2\}$  twinning, basal glide, and pencil glide in  $\langle 11\bar{2}0 \rangle$ .

#### 2. FRACTURE

The fracture mechanisms were also the same as those found in pure MnTe— $\{0001\}$  and  $\{10\bar{1}0\}$  cleavage.

#### 3. DIAMOND PYRAMID HARDNESS

The diamond pyramid hardness results for the single phase MnTe-rich portion of the MnSe-MnTe system are indicated in the right hand portion of Figure 43.

The DPH on (0001) is about 65% greater than that on (10 $\bar{1}$ 0) for pure MnTe (107 kg/mm<sup>2</sup> vs. 65 kg/mm<sup>2</sup>) and about 53% greater for the 81 a/o MnTe-19 a/o MnSe sample (165 kg/mm<sup>2</sup> vs. 108 kg/mm<sup>2</sup>). The higher hardness of the basal plane reflects the difficulty of activating slip systems capable of moving material up to the surface to make room for the indenter—something which can-

not be done by glide in  $\langle 11\bar{2}0 \rangle$  directions alone because they are all parallel to (0001) and surrounding material strongly constrains such movement. The rate of hardening on both planes was greater than that found when MnSe was added to MnS, as shown.

#### 4. KNOOP HARDNESS

Knoop hardness results for the system are shown in the right hand portion of Figure 44. All orientations of the indenter on the basal plane gave the same hardness within the limits of the experimental error. The basal hardness was about 80% greater than for the orientation  $[\bar{1}2\bar{1}0]$  on  $(10\bar{1}0)$  for pure MnTe (115 kg/mm<sup>2</sup> vs. 64 kg/mm<sup>2</sup>) and 72% greater for the 81 a/o MnTe-19 a/o MnSe sample (184 kg/mm<sup>2</sup> vs. 107 kg/mm<sup>2</sup>). The orientation  $[\bar{1}2\bar{1}0]$  on  $(10\bar{1}0)$  was slightly harder than [0001] on  $(10\bar{1}0)$  which reflects the larger number of slip systems activated by pencil glide characteristic of the latter orientation than can be supplied by basal slip which tends to be activated by the former orientation (Figures 50a and 50b).

Similar tests on the  $(11\bar{2}0)$  planes gave results virtually identical to those found on  $(10\bar{1}0)$ .

## CHAPTER V

### DISCUSSION

#### A. Deformation Associated with the Vickers Indentation

Around a Vickers indentation one would normally expect the slip and pile-up to be the most pronounced at the center of each of the four sides of the indenter regardless of orientation, since it is near these regions under the indenter where the greatest material displacements must occur. Tolansky and Nickols (1949a) found this to be the case for polycrystalline, nearly isotropic specimens of sintered tungsten carbide and selected steels. When they tested single crystals of tin, however, they found a crystallographic distortion resulting in a piling-up and sinking-in of material around the indentation (Tolansky and Nickols, 1949b, 1954).

These and other results are similar to the pile-up and sinking-in reported here for MnSe (Figures 18a and 18b) and MnS (Figures 20a and 20b) and must be related to the nature of the plastic flow taking place on the individual slip systems of the single crystal specimens.

Figure 51 indicates how the pile-up might be related to the plastic flow taking place around the indenter for MnSe. Since the slip occurs on  $\{111\}$  planes, the nature of the pile-up on the  $\{001\}$  planes would imply that the glide direction is  $\langle 112 \rangle$ . The Burgers vector in  $\langle 112 \rangle$ , however, is  $\sqrt{3}$  times that for  $\langle 110 \rangle$  glide and from geometric considerations one can conclude that  $\langle 110 \rangle$  slip is much more likely than slip in  $\langle 112 \rangle$ . Thus slip in two  $110$

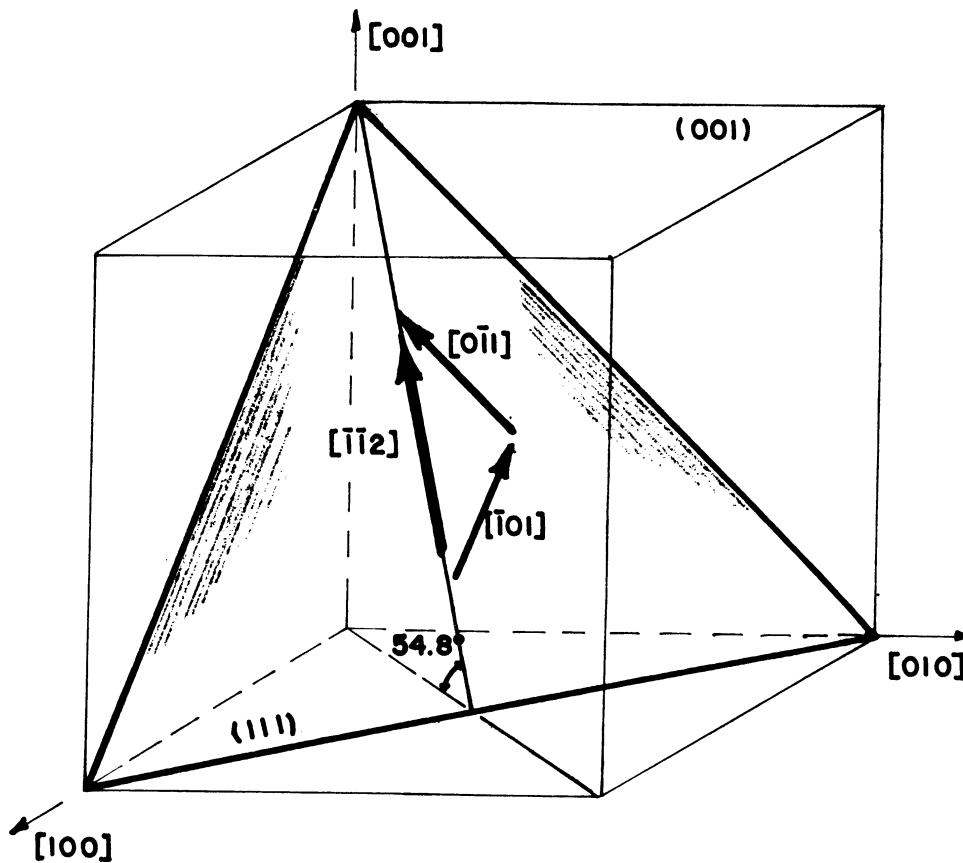


Figure 51. View of a  $\{111\}$  plane showing how flow in two  $\langle 110 \rangle$  directions can result in net  $\langle 112 \rangle$  movement.

steps seems much more feasible than a  $\langle 112 \rangle$  motion and could result in exactly the same net displacement, as shown in Figure 51.

This same sort of pile-up was previously observed by Keh (1960) on MgO when indented at high temperatures and on MnS as previously mentioned. Both these compounds possess the  $\{110\}\langle 1\bar{1}0 \rangle$  primary slip mechanism. Keh (1960) attempted to relate these hills and slip line concentrations to dislocation interactions. Dislocations on neighboring  $\{110\}$  planes at  $45^\circ$  to  $\{001\}$  [designated  $\{110\}_{45^\circ}$ ] interact and tend to pile-up. If the temperature is high enough and the dislocations can acquire enough energy, some segments of the piled-up



dislocations will cross glide on other  $\{110\}_{45^\circ}$  planes and form new dislocation sources on parallel glide planes. Thus dislocation pile-up and subsequent cross slip could lead to a movement of material that is equivalent to slip on two adjacent  $\{110\}_{45^\circ}$  planes, each of which has one  $\langle 110 \rangle$  slip direction. The overall effect would be a net displacement of material in a  $\langle 112 \rangle$  direction in the same manner as for MnSe except that now slip must take place on two planes of the  $\{110\}$  type instead of being able to occur in two  $\langle 110 \rangle$  directions on a single  $\{111\}$  plane.

An additional factor must be considered in the case of MnS and MgO however. Von Mises (1928) showed that for general homogeneous strain, the operation of five independent slip systems is necessary. The  $\{110\}\langle 1\bar{1}0 \rangle$  primary glide mechanism can provide only two (Groves and Kelly, 1963). This means that some other slip mechanisms must necessarily be operating in order to produce the shape change imposed by the indenter. Chao et al. (1964a) identified  $\{111\}\langle 1\bar{1}0 \rangle$  as a secondary slip mechanism in MnS. Although direct evidence for its operation at room temperature was not seen here, it is likely that its operation in material below the surface could also lead to a crystallographic pile-up around the indentation like that found for MnSe.

It was previously mentioned that fracture around Vickers indentations in MnSe occurred predominately on  $\{100\}$  planes. Indentations on MnS (Chao et al., 1964a) and MgO (Keh, 1960), however, showed primarily  $\{110\}$  fracture (Figure 20b). Keh (1960) attributed this to an interaction of dislocations on adjacent  $\{101\}$  planes such as, referring to Figure 52a,

$$a/2 [0\bar{1}1] + a/2 [10\bar{1}] \rightarrow a/2 [1\bar{1}0] .$$

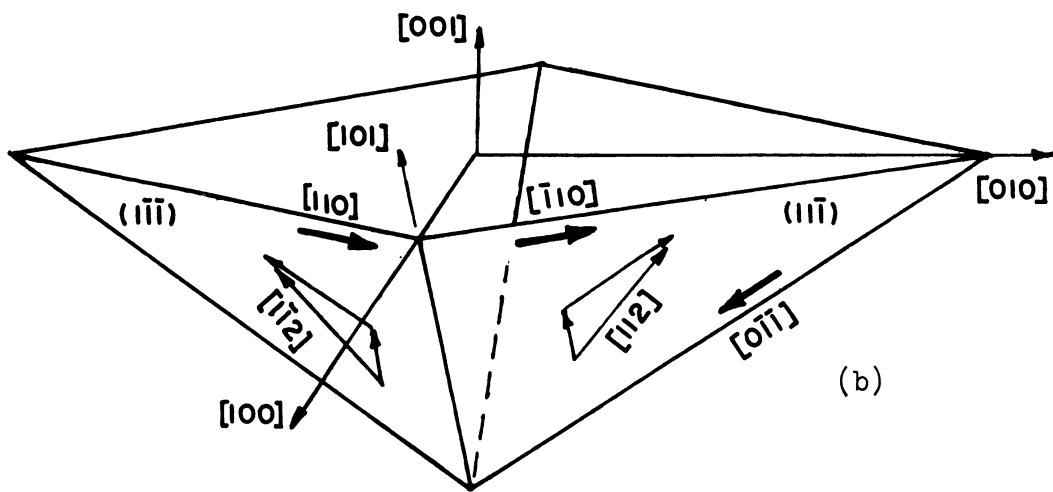
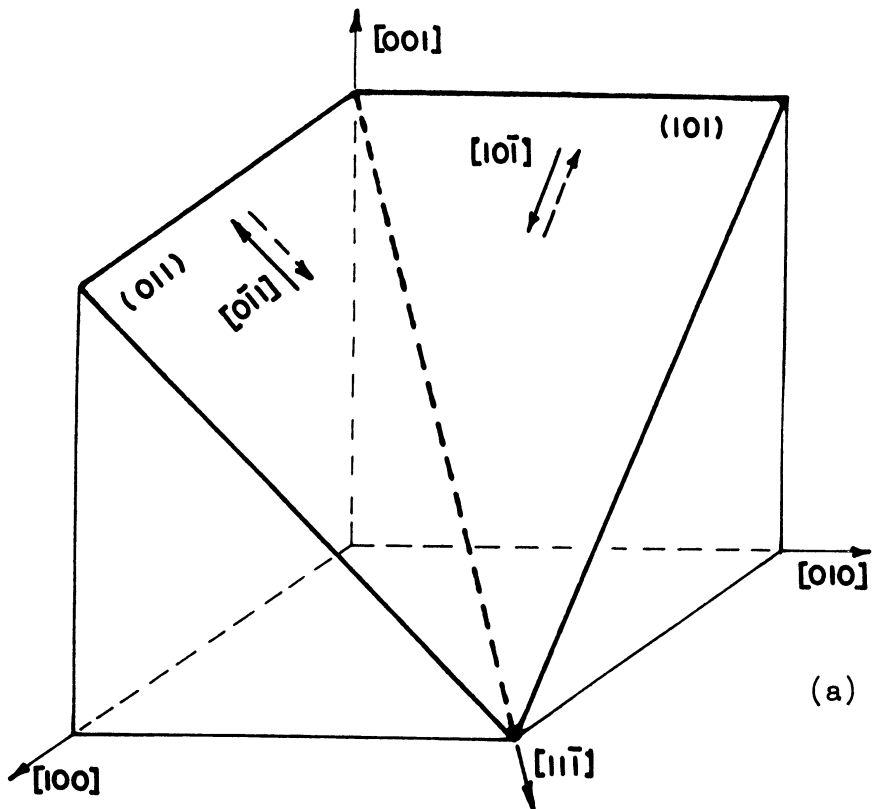


Figure 52. (a) Dislocation or slip interaction on two adjacent  $\{110\}$  planes. (b) Dislocation or slip interaction on two adjacent  $\{111\}$  planes.

The result is an immobile edge dislocation lying on a  $(112)$  plane. Therefore, the dislocations generated on the two intersecting slip planes,  $(011)$  and  $(101)$ , will pile-up against this barrier and initiate a crack in the  $(\bar{1}\bar{1}0)$  plane. If sufficient thermal energy is available, portions of the piled-up dislocations could cross glide to other parallel glide planes, reducing the tendency for crack formation and leading to a material pile-up in certain crystallographic directions as explained earlier. A somewhat simpler way of viewing this problem is to note that, in Figure 52a, upward slip on two adjacent  $\{101\}$  planes tends to separate material along a  $\{110\}_{90^\circ}$  plane.

In a similar manner, the  $\{100\}$  fracture in MnSe may be viewed as a consequence of the tendency for the material to undergo net  $\langle 112 \rangle$  flow around the indenter which, as shown in Figure 52b, separates material along a  $\{100\}_{90^\circ}$  plane.

It is also possible, however, to postulate several energetically favorable dislocation interactions forming sessile dislocations which act as barriers and lead to a dislocation pile-up and, in the absence of sufficient cross slip, to eventual fracture on  $\{100\}$ . Referring to Figure 52b, two of these are as follows:

$$(1) \quad a/2 [110] + a/2 [\bar{1}\bar{1}0] \rightarrow a/2 [020] = a[010]$$

$$(2) \quad a/2 [110] + a/2 [0\bar{1}\bar{1}] \rightarrow a/2 [10\bar{1}] .$$

Both of the resulting dislocations are of the edge variety and lie along the  $[101]$  intersection of the two  $\{111\}$  planes. The first has a glide plane  $(\bar{1}01)$  and the second  $(010)$ . Thus both would be expected to be relatively immobile.

It may be seen, therefore, from the preceding discussion that the plastic deformation leading to a material pile-up is quite intimately related in an inverse manner to fracture caused by barriers to plastic flow. Where slip and cross glide are easier (i.e., at higher temperatures or in MnSe vs. MnS) fracture is less and pile-up more pronounced.

#### B. Comparison of Deformation, Fracture, and Hardness Characteristics of Mn(Group VI) Compounds

The compounds of manganese with Group VI elements differ sufficiently with regard to deformation, fracture, and hardness characteristics that it becomes informative to review these differences and to try to relate them to some more basic characteristic of the compounds. Briefly, MnO (Moore, 1965) and MnS (Chao et al., 1964a), both NaCl-type materials, were found to have  $\{110\}\langle\bar{1}\bar{1}0\rangle$  as a primary slip mechanism but MnS also showed  $\{111\}\langle\bar{1}\bar{1}0\rangle$  as a secondary mechanism. Manganese selenide, on the other hand, revealed the primary mechanism  $\{111\}\langle\bar{1}\bar{1}0\rangle$ , that of the FCC metals, and  $\{110\}\langle\bar{1}\bar{1}0\rangle$  as secondary. Manganese telluride does not possess a NaCl-type structure, but rather, has the hexagonal NiAs structure more characteristic of selenides and tellurides of the transition metals (Taylor and Kagle, 1963).

Manganese oxide showed extensive  $\{100\}$  tension cleavage cracking around Vickers indentations in addition to  $\{110\}$  fracture produced by slip interactions on  $\{011\}$  planes. The more ductile MnS showed almost exclusively  $\{110\}$  fracture around indentations while the still softer and more ductile MnSe gave  $\{100\}$  fracture due to multiple slip interactions on  $\{111\}$  planes.

The increased ductility and softness with increased anion size point to a decrease in the ionic nature of the chemical bonding as the major factor giving rise to the more metallic behavior. Numerous other properties and characteristics of these materials are listed in Table III, and all these substantiate the idea that increasing the size of the anion decreases the strength and stability of the ionic bond, thus leading to a bond more covalent-metallic in character. In going from MnO to MnTe, the melting point and hardness decrease, the color changes from light green to opaque brown-black, the electrical resistivity and band gap energy decrease, and the anion polarizabilities increase to high values.

One can estimate the degree of ionic bonding in these compounds by electronegativity calculations as outlined by Pauling (1948). These results are shown in the last column of Table III and indicate that the amount of ionic bonding decreases from about 65% ionic in MnO to around 10% in MnTe.

Using Goldschmidt ionic radii, one can calculate theoretical lattice parameters for these compounds assuming that they are totally ionic. A comparison between calculated and measured cation-anion distances ( $r+R$ ) is shown in Table IV along with ( $r+R$ ) values assuming atomic rather than ionic radii. Once more the results indicate a departure from ionic bonding toward a more covalent or metallic structure.

Pauling (1948) says of such a situation:

"There is little evidence for a direct transition from the extreme ionic type of bond to the metallic type; in every sequence of substances which suggests itself, transition from ionic to covalent bond type first occurs followed by transition to the metallic type. This provides support for the concept of the metallic bond as similar in nature to the covalent bond, with added freedom of motion of the electrons."

TABLE III

## PROPERTIES OF Mn(GROUP VI) COMPOUNDS

Compound	Crystal Structure	Melting Point, C°	Color	Vickers Hardness, kg/mm <sup>2</sup>	Primary Deformation Mechanism	Secondary Deformation Mechanism	Anion Polarizability, cm <sup>3</sup> x 10 <sup>-24</sup>	Electrical Resistivity, ohm-cm	Band Gap, eV	Approx. % Ionic Bond <sup>9</sup>
MnO	Cubic NaCl	1780 <sup>1</sup>	Light green	285	{110}<110> slip		3.1	~10 <sup>8</sup> <sup>5</sup>		65
MnS	Cubic NaCl	1620 <sup>1</sup>	Green	142	{110}<110> slip	{111}<110> slip	10.2	~10 <sup>5</sup> <sup>6</sup>		25-30
MnSe	Cubic NaCl	1500 <sup>2</sup>	Brown	47	{111}<110> slip	{110}<110> slip		~10 <sup>5</sup> <sup>7</sup>	0.7 <sup>8</sup>	20
MnTe	Hex. NiAs	1170 <sup>3</sup>	Brown-black	64 on prism plane 107 on basal plane	{1012}twin. basal slip pencil glide in <1020>		14.0	~1 <sup>7</sup>	0.37 <sup>8</sup>	10

1. Lynch and Rudner (1966).

2. Mehta et al. (1967).

3. Johnston and Sestrich (1961).

4. Gilman (1959a).

5. DeBoer and Verwey (1937).

6. Measured at 20°C by the author.

7. Parker, R. (1958).

8. Makovetski and Sirota (1965).

9. Pauling (1948).

TABLE IV

CATION-ANION DISTANCES FOR Mn(GROUP VI) COMPOUNDS

Compound	Ionic (r+R) (Å)	Measured (r+R) (Å)	Difference (Å)	Atomic (r+R) (Å)
MnO	2.23	2.22	0.01	1.72
MnS	2.65	2.61	0.05	2.18
MnSe	2.82	2.73	0.09	2.28
MnTe	3.02	2.92	0.10	2.55

Thus it is felt that the regular variation in hardness and plastic deformation behavior is due to a change in the nature of the chemical bond which varies from an ionic-covalent bond in MnO to a largely covalent-metallic type of bond in the case of MnTe. A more metallic bond results in an increased ease of dislocation movement, a characteristic of pure metals (Gilman, 1963), and subsequent decreased hardness and increased plastic deformation before fracture.

### C. Knoop Hardness Indentations on Anisotropic Materials

#### 1. DATA AVAILABLE

It is well known that Knoop hardness tests on single crystal specimens give a periodic variation of hardness with crystallographic direction depending on the symmetry of the plane being tested. Results for numerous crystals and crystal structures appear in the literature and are generally uncorrelated in any fundamental way with the deformation behavior of the material. A sum-

mary of some of the data appearing in the literature for cubic materials is presented in Tables V and VI. The first column in the tables gives the direction of the long axis of the indenter and the second, the plane on which the test was made. Table V shows data for FCC and BCC metals and for MnSe which slips on  $\{111\}$  planes. Table VI gives hardnesses for NaCl-type materials with the glide mechanism  $\{110\}\langle\bar{1}\bar{1}0\rangle$ . These two classes of material illustrate two general types of behavior. In Table V, the hardnesses are greatest when the long axis of the indenter is in a  $\langle 100 \rangle$  direction and least when in  $\langle 110 \rangle$ , while the reverse is true for the materials in Table VI. Garfinkle and Garlick (1967) note that the hardnesses themselves, on any given material, seem to depend for the most part on the direction of the long axis of the indenter and not on the plane of indentation. It must be remembered, however, that when the long axis of the indenter is in a certain direction, one is actually measuring the hardness or resistance to deformation perpendicular to that direction since material is essentially pushed laterally normal to the long axis.

It is also interesting to note that close-packed FCC metals slipping on  $\{111\}$  planes show hardness anisotropy behavior similar to that in BCC metals. This is understandable, however, if one realizes that a common slip mechanism in BCC materials is  $\{110\}\langle\bar{1}\bar{1}\bar{1}\rangle$ , the inverse of that found in FCC metals. Both mechanisms provide the same number of slip systems, and stresses and strains are related to each other by the same  $(\cos \lambda \cos \phi)$  resolving factors. To determine if the percentage variation in hardness is the same for all the materials in Table V, it is helpful to plot on semi-log paper hardness vs. indenter orientation. This plot is shown in Figure 53, where the spacing of points on



TABLE V

KNOOP HARDNESS DATA FOR FCC AND BCC METALS AND MnSe

Orientation Direction Plane	Aluminum <sup>1</sup>	Aluminum <sup>2</sup>	MnSe	Silicon-Ferrite <sup>3</sup>	Tungsten <sup>2</sup>	Niobium <sup>2</sup>	W-3.2 Re <sup>2</sup>
[010] (001)	18	23	65	229	399	79	362
[110] (001)	13	18	43	183	342	57	279
[100] (011)	22	23	73	239	408	84	398
[0 $\bar{1}$ 1] (011)	15	17	48	203	332	60	284
[11 $\bar{1}$ ] (011)	15		54	195			
[1 $\bar{1}$ 0] (111)	17		57	199			
[11 $\bar{2}$ ] (111)	18		57	212			

1. Petty (1963).
2. Garfinkle and Garlick (1967).
3. Daniels and Dunn (1949).

TABLE VI

KNOOP HARDNESS DATA FOR NaCl-TYPE MATERIALS  
WHICH DEFORM BY  $\{110\}\langle\bar{1}\bar{1}0\rangle$  SLIP

Orientation		MnS	MnS-1% Ca <sup>1</sup>	MnO <sup>2</sup>	LiF <sup>3</sup>
Direction	Plane				
[010]	(001)	122	166	252	88
[110]	(001)	142	184	282	94
[100]	(011)	119	163	252	89
[0 $\bar{1}$ 1]	(011)	142	196	286	93
[11 $\bar{1}$ ]	(011)	142	193	284	
[1 $\bar{1}$ 0]	(111)	140		276	
[11 $\bar{2}$ ]	(111)	140		259	

1. Chao et al. (1964b).
2. Moore (1965).
3. Garfinkle and Garlick (1967).

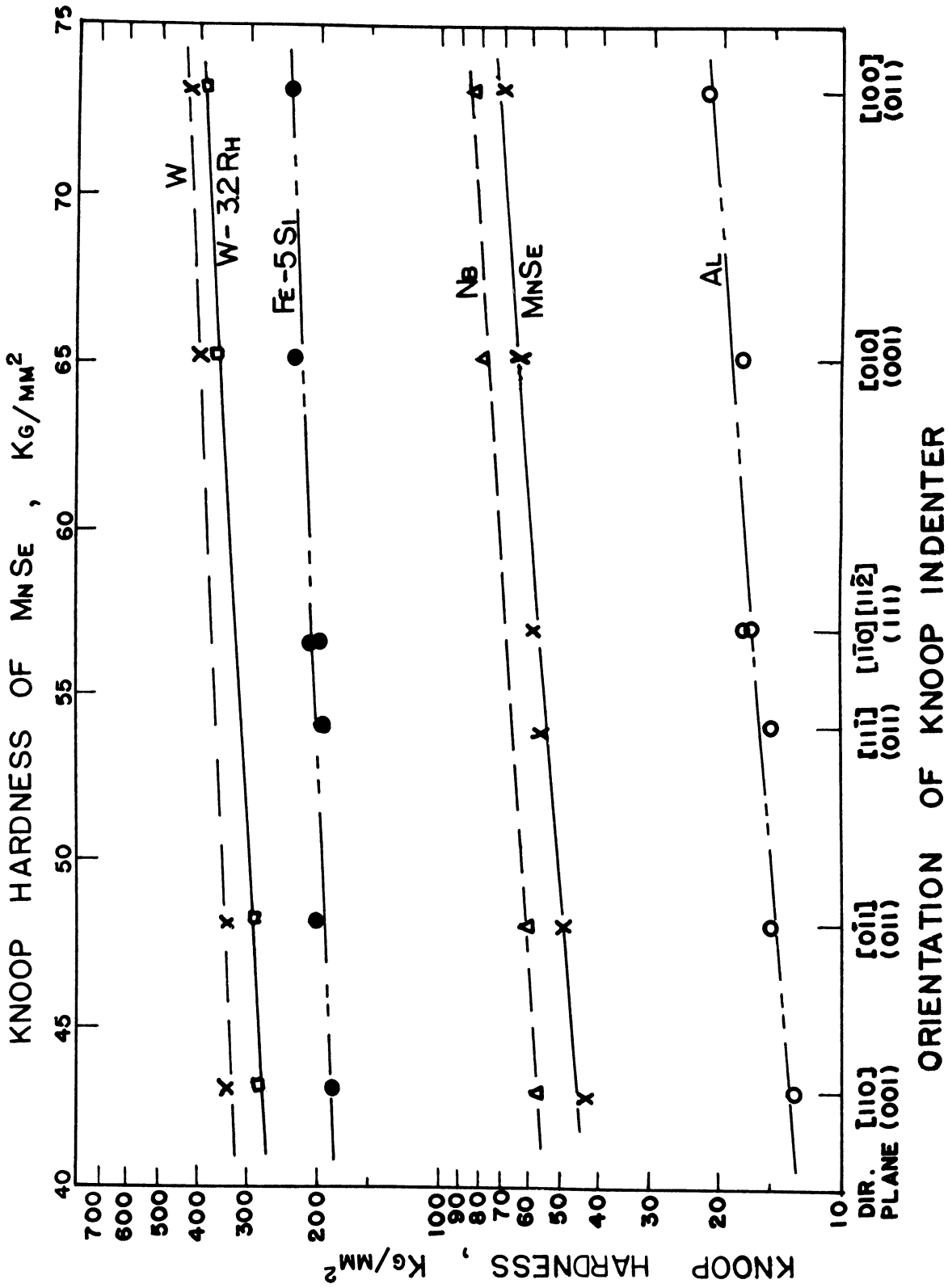


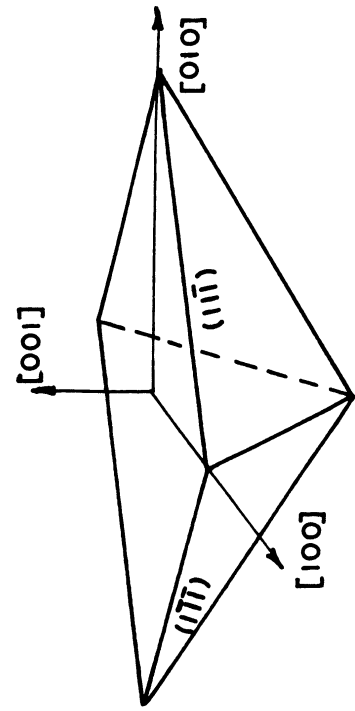
Figure 53. Comparison of Knoop hardness anisotropy behavior for several materials with cubic crystal structures.

the abscissa or "indenter orientation" scale was proportioned to the measured hardnesses on MnSe which was taken as a standard. The slopes of the various curves do not vary appreciably, indicating similar anisotropic hardness behavior in spite of crystal structure differences.

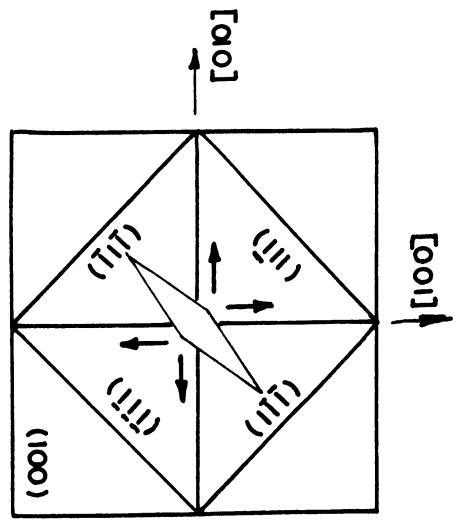
Data are also available in the literature on Knoop hardness anisotropy results for hexagonal materials although these have not been tabulated here (Daniels and Dunn, 1949; Feng and Elbaum, 1958; Schwartz et al., 1961; Partridge and Roberts, 1964).

In certain cases, one can see in qualitative terms why some indenter orientations give higher hardnesses than others for a given slip mechanism. Consider, for instance, a Knoop indentation on the (001) plane. For  $\{110\}\langle\bar{1}\bar{1}0\rangle$  glide, the slip planes are as shown in Figure 54a, which, in plan view, would appear as in Figure 54b. When the indenter is aligned with its long axis parallel to the [100] direction, relatively simple lateral displacement by slip on two  $\{110\}_{45^\circ}$  planes on each side of the indenter can occur. When aligned parallel to [110], however, the load must be relieved by complex slip utilizing several slip planes on each side of the indenter. The result is that the material is harder in  $\langle 110 \rangle$  than  $\langle 100 \rangle$  when the primary slip mechanism is  $\{110\}\langle\bar{1}\bar{1}0\rangle$ .

For materials gliding on  $\{111\}\langle\bar{1}\bar{1}0\rangle$ , the slip planes are oriented as in Figure 55b. When the indenter is parallel to [100] on the (001) plane, the load can be relieved only by slip on at least two planes on each side of the indenter. When parallel to [110], slipping in two  $\langle 110 \rangle$  directions on  $\{111\}$  planes on each side of the indenter can accommodate most of the shape change.

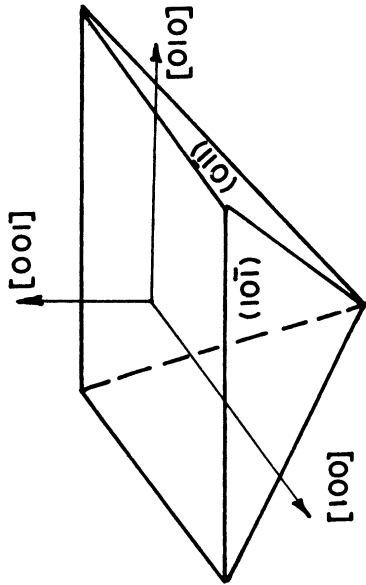


(a)

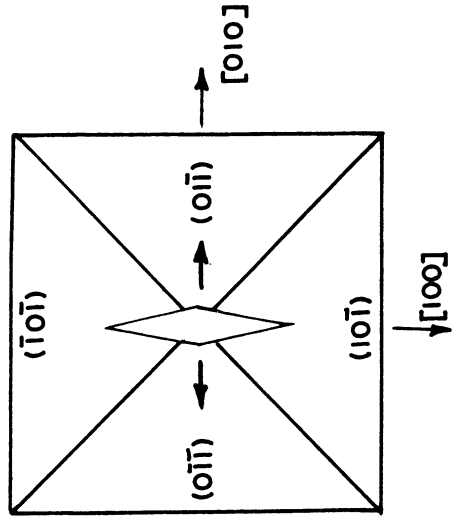


(b)

Figure 55. (a) Orientation of {111} planes. (b) View in  $[00\bar{1}]$  direction with Knoop indenter in  $[\bar{1}10]$ .



(a)



(b)

Figure 54. (a) Orientation of {110} planes. (b) View in  $[00\bar{1}]$  direction with Knoop indenter in  $[100]$ .

This multiple glide on two planes might be expected to occur more easily than slip on four planes and would lead one to predict that  $\langle 110 \rangle$  directions on  $(001)$  are softer than  $\langle 100 \rangle$  for  $\{111\}\langle \bar{1}\bar{1}0 \rangle$  glide.

The situation becomes more complex for indentations on  $\{011\}$  planes, but the hardness anisotropy can still be quite easily rationalized for materials showing  $\{111\}\langle \bar{1}\bar{1}0 \rangle$  slip. The  $\{111\}$  glide planes are shown in Figure 56a. Two of these will intersect a  $(\bar{1}\bar{1}0)$  plane at 35.3 degrees in the  $[110]$  direction and the two others at 90 degrees in  $[112]$  and  $[\bar{1}\bar{1}2]$  directions. An edge view of the  $(\bar{1}\bar{1}0)$  plane is shown in Figure 56b with the  $(\bar{1}\bar{1}1)$  and  $(\bar{1}\bar{1}\bar{1})$  planes intersecting in the  $[110]$  direction. Thus, when the indenter is aligned parallel to  $[110]$ , most of the lateral displacement can be accomplished by relatively simple slip on each side of the indenter on these two planes. When parallel to  $[100]$ , however, the  $\{111\}_{90^\circ}$  planes must now play a more prominent role, and one would therefore expect the material to be softer when the long axis is in a  $\langle 110 \rangle$  direction.

It becomes much more difficult to visualize this for  $\{011\}$  indentations on materials showing primarily  $\{110\}\langle \bar{1}\bar{1}0 \rangle$  glide.

## 2. SCOPE OF THE PROBLEM

An accurate quantitative analysis of the deformation associated with the Knoop indenter, however, represents a problem of tremendous complexity. A necessary first step is to define the state of stress underneath the indenter. Because of the shape of the indenter, the stress state is not uniform but depends on position in the material relative to the indenter. In addition,

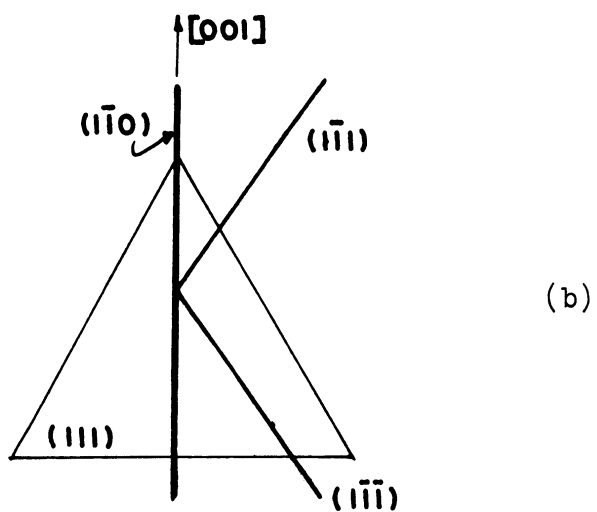
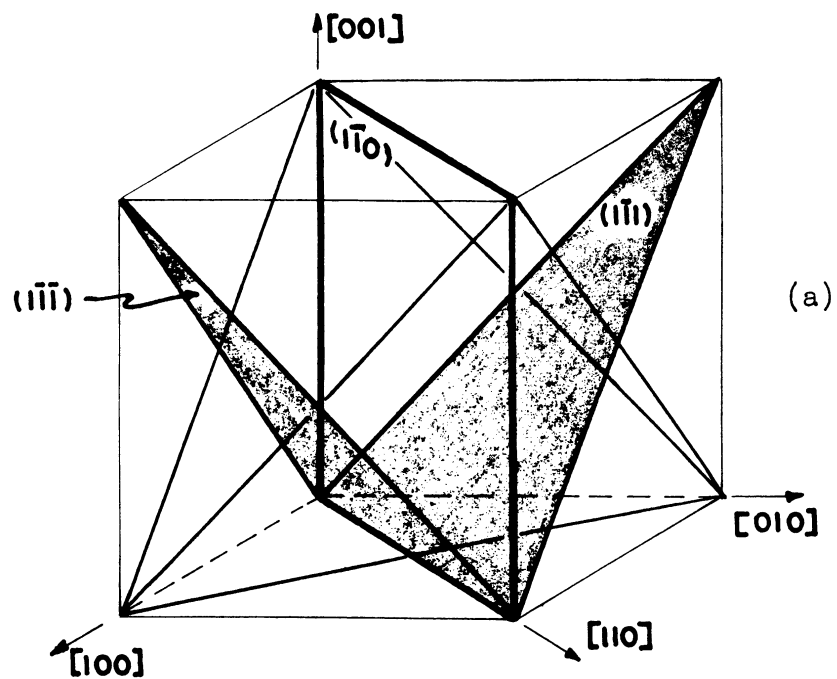


Figure 56. (a) Orientation of  $\{111\}$  planes with respect to the  $(1\bar{1}0)$  plane. (b) Edge view of the  $(1\bar{1}0)$  plane with intersecting  $\{111\}$  planes. The shaded planes in (a) are shown as lines in (b).

anisotropy inherent in the single crystal means that strains and yield stresses vary in another complex manner.

In order to solve this problem rigorously for a given indenter orientation, it would be necessary to determine all physically possible flow paths on the known slip systems capable of accommodating the shape change caused by the indenter, to calculate the work of deformation on each, and to pick the particular flow path which requires the expenditure of the least amount of work as the one most likely to describe the actual indentation process. If this were done for all orientations of the indenter, the "minium work" values at each orientation should give the relative hardnesses.

An additional complication arises when the known slip mechanism cannot provide the five independent slip systems necessary to produce an arbitrary shape change with conservation of volume. The  $\{110\}\langle\bar{1}\bar{1}0\rangle$  mechanism of NaCl-type ionics, for instance, gives only two (Groves and Kelly, 1963); consequently, for these materials, it is necessary to know what other mechanisms operate in order to solve this problem accurately. Also, work hardening, indenter end effects, and possible material rotations add further complications.

### 3. TREATMENTS OF PROBLEM

Apparently Daniels and Dunn (1949) are the only persons who have attempted a comprehensive treatment of the hardness anisotropy of single crystals. Referring to Figure 57A, they assume that the force causing deformation around each facet is a tensile force,  $F$ , parallel to the steepest slope of the facet. This assumption has been the subject of some criticism (Mebis, 1949). They



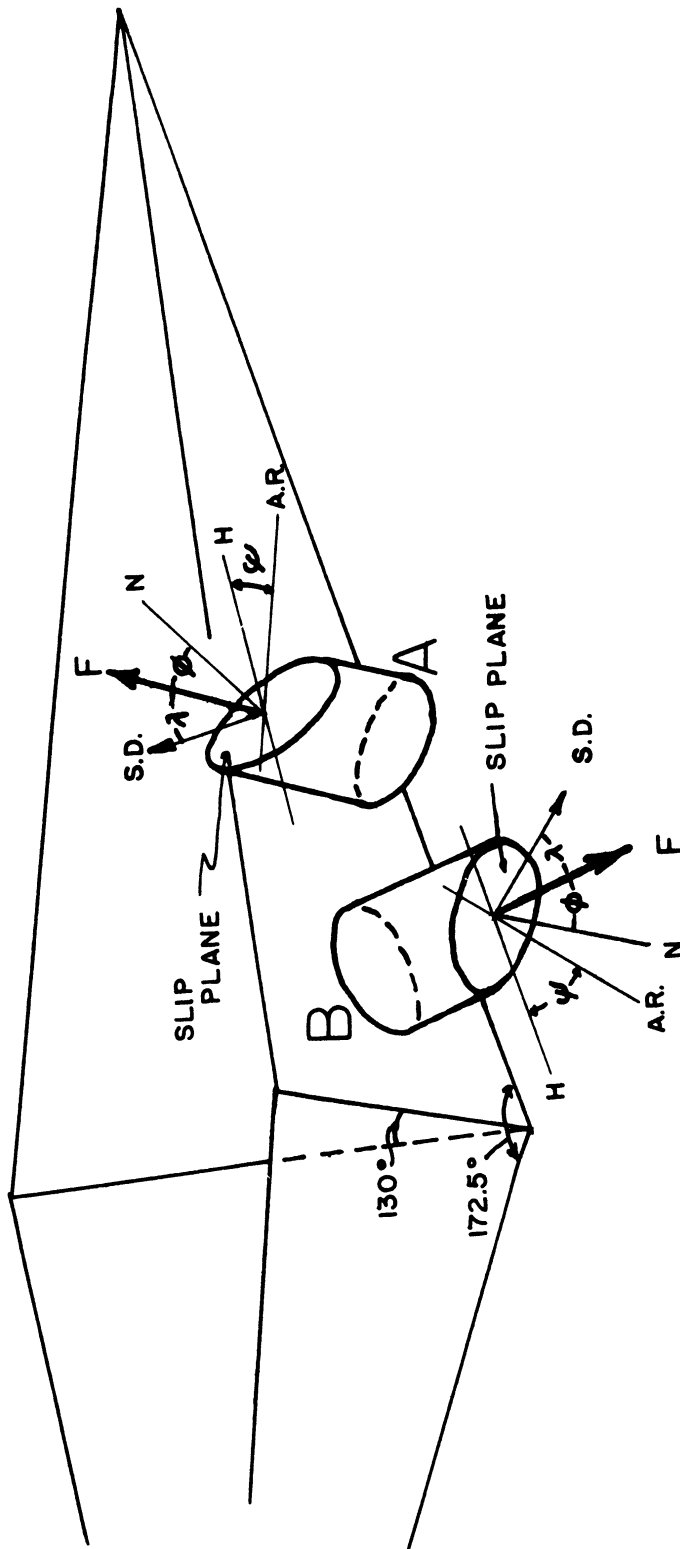


Figure 57. Diagram of Knoop indenter showing positions of force, slip plane, slip direction, and axes of rotation for (A) Daniels and Dunn (1949) and (B) Feng and Elbaum (1958) methods of analysis.

resolve this force for each facet on each of the slip planes and slip directions of the known or assumed glide mechanism using the relation:

Effective Resolved Shear = ERS =  $F/A (\cos \lambda \cos \phi \cos \psi)$ , where

- $\lambda$  = the angle between the slip direction, S.D., and the effective force
- $\phi$  = the angle between the normal to the slip plane, N, and the effective force
- $\psi$  = the angle between the direction, A.R., in the slip plane perpendicular to the slip direction, and the direction, H, in the "indenter-facet" plane perpendicular to the effective force.

The factor,  $\cos \psi$ , is supposed to evaluate the constraint imposed by the indenter as material tries to rotate about axis A.R. but indenter constraints try to force it to rotate about axis H. The larger the angle between these axes, the more difficult the deformation becomes. The particular slip system with the largest resolving factor ( $m = \cos \lambda \cos \phi \cos \psi$ ) is the one assumed to be activated first. Because of the geometrical similarity of the indenter, this "m"-factor will remain essentially the same throughout the test and it is assumed to be the one primarily responsible for determining the hardness. High "m" means low hardness so the hardness becomes proportional to  $(1/m)$ .

Computations based on their model apparently predicted the hardness anisotropy found in silicon ferrite. Recently, however, Garfinkle and Garlick (1967), in re-examining this model, found that Daniels and Dunn (1949) had failed to consider certain slip systems of their assumed  $\{112\}\langle 11\bar{1} \rangle$  glide mechanism. When these were included, little agreement was found between calculated and measured results. Similar attempts involving  $\{110\}\langle 1\bar{1}1 \rangle$  and  $\{123\}\langle 11\bar{1} \rangle$  slip revealed equally poor correlations, indicating a discrepancy in their theoretical treatment.

Feng and Elbaum (1958), in modifying the Daniels and Dunn treatment, assumed that the effective force causing deformation was a compressive force acting perpendicular to each indenter facet (Figure 57B). Garfinkle and Garlick (1967) again found little agreement between predicted hardness anisotropy and the experimental results using this technique.

It was our desire to view this problem in terms of shear stresses rather than normal stresses since it is the differences in principal normal stresses which determine the shear stresses responsible for deformation (i.e., hydrostatic stresses cause no deformation). The slip line field analysis technique was selected as a logical approach to the problem. Previously Hill et al. (1947) calculated the locus of maximum shear stress for the plane strain indentation of an isotropic material by an infinite wedge. Figure 58 shows this field on both sides of an infinite wedge of included angle 130 degrees, the same as that of the Knoop indenter. This field was assumed to approximate the stress state around the indenter for the first attempt at characterizing the deformation.

In triangle OAE, the principal shearing stresses are in the directions EA and OA. The principal normal stresses, always at 45 degrees to the shears, are P and Q, and, by coincidence,  $P = 2Q$  for this special case. In the fan shaped region OAB, the directions of maximum shear rotate through an angle of 57.2 degrees, while in triangle OBC, the principal directions are OB and BC. The field is symmetrical about the center of the indenter.

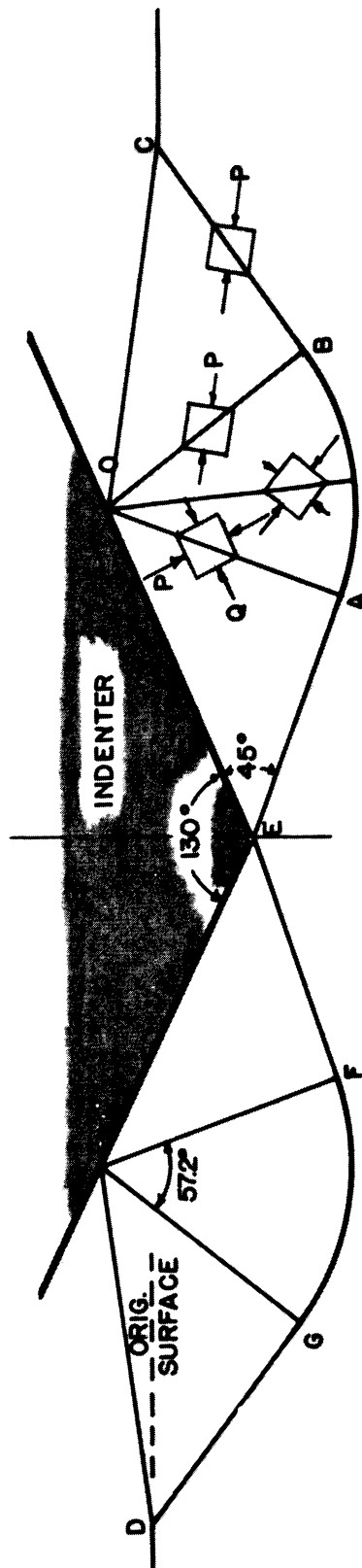


Figure 58. Slip line field associated with the plane strain indentation of an isotropic material by an infinite wedge of included angle  $130^\circ$ . Principal normal stresses are P and Q (Hill et al., 1947).

## a. One Lateral Shear

In the first technique, a net shearing stress was assumed to act on each side of the indenter in directions EC and ED and to be the stress primarily responsible for the deformation associated with the indenter. These particular directions were chosen because they seemed to be consistent with a continuity of material flow and to represent a satisfactory combination of the downward shear stresses in directions EA and EF and the upward stresses in directions BC and GD. This shear stress was resolved on all twelve slip systems of the type  $\{111\}\langle\bar{1}\bar{1}0\rangle$  and all six systems of the type  $\{110\}\langle\bar{1}\bar{1}0\rangle$  for each orientation of the indenter. This was accomplished by use of a stereographic projection such as that shown in Figure 59 for a Knoop indentation in the  $[010]$  direction on the  $(001)$  plane. The axes "y" and "x" are parallel and perpendicular, respectively, to the shear stress on one side of the indenter. The stress was resolved using the standard formula:

$$\begin{aligned}\tau_{ND} &= \tau_{xy}(l_{xD}l_{yN} + l_{xN}l_{yD}) \\ &= \tau_{xy}(m)\end{aligned}$$

$\tau_{ND}$  = resolved shear stress

$l_{xD}$  = cosine of the angle between the "x"-axis and the slip direction

$l_{yN}$  = cosine of the angle between the "y"-axis and the normal to the slip plane, etc.

The particular slip system with the maximum value of "m" was assumed to be the first to operate and the one contributing most to the total deformation. The hardness was thus assumed to be proportional to  $(1/m)$  and the hard-



ness anisotropy could be estimated by comparing the minimum  $(1/m)$ 's for various indenter orientations.

b. Two Shear Stresses

In a second method of analysis, it was assumed that two shearing stresses on each facet, one downward and the other in an upward direction, were primarily responsible for the plastic flow. Each facet was taken to be one side of an infinite wedge with a corresponding slip line field associated with it. The two directions of shear were assumed to be EA and BC (Figure 58) which are the directions of principal shear stress in the triangular regions OEA and OBC of the slip line field, respectively. This is shown in stereographic projection for facet 1 in Figure 60. Lines PQ and RS are along the radii of the great circles which designate the intersection of the facets with the plane of projection. It is out these directions that the stresses are assumed to act. They are shown for facet 1 along the directions  $y_1$  for the downward shear stress (EA) and  $y_2$  for the upward stress (BC). The directions  $x_1$  and  $x_2$  are normal to  $y_1$  and  $y_2$  respectively. Each of the shear stresses on each facet was then resolved on each of the twelve  $\{111\}\langle\bar{1}\bar{1}0\rangle$  systems and six  $\{110\}\langle\bar{1}\bar{1}0\rangle$  systems (for orientations showing 4-fold symmetry around the indenter, it was necessary to evaluate the "m" factors for only one facet, etc...). The minimum  $(1/m)$  values for each shear at each orientation were combined as  $\frac{1}{2} (1/m_{EA} + 1/m_{BC})$  which was then taken as proportional to the hardness. This particular mode of combination was chosen because of the interdependence of both steps in the shearing process. For instance, if all the m's for one shear were zero, the

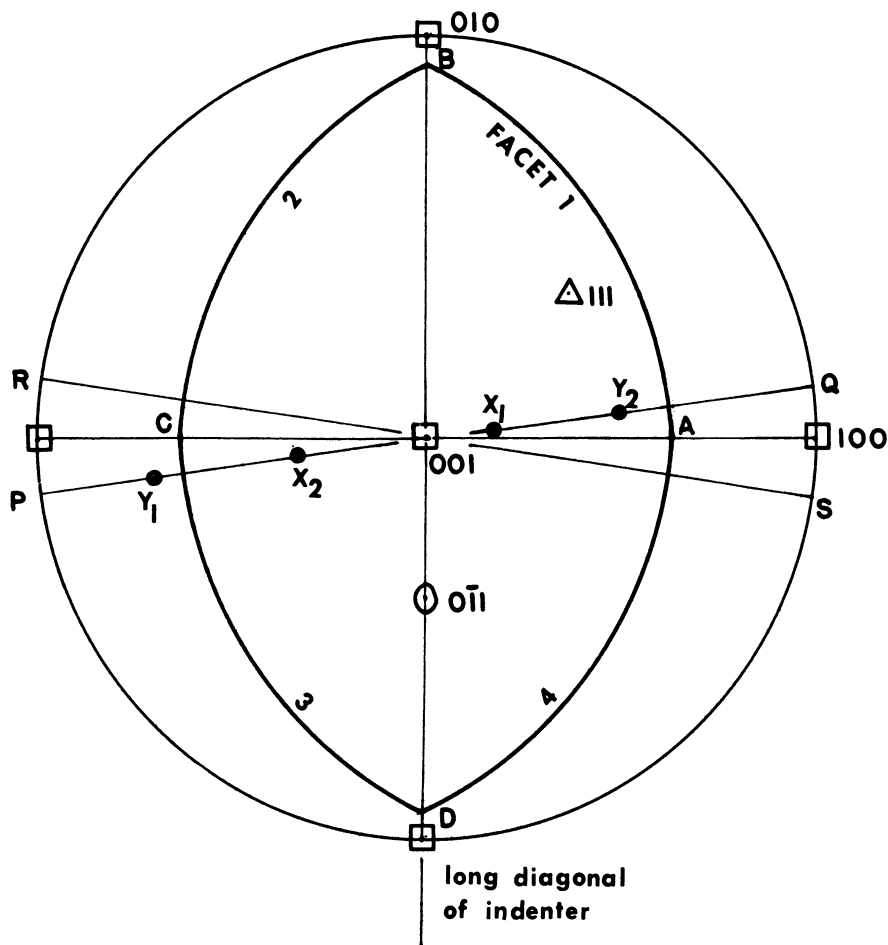


Figure 60. Standard (001) stereographic projection of a cubic crystal showing the assumed shear stress directions for facet 1 and the intersection of the Knoop indenter with the plane of projection for the "two shears" method of analysis when the long indenter axis is in the [010] direction.

two step deformation could not occur and the hardness would be infinite. This would still be reflected in the term  $\frac{1}{2}(1/m_{EA} + 1/m_{BC})$ .

### c. Integrated Average of Resolved Shear

It can be shown for the indentation of an infinite wedge on an isotropic material that about half the work of deformation takes place in the fan-shaped region OAB (Figure 58), which was completely neglected in the previous treatment. It was felt that a better analytical description of the deformation



would be obtained if an average ( $1/m$ ) value could be computed for this center region of the slip line field and weighted with the values from the "two shears" method. Accordingly, the minimum ( $1/m$ ) values were found at 10 degree intervals as the directions of maximum shear rotated from EA to BC and these were plotted vs. the degrees of rotation,  $\theta$ . An integrated average value was obtained and weighted with the end-point values to give one net resolving factor of:

$$\text{NRF} = \frac{1}{4} \left( \frac{1}{m_{\text{EA}}} \right)_{\text{min}} + \frac{1}{2} \left[ \frac{\int_{\theta_{\text{EA}}}^{\theta_{\text{BC}}} \left( \frac{1}{m} \right)_{\text{min}} d\theta}{\theta_{\text{BC}} - \theta_{\text{EA}}} \right] + \frac{1}{4} \left( \frac{1}{m_{\text{BC}}} \right)_{\text{min}} .$$

The minimum ( $1/m$ )'s varied in value and the particular slip system on which they occurred usually changed several times during the 57.2 degree rotation. The total factor given in the above equation was taken as proportional to the hardness.

#### 4. RESULTS

The resultant hardness factors for the above three procedures together with similar calculations by the Daniels and Dunn and Feng and Elbaum methods are shown in Tables VII and VIII. Table VII is for  $\{111\}\langle\bar{1}\bar{1}0\rangle$  slip with the hardnesses of MnSe added for reference. Table VIII shows results for  $\{110\}\langle\bar{1}\bar{1}0\rangle$  slip and includes the measured hardnesses of MnS and MnO for comparison. Relative hardnesses calculated by the "two shears" method of analysis matched most closely the measured values for materials listed in Table V (i.e., FCC and BCC metals and MnSe). Figure 61 shows a graphical correlation for three

TABLE VII

KNOOP HARDNESS CALCULATIONS FOR  $\{111\}\langle 1\bar{1}0\rangle$  SLIP

Orientation Direction	Plane	Hardness, MnSe	Daniels and Dunn	Feng and Elbaum	Lateral Shear	Two Shears	Integrated Average
[010]	(001)	65	3.62	4.26	1.91	1.40	1.540
[110]	(001)	43	2.84	3.24	1.85	1.23	1.36
[100]	(011)	73	3.25	3.25	1.28	1.65	1.49
[0 $\bar{1}$ 1]	(011)	48	2.61	2.96	1.80	1.17	1.26
[11 $\bar{1}$ ]	(011)	54	2.47	3.31	1.115	1.116	1.12
[1 $\bar{1}$ 0]	(111)	57	2.70	2.81	1.21	1.34	1.27
[11 $\bar{2}$ ]	(111)	57	2.52	2.60	1.05	1.247	1.19

TABLE VIII

KNOOP HARDNESS CALCULATIONS FOR  $\{110\}\langle\bar{1}\bar{1}0\rangle$  SLIP

Orientation Direction	Plane	Hardness MnS	Hardness MnO	Daniels and Dunn	Feng and Elbaum	Lateral Shear	Two Shears	Integrated Average
[010]	(001)	122	252	3.50	3.37	3.08	1.31	$\infty$
[110]	(001)	142	282	7.46	3.79	3.94	1.59	$\infty$
[100]	(011)	119	252	2.67	2.59	1.05	2.49	1.91
[0 $\bar{1}$ 1]	(011)	142	286	3.77	11.1	4.37	1.65	2.44
[1 $\bar{1}$ 1]	(011)	142	284	5.24	6.29	1.80	1.84	1.84
[1 $\bar{1}$ 0]	(111)	140	276	4.59	4.50	1.34	3.85	2.97
[11 $\bar{2}$ ]	(111)	140	259	3.98	3.85	1.28	2.32	1.98

of these materials—aluminum, manganese selenide, and silicon iron. The abscissa is the measured Knoop hardness normalized to the maximum value, which occurred at the same indenter orientation in all three materials—[100] on (011). The ordinate is the calculated hardness,  $(1/m)_{\text{equivalent}}$ , normalized by the calculated value at the indenter orientation giving the highest measured value—[100] on (011). If the theory is correct, all the points should fall on a curve of slope equal to unity. While there is considerable scatter, the trend does seem to be along lines with this slope, although the softest orientation, [110] on (001), falls way out of line.

It was thought that the "integrated average" method would provide a better correlation, but a plot similar to Figure 61 shown in Figure 62 indicates much greater scatter than in the "two shears" approach.

A comparison between calculated and measured hardness in MnSe for all five calculational methods is shown in Figure 63. Here again, the hardness of MnSe is normalized by the highest value measured, and the calculated hardness by the calculated value at the same indenter orientation. It is clear that the "two shears" technique provides the best correlation (open circles).

Similar plots for materials exhibiting  $\{110\}\langle\bar{1}\bar{1}0\rangle$  glide show almost no correlation between measured and calculated hardnesses. This is not extremely surprising, however, since the  $\{110\}\langle\bar{1}\bar{1}0\rangle$  mechanism alone cannot provide the five independent slip systems necessary to accommodate an arbitrary shape change, while  $\{111\}\langle\bar{1}\bar{1}0\rangle$  slip can. If the results are not good in the latter case, they can hardly be expected to improve when other slip systems of unknown character must come into play.

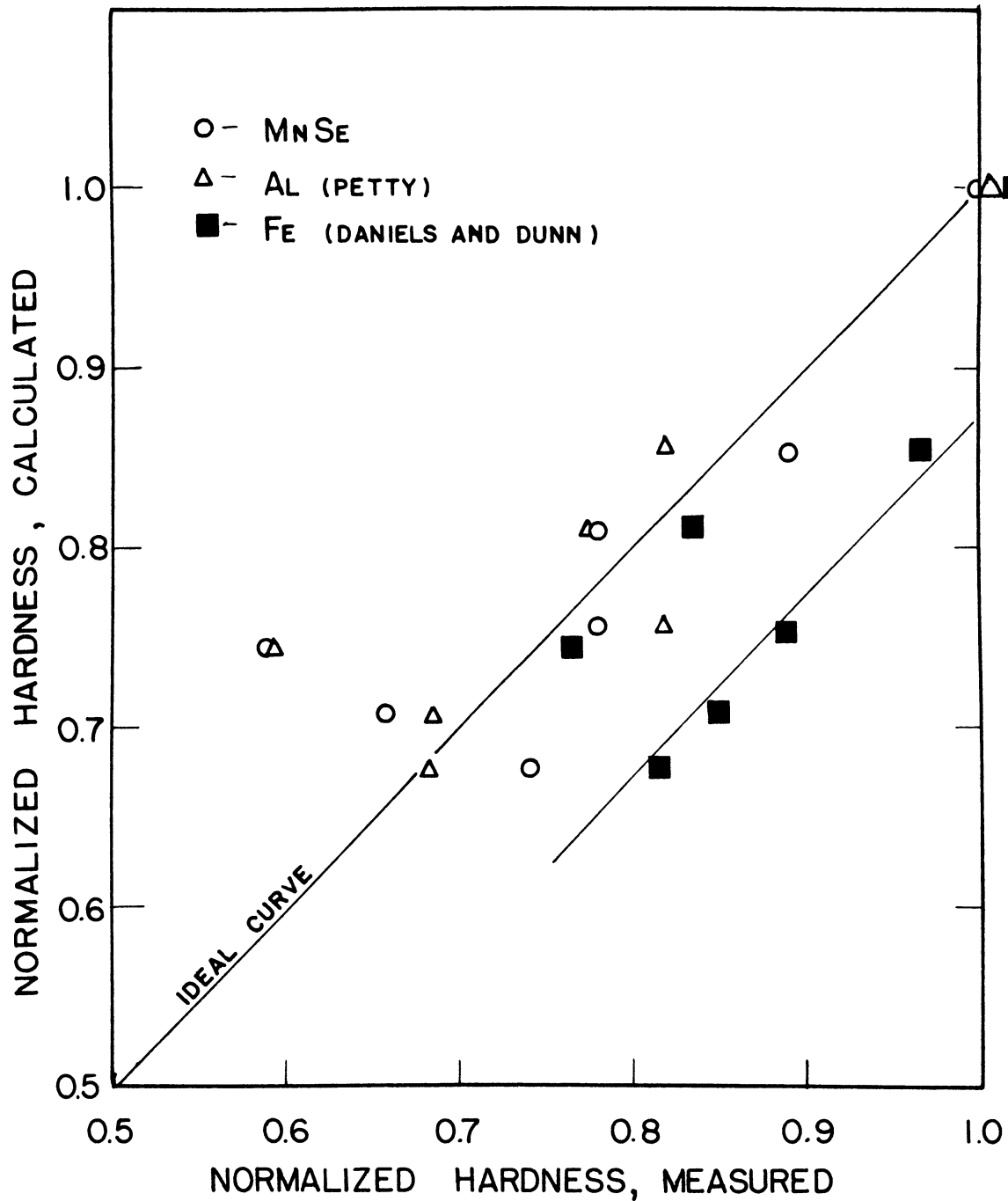


Figure 61. Comparison of calculated and measured Knoop hardnesses on single crystals of manganese selenide, aluminum, and silicon ferrite using the "two shears" method of analysis.

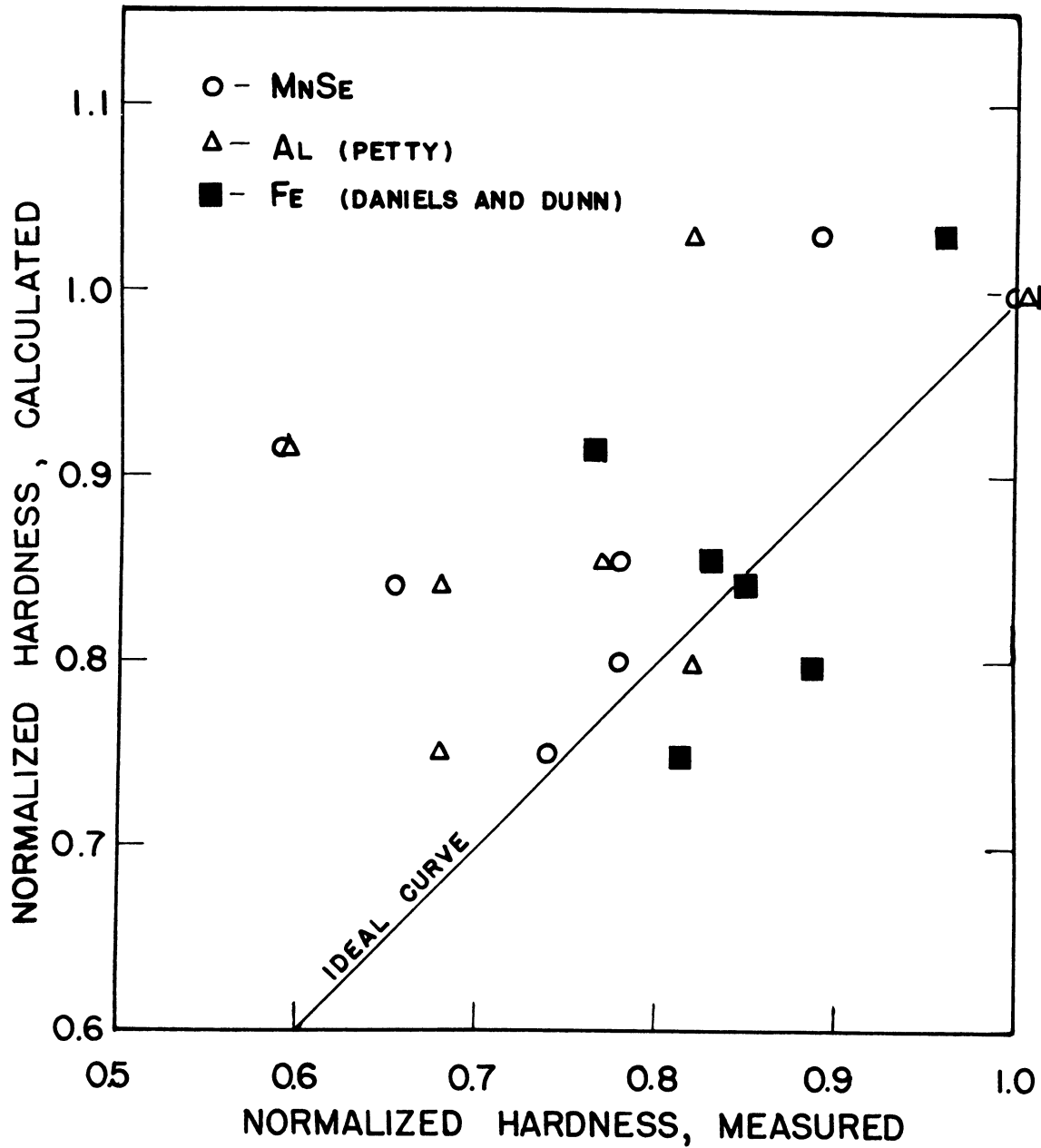


Figure 62. Comparison of calculated and measured Knoop hardnesses on single crystals of manganese selenide, aluminum, and silicon ferrite using the "integrated average" method of analysis.

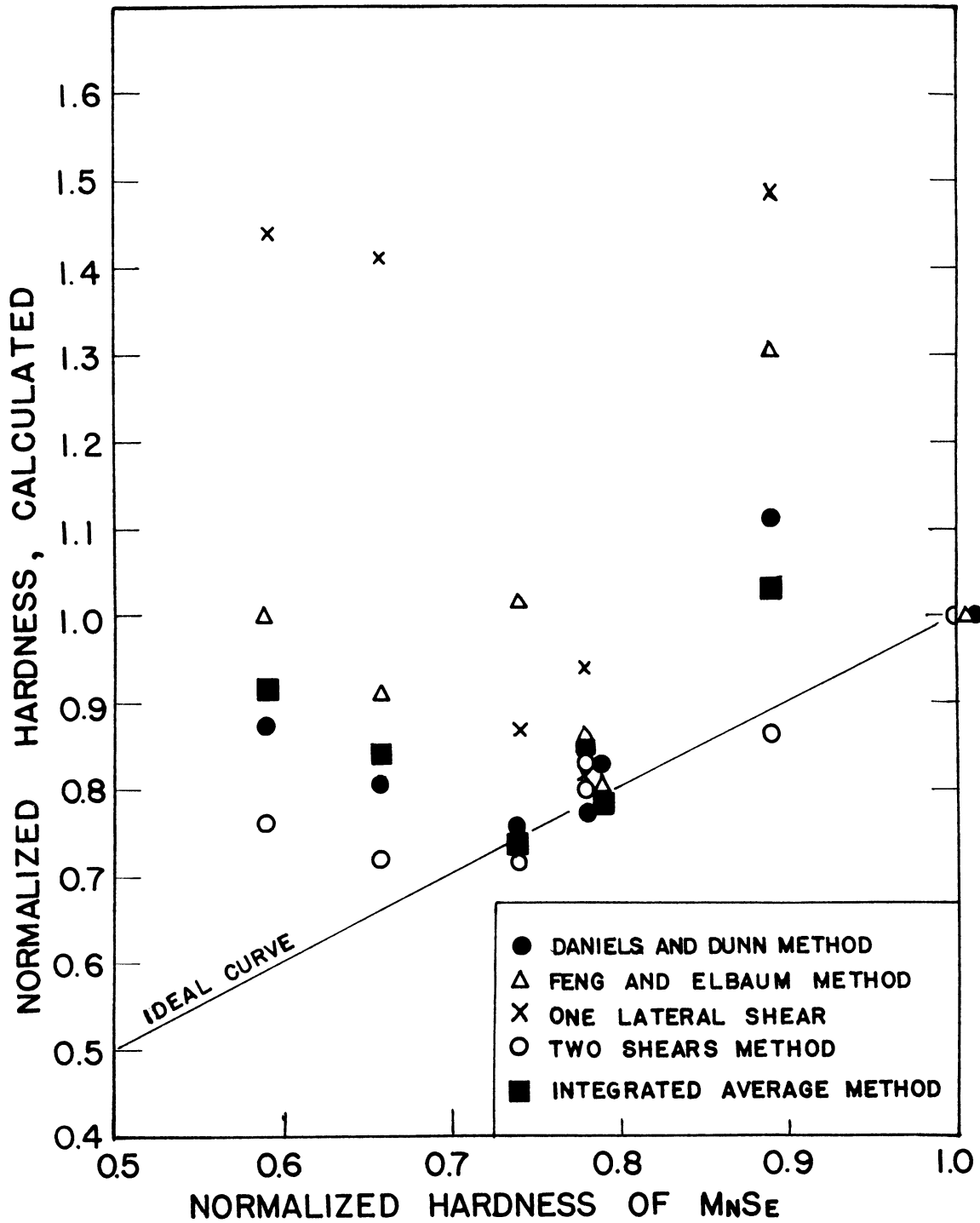


Figure 63. Comparison of various methods of estimating Knoop hardness anisotropy on cubic single crystals using manganese selenide as standard.

In summary, several approaches were attempted in an effort to explain in more fundamental and quantitative terms the deformation and hardness anisotropy associated with Knoop indentations on single crystals. Good results were not obtained although the best correlation was found for materials slipping on  $\{111\}\langle\bar{1}\bar{1}0\rangle$  when it was assumed that two shear stresses, one downward and the other upward, were responsible for initiating a majority of the plastic deformation. The problem is so complex, however, that it is now felt only an extremely complex theory will ever be able to explain the deformation associated with the Knoop indentation on single crystals.



## CHAPTER VI

### CONCLUSIONS

The following conclusions may be drawn from this investigation:

1. Cubic, NaCl-type manganous selenide, MnSe, exhibits  $\{111\}\langle\bar{1}\bar{1}0\rangle$  and  $\{110\}\langle\bar{1}\bar{1}0\rangle$  as primary and secondary slip mechanisms respectively. This is in contrast to the  $\{110\}\langle\bar{1}\bar{1}0\rangle$  mechanism preferred by MnO and MnS.
2. As with MnO and MnS, the primary cleavage plane in MnSe is  $\{100\}$  with some secondary  $\{110\}$  cleavage also evident. Around surface indentations, however, MnSe shows primarily  $\{100\}$  fracture due to dislocation interactions on  $\{111\}$  planes, in contrast to  $\{110\}$  fracture common in MnS due to dislocation interactions on  $\{110\}$  planes.
3. Around Vickers indentations on MnSe and MnS, a crystallographic pile-up of material occurs in certain regions and a sinking-in of material in others. The pile-up directions are independent of indenter orientation and unusual shaped impressions result depending on how the indenter penetrates these piled-up regions. This phenomenon is related to the flow of material on crystallographic slip systems.
  - a. For an indentation on the  $(001)$  plane of MnSe, for instance, material prefers to flow in two  $\langle 110 \rangle$  directions on each  $\{111\}$  slip plane giving an apparent Burgers vector in  $\langle 112 \rangle$  and resulting in four piled-up hills out  $\langle 110 \rangle$  directions on  $(001)$ .
  - b. The pile-up in MnS is like that found in MnSe. In this case, however, the apparent  $\langle 112 \rangle$  flow may be due to cross slip and disloca-

tion climb on adjacent  $\{110\}$  planes in addition to secondary slip on  $\{111\}$  planes.

- c. The preferred flow paths resulting in pile-up also result in the appearance of a majority of the slip traces being concentrated in the piled-up regions.
- d. For both MnSe and MnS, dislocation interactions forming barriers can lead to dislocation pile-up and eventual fracture. Where cross slip and climb can occur, material pile-up occurs and the tendency for fracturing near indentations decreases.

4. In the continuous solid solution system MnSe-MnS, the primary slip mechanism changes gradually from  $\{111\}\langle\bar{1}\bar{1}0\rangle$  for MnSe to  $\{110\}\langle\bar{1}\bar{1}0\rangle$  for MnS.

5. Substitution of sulfide for selenide ions in MnSe results in a large positive solid solution hardening deviation. Substitution of selenide for sulfide ions in MnS also results in a positive, although smaller, solid solution hardening effect.

- a. MnSe is much softer than MnS ( $47 \text{ kg/mm}^2$  vs.  $145 \text{ kg/mm}^2$ ).
- b. Within the limits of experimental error, the diamond pyramid hardness is the same on the  $\{001\}$ ,  $\{011\}$ , and  $\{111\}$  planes for all compositions in the MnSe-MnS system.
- c. The  $\{110\}\langle\bar{1}\bar{1}0\rangle$  slip mechanism of MnS hardens much more rapidly with decreasing temperature than the  $\{111\}\langle\bar{1}\bar{1}0\rangle$  mechanism characteristic of MnSe such that, at liquid nitrogen temperature, MnS shows an appreciable amount of  $\{111\}$  slip.

6. The addition of telluride ions to MnSe results in an early appearance of  $\{110\}$  slip and produces a slightly higher rate of solid solution hardening than for a comparable substitution of sulfide ions.

7. Manganous telluride, MnTe, having the hexagonal NiAs structure, shows three modes of plastic deformation around Vickers and Knoop indentations: (1)  $\{10\bar{1}2\}$  twinning, (2) basal glide, and (3) pencil glide in  $\langle 11\bar{2}0 \rangle$ .

8. Fracture in MnTe occurs on  $\{0001\}$  primarily but also on  $\{10\bar{1}0\}$ , both in crushed fragments and around surface indentations.

9. Solid solutions formed by substitution of selenide ions in the MnTe matrix show the same plastic deformation and fracture characteristics as MnTe.

a. The basal plane is much harder than the prism planes which is a reflection of the difficulty of activating slip systems by basal indentation.

b. The rate of hardening is greater than for the comparable substitution of selenide ions in the MnS matrix.

10. Knoop hardness anisotropy behavior is evident on the single crystal specimens studied.

a. Manganese selenide is softest when the long axis of the Knoop indenter is in a  $\langle 110 \rangle$  direction and hardest when it is in  $\langle 100 \rangle$ . The reverse is true for MnS.

b. The reversal of hard and soft directions in the MnSe-MnS system provides a qualitative means of following the gradual change of primary glide mechanism with composition.

11. A rigorous treatment of Knoop hardness anisotropy and the flow of material associated with the indenter is an extremely complex problem which cannot be explained in a manner as simple as that proposed by Daniels and Dunn.

- a. Of several additional procedures tried in an effort to explain this behavior, the method giving the best correlation between theory and measured results for FCC metals is one which assumes that the majority of plastic flow is caused by two shear stresses around each facet of the indenter, one acting in a downward direction, the other, upward. The correlation was much better than the Daniels and Dunn procedure but still was not considered good.
- b. The same approaches on NaCl-type ionic materials gliding primarily on  $\{110\}\langle\bar{1}\bar{1}0\rangle$  showed poor correlations for all methods attempted because five independent slip systems are not available from this slip mechanism alone.

12. The changes in deformation, fracture, and hardness characteristics in compounds of manganese with Group VI elements are relatable to changes in other properties such as electrical conductivity and melting point and result from a regular decrease in the ionic character associated with the chemical bonding as one goes from MnO to MnTe.

APPENDIX I

TABULATION OF HARDNESS DATA

Part I. Knoop Hardness Numbers- 200 gram load  
(Compositions are atom percents)

MnSe + 25°C

Plane	Long Axis Direction			
	<010>	<011>	<111>	<112>
{001}	64.9	43.		
{011}	73.	48.	54.	54.
{111}		57.		57.

91MnSe-9MnS 25°C

Plane	Long Axis Direction			
	<010>	<011>	<111>	<112>
{001}	91.	73.		
{011}	94.	82.	87.	84.
{111}		90.		93.

75MnSe-25MnS 25°C

Plane	Long Axis Direction			
	<010>	<011>	<111>	<112>
{001}	114.	96.		
{011}	114.	112.	110.	109.
{111}		116.		116.

50MnSe-50MnS 25°C

Plane	Long Axis Direction			
	<010>	<011>	<111>	<112>
{001}	149.	138.		
{011}	148	146.	149	147.
{111}		147.		141.

25MnSe-75MnS 25°C

Plane	Long Axis Direction			
	<010>	<011>	<111>	<112>
{001}	157.	160.		
{011}	161.	176.	170.	172.
{111}		171.		171.

MnS 25°C

Plane	Long Axis Direction			
	<010>	<011>	<111>	<112>
{001}	122.	142.		
{011}	119.	142.	142.	140.
{111}		140.		140.

MnSe -70°C

Plane	Long Axis Direction			
	<010>	<011>	<111>	<112>
{001}	72.	48.		

75MnSe-25MnS -70°C

Plane	Long Axis Direction			
	<010>	<011>	<111>	<112>
{001}	127.	109.		

50MnSe-50MnS -70 °C

Plane	Long Axis Direction			
	<010>	<011>	<111>	<112>
{001}	165.	155.		

25MnSe-75MnS. -70 °C

Plane	Long Axis Direction			
	<010>	<011>	<111>	<112>
{001}	172.	172.		

MnS -70 °C

Plane	Long Axis Direction			
	<010>	<011>	<111>	<112>
{001}	169.	188.		

MnSe 135 °C

Plane	Long Axis Direction			
	<010>	<011>	<111>	<112>
{001}	56.	39.		

75MnSe-25MnS 135 °C

Plane	Long Axis Direction			
	<010>	<011>	<111>	<112>
{001}	102.	90.		

50MnSe-50MnS 135 °C

Plane	Long Axis Direction			
	<010>	<011>	<111>	<112>
{001}	130.	127.		

25MnSe-75MnS 135 °C

Plane	Long Axis Direction			
	<010>	<011>	<111>	<112>
{001}	136.	145.		

MnS 135 °C

Plane	Long Axis Direction			
	<010>	<011>	<111>	<112>
{001}	107.	107.		

93MnSe-7MnTe 25 °C

Plane	Long Axis Direction			
	<010>	<011>	<111>	<112>
{001}	101.	83.		
{011}	100.	88.	89.	

87MnSe-13MnTe 25 °C

Plane	Long Axis Direction			
	<010>	<011>	<111>	<112>
{001}	139.	108.		
{011}	132.	126.	128.	

MnTe				91MnTe-9MnSe			
25° C				25° C			
Plane	Long axis direction			Plane	Long axis direction		
	$\langle\bar{1}2\bar{1}0\rangle$	$\langle\bar{1}100\rangle$	$\langle 0001\rangle$		$\langle\bar{1}2\bar{1}0\rangle$	$\langle\bar{1}100\rangle$	$\langle 0001\rangle$
{0001}	113.	118.		{0001}	149.	151.	
{10 $\bar{1}$ 0}	51.		65.	{10 $\bar{1}$ 0}	73.		90.
{11 $\bar{2}$ 0}		53.	64.				

81MnTe-19MnSe			
25° C			
Plane	Long axis direction		
	$\langle\bar{1}2\bar{1}0\rangle$	$\langle\bar{1}100\rangle$	$\langle 0001\rangle$
{0001}	186.	181.	
{10 $\bar{1}$ 0}	95.		107.

Part II. Diamond Pyramid (Vickers) Hardness  
500 gram load

Composition	Plane		
	{001}	{011}	{111}
Pure MnSe	47.	47.	46.
91MnSe-9MnS	79.	84.	85.
75MnSe-25MnS	108.	115.	115.
50MnSe-50MnS	146.	148.	148.
25MnSe-75MnS	165.	169.	169.
Pure MnS	144.	144.	146.

Composition	Temperature, ° C		
	-198	-70	135
Pure MnSe	-	50.	43.
91MnSe-9MnS	-	-	-
75MnSe-25MnS	~300	121.	100.
50MnSe-50MnS	~330	156.	131.
25MnSe-75MnS	~270	173.	144.
Pure MnS	207.	187.	105.

25° C

Composition	Plane		
	{001}	{011}	{111}
Pure MnSe	47.	47.	46.
93MnSe-7MnTe	83.	80.	
87MnSe-13MnTe	111.	115.	

25° C

Composition	Plane		
	{0001}	{1010}	{1120}
Pure MnTe	107.	64.	65.
91MnTe-9MnSe	135.	83.	83.
81MnTe-19MnSe	165.	108.	110.

All of these hardness numbers represent an average of at least five readings, and, in most cases, they are the average of ten or more.



## APPENDIX II

### SUMMARY OF KNOOP HARDNESS ANISOTROPY THEORIES

#### 1. DANIELS AND DUNN METHOD

The Daniels and Dunn (1949) procedure has been explained quite extensively in the text. For further reference, the reader is referred to the original article.

#### 2. FENG AND ELBAUM METHOD

The Feng and Elbaum (1958) method is similar to the Daniels and Dunn (1949) method except that a compressive force perpendicular to each facet is assumed to be responsible for most of the deformation occurring during indentation.

#### 3. ONE SHEAR STRESS METHOD

This procedure has also been described extensively in the body of this report but a sample calculation will be included here. A portion of the indenter and the slip line field associated with the indentation of an infinite wedge in an isotropic material is shown in Figure 64. The direction of the assumed shear stress,  $\tau_{xy}$ , is along a line from E to C on this side of the indenter. This direction is labeled "y" and direction "x" is perpendicular to it. Figure 65 is a stereographic projection showing the intersection of the facets of the indenter with the plane of indentation; the directions "x" and "y"; a slip plane normal, N; and a slip direction, D. The shear stress  $\tau_{xy}$ ,

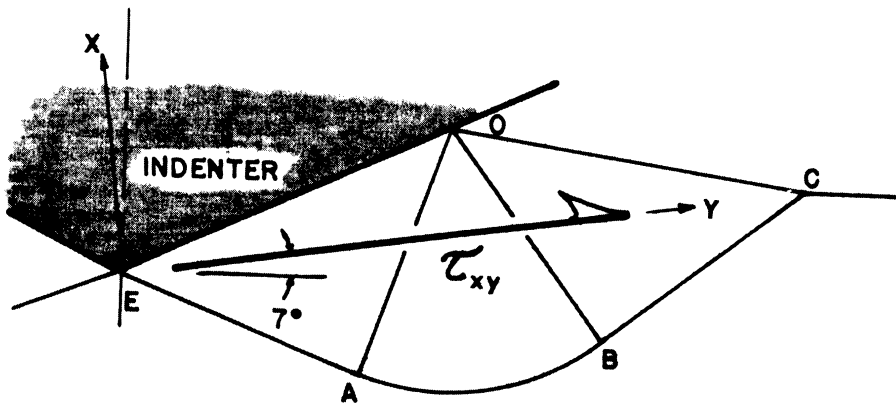


Figure 64. Assumed slip line field around Knoop indenter and direction of shear stress for the "one lateral shear stress" method of calculation.

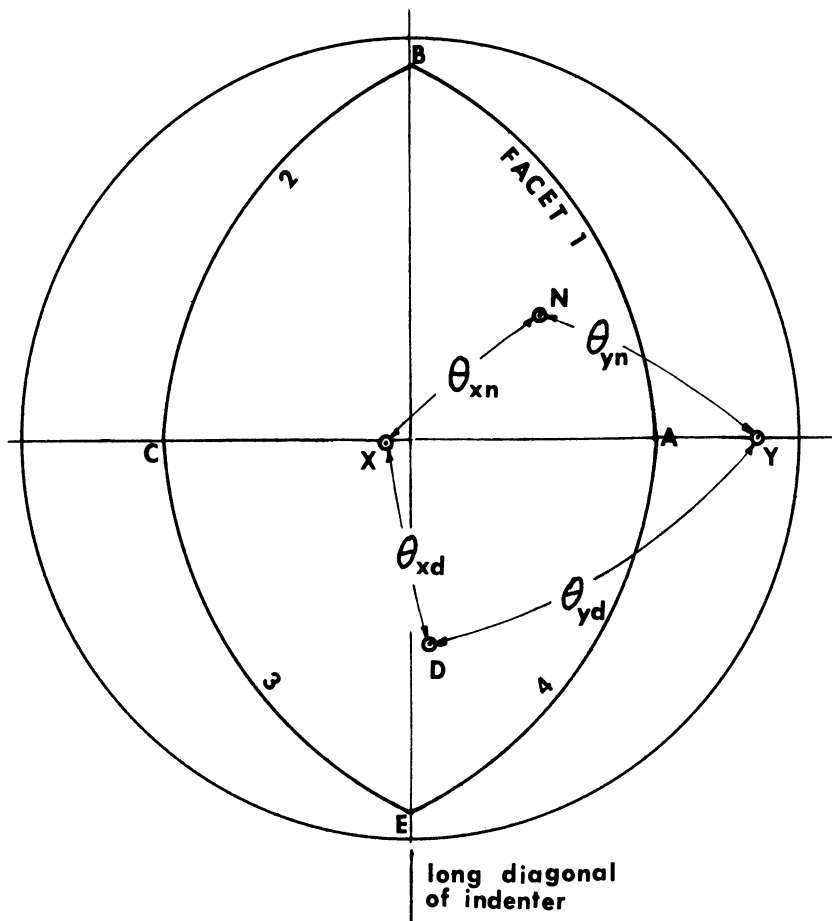


Figure 65. Stereographic projection illustrating calculational procedure for "one lateral shear stress" method.

is resolved in the direction, D, on the plane whose normal is N by the formula:

$$\tau_{ND} = \tau_{xy}(l_{xN}l_{yD} + l_{xD}l_{yN})$$

$$\tau_{ND} = \tau_{xy}(m), \text{ where}$$

$$\tau_{ND} = \text{resolved shear stress}$$

$$l_{xN} = \text{cosine of the angle between the "x"-axis and the normal to the slip plane}$$

$$l_{yD} = \text{cosine of the angle between the "y"-axis and the slip direction, etc.}$$

For this hypothetical case:

$$\theta_{xN} = 54^\circ$$

$$\theta_{yD} = 82^\circ$$

$$\theta_{xD} = 55^\circ$$

$$\theta_{yN} = 51^\circ$$

$$\tau_{ND} = \tau_{xy}(0.425)$$

$$\therefore m = 0.425$$

This factor was calculated for all the slip systems of a given type at each particular indenter orientation and the maximum "m"-value at each orientation was assumed to be inversely proportional to the hardness.

#### 4. TWO SHEARS METHOD

In this procedure, two shear stresses,  $\tau_{x_1y_1}$  and  $\tau_{x_2y_2}$  shown in Figure 66, were assumed to be primarily responsible for the deformation associated with the indenter. These stress directions are shown in stereographic projection for facet 1 in Figure 67. Each facet was assumed to be one side of an in-

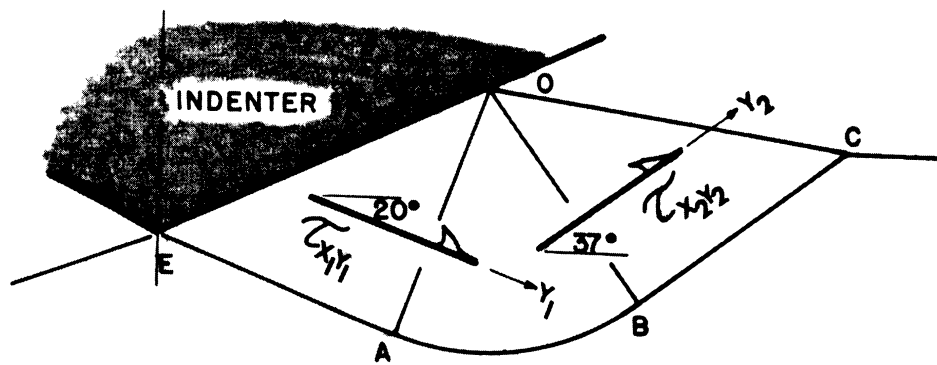


Figure 66. Assumed slip line field around Knoop indenter and directions of shear stress for the "two shears" method of calculation.

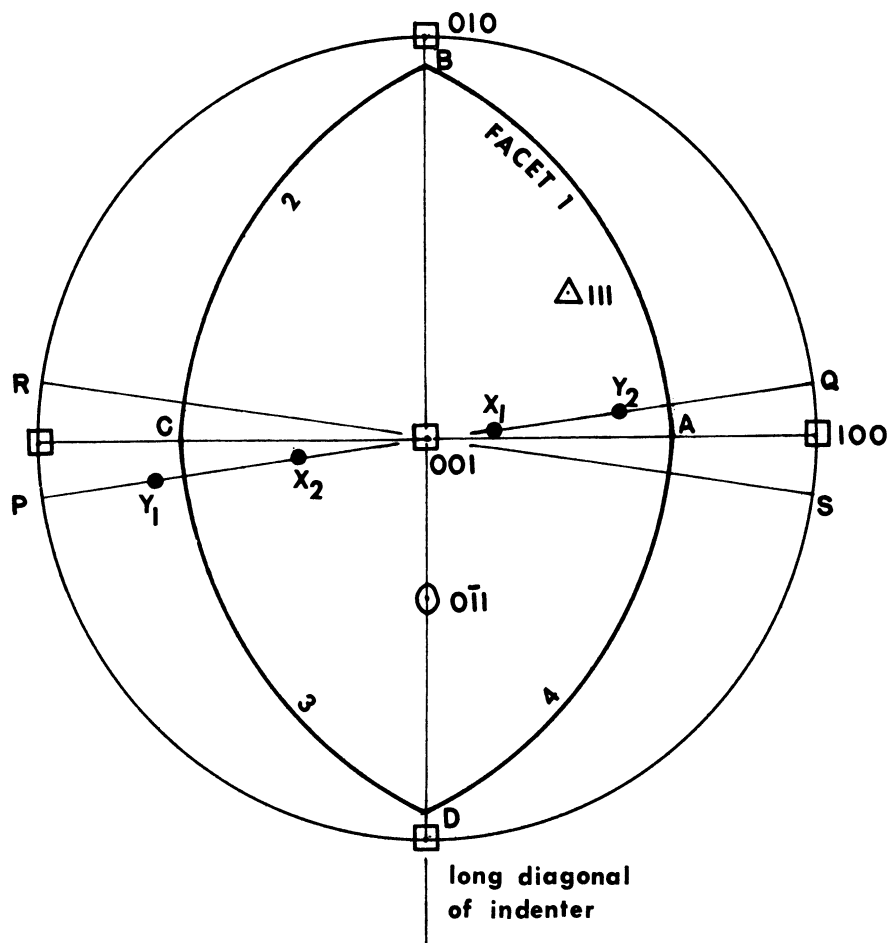


Figure 67. Stereographic projection illustrating the calculational procedure for "two shears" method for the  $(111)[\bar{0}11]$  slip system when the long axis of the indenter is in the  $[010]$  direction on the  $(001)$  plane.

finite wedge with a slip line field associated with it.

A sample calculation will be performed for the slip system  $(111)[0\bar{1}1]$  for an indentation on the  $(001)$  plane with the long axis of the indenter in the  $[010]$  direction.

$$\begin{aligned} \tau_{x_1y_1}: \quad \tau_{ND} &= \tau_{x_1y_1} (\ell_{x_1N} \ell_{y_1D} + \ell_{x_1D} \ell_{y_1N}) \\ &= \tau_{x_1y_1} (0.766)(0.342) + (-0.407)(0.629) \\ &= \tau_{x_1y_1} (0.006) \end{aligned}$$

$$\begin{aligned} \tau_{x_2y_2}: \quad \tau_{ND} &= \tau_{x_2y_2} (\ell_{x_2N} \ell_{y_2D} + \ell_{x_2D} \ell_{y_2N}) \\ &= \tau_{x_2y_2} (0.078)(0.342) + (0.866)(0.629) \\ &= \tau_{x_2y_2} (0.571) \end{aligned}$$

At this particular indenter orientation the largest value of "m" for the downward stress,  $\tau_{x_1y_1}$ , happens to occur on the system  $(\bar{1}\bar{1}1)[011]$  ( $m = 0.614$ ) and for the upward stress,  $\tau_{x_2y_2}$ , on the system  $(111)[10\bar{1}]$  ( $m = 0.842$ ). Thus the hardness is proportional to:

$$\frac{1}{2} (1/m_1 + 1/m_2) = \frac{1}{2} (1/0.614 + 1/0.842) = 1.408 .$$

In this procedure, any effects associated with the fan-shaped region of the slip line field, OAB, were completely neglected. It may be shown by means of a hodograph, however, that about half the work done in deforming an isotropic material takes place in this region. A hodograph is a vectorial plot of velocities of indenter and material as it deforms.

The stress perpendicular to the side of the indenter along OE (Figure 68) happens to be  $4k$  where  $k$  is the yield stress, assuming an isotropic, nonstrain hardening material. The force per unit length,  $F_{\perp}$ , is  $P(\overline{OE})$ . This force resolved in a vertical direction is the force the indenter encounters as it moves downward with velocity  $V_I$  (Figure 69). The rate of work done on the indenter as it moves downward is:

$$F_y V_I = V_I(4k)(\overline{OE}) \cos 25^\circ .$$

This equals the sum of the work done on the material by the indenter in the three portions of the slip line field, OEA, OAB, and OBC.

$$\begin{aligned} F_y V_I &= \sum_i k V_i^* \bar{i} \\ &= k[V_{EA}^* \overline{EA} + V_{BC}^* \overline{BC} + \text{work in region OAB}] \end{aligned}$$

now

$$V_{EA}^* \overline{EA} = V_{BC}^* \overline{BC}$$

and, by the law of sines,

$$\frac{V_{EA}^*}{\sin 65^\circ} = \frac{V_I}{\sin 45^\circ}$$

$$\therefore V_{EA}^* = V_I (\sin 65^\circ) \sqrt{2}$$

and,

$$\overline{EA} = \frac{\overline{EO}}{\sqrt{2}}$$

$$\frac{\text{work on leg } \overline{EA}}{\text{total work}} = \frac{k(V_I \sin 65^\circ \sqrt{2}) \frac{\overline{EO}}{\sqrt{2}}}{4k(V_I \cos 25^\circ) \overline{EO}} = 0.25 .$$

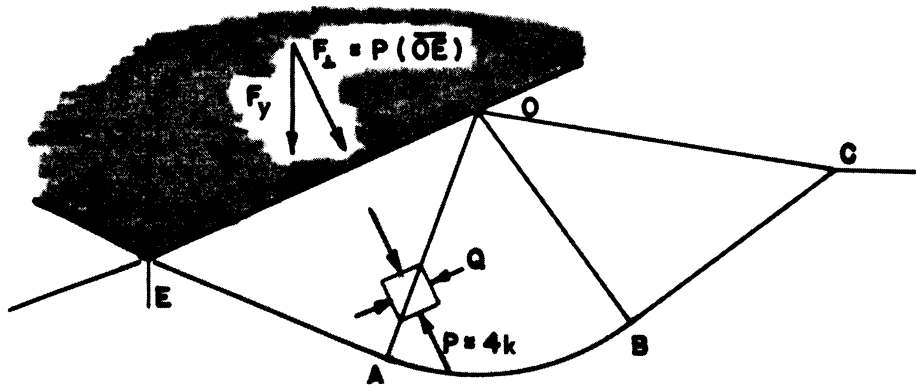


Figure 68. Diagram of slip line field to be used as an aid for calculating the work done in indenting an isotropic material with an infinite wedge.

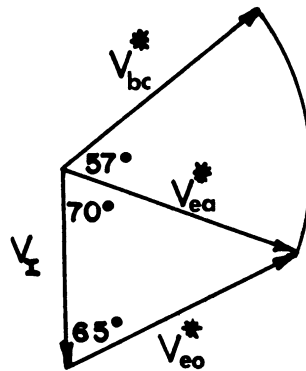


Figure 69. Hodograph for the indentation of an isotropic material by an infinite wedge of included angle 130 degrees.

Therefore,  $1/4$  of the work is done in region OAE,  $1/4$  in OBC, leaving  $1/2$  in the fan-shaped region OAB.

#### 5. INTEGRATED AVERAGE METHOD

It was felt that a better analytical description of the deformation would be obtained if an average  $1/m$  value could be computed for this center region of the slip line field and weighted with the results from the shears  $\tau_{x_1y_1}$  and  $\tau_{x_2y_2}$  as found in the "two shears" method. Accordingly, the directions of principal shear stress were rotated between EA and BC and the stresses resolved at 10 degree intervals during the rotation. At each position the minimum  $(1/m)$  value was found. A plot of  $(1/m)_{\min}$  vs. angle of rotation  $\theta$  is shown in Figure 70 for  $\{111\}\langle\bar{1}\bar{1}0\rangle$  slip and for the indenter in  $[010]$  on  $(001)$ . Each continuous curve represents the variation of  $(1/m)$  with  $\theta$  for one slip system. An average value over this region was calculated by a graphical integration and weighted with the results of the "two shears" method as:

$$(1/m)_{\text{equiv}} = \frac{1}{4} (1/m_{\text{EA}})_{\min} + \frac{1}{4} (1/m_{\text{BC}})_{\min} + \frac{1}{2} (1/m_{\theta})_{\text{aver}}$$

which was then taken as proportional to the hardness. In this case,

$$(1/m_{\theta})_{\text{aver}} = 1.670 \text{ and } (1/m)_{\text{equiv}} = 1.539.$$



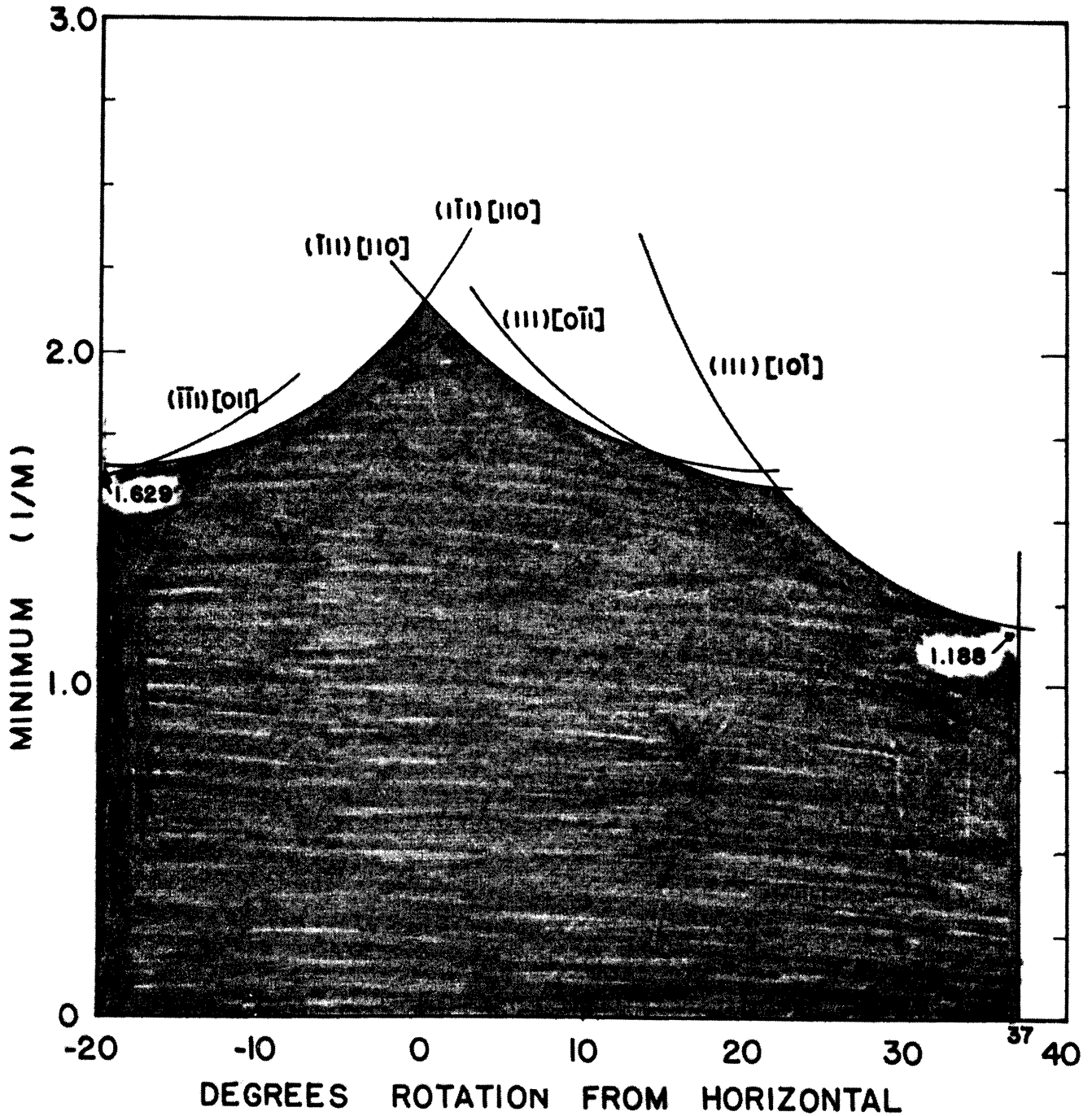


Figure 70. Plot of the minimum ( $1/m$ ) vs. orientation of shear stress for the "integrated average" method when the long axis of the indenter is in the  $[010]$  direction on the  $(001)$  plane. The particular slip system responsible for the minimum value in a particular region is identified. An average value was found over the 57 degree rotation by means of a graphical integration.

## APPENDIX III

### OTHER SYSTEMS INVESTIGATED

At the onset of this investigation, several solid solution systems were selected as showing potential for a deformation study. The growth of single crystals was attempted for almost all these systems but several failed to give satisfactory results. These are listed as follows:

#### 1. MnTe-MnS SYSTEM

The MnTe-MnS system, shown in Figure 5, shows such limited single phase regions that no single crystals, other than of the pure end members, could be grown.

#### 2. MnSe-FeSe SYSTEM

Kiessling et al. (1967) have found that Fe may replace up to 42 percent of the Mn atoms in MnSe at 1150°C. It was therefore hoped that the solid solubility at room temperature would be large enough to allow single crystals of one or two compositions to be grown in the single phase region. Powders of Mn, Fe, and Se were blended, placed in graphite crucibles, sealed in vycor under vacuum, and reacted at 700°C to give material of compositions 92 w/o MnSe-8 w/o FeSe, and 85 w/o MnSe-15 w/o FeSe. Some of the reacted material was placed in another graphite crucible, sealed in fused silica tubing under vacuum, and lowered slowly through an induction coil, bypassing the zone refining step just to see if the process used with MnSe and MnTe was feasible here. It was anticipated that there would be a strong tendency to form iron carbide. Ap-

parently iron carbide did form, releasing selenium which has a high vapor pressure at 1500°C, approximately the temperature used in this run. The silica tube could not hold this pressure and exploded. The compound FeSe is thus not as stable as MnSe.

Another run was attempted using an alumina crucible rather than graphite. The alumina crucible reacted extensively with the selenium in the charge, and, after a short time, the fused silica capsule shattered again.

As a result, this system was abandoned.

### 3. MnSe-CrSe SYSTEM

Kiessling et al. (1967) found that Cr may replace up to 47 percent of the Mn atoms in MnSe. Powders of Mn, Cr, and Se were mixed and reacted at 700°C in a graphite crucible sealed in vycor to give compositions of 92 w/o MnSe-8 w/o CrSe, and 85 w/o MnSe-15 w/o CrSe. When attempts were made to grow single crystals, the fused silica tube again exploded.

It is felt that single crystals in the above two systems could be grown in a high pressure chamber utilizing argon or some inert gas at 150 to 200 atmospheres pressure. This, however, would have required extensive and costly construction and revision of equipment which was not deemed appropriate at this time.

### 4. MnS-FeS SYSTEM

Iron sulfide, FeS, was prepared by reacting sulfur with high purity iron wire in an evacuated pyrex tube but no attempt was made to grow single crystals because of the explosions encountered in the previous two cases.

## 5. MnS-CrS SYSTEM

Attempts were made to manufacture CrS as a raw material by reacting stoichiometric amounts of sulfur and chromium powders. Some of the sulfur did react with the chromium, but much of it would not react even over long periods of time at 500°C (e.g., a week or more).

## REFERENCES

- AMELINCKX, S. (1958) "The Nucleation of Dislocation Loops During Cleavage," Phil. Mag., 3, p. 653.
- ARGON, A. S. and E. OROWAN (1964) "Plastic Deformation in MgO Single Crystals," Phil. Mag., 9, p. 1003.
- ASHBEE, K.H.G. and R. E. SMALLMAN (1963) "Stress-Strain Behavior of Titanium Dioxide (Rutile) Single Crystals," J. Am. Cer. Soc., 46, p. 211.
- BAILEY, S. W., R. A. BELL and C. J. PENG (1958) "Plastic Deformation of Quartz in Nature," Geol. Soc. of Am. Bull., 69, p. 1443.
- BAKARIAN, P. W. and C. H. MATHEWSON (1943) Trans. AIME, 152, p. 226.
- BANEWICZ, J. J. and R. LINDSAY (1956) "Magnetic Susceptibility of  $\alpha$ -MnS," Phys. Rev., 104, p. 318.
- BANEWICZ, J. J., R. F. HEIDELBERG and A. H. LUXEM (1961) "High Temperature Magnetic Susceptibilities of MnO, MnSe and MnTe," J. Phys. Chem., 65, p. 615.
- BARONI, Di A. (1938) "Kürzere Originalmitteilungen und Notizen," Zeit. Krist., A99, p. 336.
- BARRETT, C. S. (1952) Structure of Metals, McGraw-Hill Co., Inc., New York.
- BIZETTE, H., C. F. SQUIRE and TSAI (1938) "Le Point de Transition  $\lambda$  de la Susceptibilité Magnétique du Protoxyde de Manganese, MnO," Compt. Rend., 207, p. 449.
- BLITZ, W. and W. KLEMM (1933) "Die Unterteilung der Reihen der Übergangselemente," Zeit. Elektrochemie, 39, p. 597.
- BRIDGMAN, P. W. (1947) "The Effect of Hydrostatic Pressure on the Fracture of Brittle Substances," J. Appl. Phys., 18, p. 246.
- BRIDGMAN, P. W. (1952) Studies in Large Plastic Flow and Fracture, McGraw-Hill Co., Inc., New York.
- BÜCKLE, H. (1954) "Investigation of the Load Dependence of Vickers Micro-hardness, Part II," Zeit. Metallkunde, 45, p. 694.

- BÜCKLE, H. (1959) "Progress in Micro-Indentation Hardness Testing," Met. Rev., 4, p. 49.
- BUERGER, M. J. (1935) "Translation Gliding in Crystals of the NaCl Structure Type," Am. Mineral., 15, p. 21.
- BURN, R. and G. T. MURRAY (1962) "Plasticity and Dislocation Etch Pits in CaF<sub>2</sub>," J. Am. Cer. Soc., 45, p. 251.
- CHAO, H. C., Y. E. SMITH and L. H. VAN VLACK (1963) "The MnO-MnS Phase Diagram," Trans. AIME, 227, p. 796.
- CHAO, H. C., L. THOMASSEN and L. H. VAN VLACK (1964a) "Deformation and Fracture of MnS Crystals," ASM Trans. Quart., 57, p. 386.
- CHAO, H. C., L. H. VAN VLACK, F. OBERIN and L. THOMASSEN (1964b) "Hardness of Inclusion Sulfides," ASM Trans. Quart., 57, p. 885.
- CLASS, W., E. S. MACHLIN and G. T. MURRAY (1959) "Sodium Chloride Embrittlement by Surface Compound Formation," J. Metals, 11, p. 583.
- COBLENTZ, W. W. (1903) "Note on the Bending of Rock Salt," Phys. Rev., 16, p. 389.
- CONRAD, H. (1965) "Mechanical Behavior of Sapphire," J. Am. Cer. Soc., 48, p. 195.
- COTTRELL, A. H. (1953) Dislocations and Plastic Flow in Crystals, Clarendon Press, Oxford.
- COTTRELL, A. H. (1958) "Theory of Brittle Fracture in Steels and Similar Metals," Trans. AIME, 212, p. 192.
- DANIELS, F. W. and C. G. DUNN (1949) "The Effect of Orientation on Knoop Hardness of Single Crystals of Zinc and Silicon Ferrite," Trans. AIME, 41, p. 419.
- DE BOER, J. H. and E.J.W. VERWEY (1937) "Semiconductors with Partially and Completely Filled 3d Lattice Bands," Proc. Physical Soc., 49 (extra part), p. 59.
- DIETER, G. E. (1961) Mechanical Metallurgy, McGraw-Hill Co., Inc., New York.
- DURAND, M. A. (1936) "The Temperature Variation of the Elastic Modulus of NaCl, KCl and MgO," Phys. Rev., 50, p. 449.

- ESHELBY, J. D., C.W.A. NEWBY, P. L. PRATT and A. B. LIDIARD (1958) "Charged Dislocations and the Strength of Ionic Crystals," Phil. Mag., 3, p. 75.
- FENG, C. and C. ELBAUM (1958) "Effect of Crystallographic Orientation and Oxygen Content on Knoop Hardness Values of Iodide Titanium," Trans. AIME, 212, p. 48.
- FRANK, F. C. and W. T. READ (1950) "Multiplication Processes for Slow Moving Dislocations," Phys. Rev., 79, p. 722.
- FURBERG, S. (1953) "On the System Mn-Te," Acta Chemica Scandinavica, 7, p. 693.
- GALT, J. K. (1948) "Mechanical Properties of NaCl, KBr and KCl," Phys. Rev., 73, p. 1460.
- GARFINKLE, M. and R. G. GARLICK (1967) "A Stereographic Representation of Knoop Hardness Anisotropy," NASA Technical Note NASA TN-D-4226, Lewis Research Center.
- GENERAL ELECTRIC COMPANY (1964) Fused Quartz Catalog.
- GILMAN, J. J. (1957) "Nucleation of Dislocation Loops by Cracks in Crystals," Trans. AIME, 209, p. 1449.
- GILMAN, J. J. and D. W. STAUFF (1958) "Nucleation of Dislocations Accompanying Electric Breakdown in Lithium Fluoride Crystals," J. Appl. Phys., 29, p. 120.
- GILMAN, J. J. (1959a) "Plastic Anisotropy of LiF and Other Rock-Salt Type Crystals," Acta Met., 7, p. 608.
- GILMAN, J. J. (1959b) "Dislocation Sources in Crystals," J. Appl. Phys., 30, p. 1584.
- GILMAN, J. J. (1961a) "Mechanical Behavior of Ionic Crystals," Progress in Ceramic Science, Vol. 1, J. E. Burke, Ed., Pergamon Press, New York, p. 146.
- GILMAN, J. J. (1961b) "Reduction of Cohesion in Ionic Crystals by Dislocations," J. Appl. Phys., 32, p. 738.
- GILMAN, J. J. (1963) "Strength of Ceramic Crystals," Mechanical Behavior of Crystalline Solids, NBS Monograph 59, p. 79.
- GORUM, A. E., E. R. PARKER and J. A. PASK (1958) "Effect of Surface Conditions on Room Temperature Ductility of Ionic Crystals," J. Am. Cer. Soc., 41, p. 161.

- GRAZHDANKINA, N. P. and D. I. GURFEL (1958) "X-Ray Diffraction Study of the Thermal Expansion of Antiferromagnetic MnTe," Soviet Phys. JETP, 35, p. 907.
- GREELAND, K. M. (1937) "Slip Bands on Mercury Single Crystals," Proc. Roy. Soc. (London), A163, p. 28.
- GREENWALD, S. (1953) "The Antiferromagnetic Structure Deformation in CoO and MnTe," Acta Cryst., 6, p. 396.
- GRIFFITH, A. A. (1921) "The Phenomena of Rupture and Flow in Solids," Phil. Trans. (London), A221, p. 163.
- GROVES, G. W. and A. KELLY (1963) "Independent Slip Systems in Crystals," Phil. Mag., 8, p. 877.
- HANSEN, M. (1958) Constitution of Binary Alloys, McGraw-Hill Co., Inc., New York.
- HILL, R., E. H. LEE and S. J. TUPPER (1947) "The Theory of Wedge Indentation of Ductile Materials," Proc. Roy. Soc. (London), A188, p. 273.
- HILL, R. (1950) The Mathematical Theory of Plasticity, Clarendon Press, Oxford.
- HOLLOX, G. E. and R. E. SMALLMAN (1966) "Plastic Behavior of Titanium Carbide," J. Appl. Phys., 37, p. 818.
- HUNTER, L. and S. SIEGEL (1942) "The Variation with Temperature of the Principal Elastic Moduli of NaCl Near the Melting Point," Phys. Rev., 61, p. 84.
- JOFFE, A., M. W. KIRPITSCHewa and M. A. LEWITSKY (1924) "Deformation und Festigkeit der Kristalle," Zeit. Phys., 22, p. 286.
- JOHANSEN, H. A. (1958) "The Stoichiometry of MnTe," J. Inorg. and Nucl. Chem., 6, p. 344.
- JOHNSON, L. D. and J. A. PASK (1964) "Mechanical Behavior of Single Crystal and Polycrystalline Cesium Bromide," J. Am. Cer. Soc., 47, p. 437.
- JOHNSTON, T. L., R. J. STOKES and C. H. LI (1962) "Crack Nucleation in Magnesium Oxide Bi-Crystals Under Compression," Phil. Mag., 7, p. 23.
- JOHNSTON, T. L. (1963) "Fracture Mechanisms in Crystalline Ceramics," Mechanical Behavior of Crystalline Solids, NBS Monograph 59, p. 63.
- JOHNSTON, T. L. and E. R. PARKER (1963) "Fracture of Nonmetallic Crystals," Fracture of Solids, John Wiley and Sons, New York.



- JOHNSTON, W. D. and D. E. SESTRICH (1961) "The MnTe-GeTe Phase Diagram," J. Inorg. and Nucl. Chem., 19, p. 229.
- JOHNSTON, W. G. and J. J. GILMAN (1959) "Dislocation Velocities, Dislocation Densities and Plastic Flow in Lithium Fluoride Crystals," J. Appl. Phys., 30, p. 129.
- JOHNSTON, W. G. and J. J. GILMAN (1960) "Dislocation Multiplication in Lithium Fluoride Crystals," J. Appl. Phys., 31, p. 632.
- KEAR, B., A. TAYLOR and P. PRATT (1959) "Some Dislocation Interactions in Simple Ionic Crystals," Phil. Mag., 4, p. 665.
- KEH, A. S., J.C.M. LI and Y. T. CHOU, (1959) "Cracks Due to Piling-Up of Dislocations on Two Intersecting Slip Planes in MgO Crystals," Acta Met., 7, p. 694.
- KEH, A. S. (1960) "Dislocations in Indented Magnesium Oxide Crystals," J. Appl. Phys., 31, p. 1538.
- KELLY, K. K. (1939) "Specific Heats at Low Temperature of Manganese, Manganous Selenide and Manganous Telluride," J. Am. Chem. Soc., 61, p. 203.
- KIESSLING, R. and C. WESTMAN (1966) "Sulfide Inclusions and Synthetic Sulfides of the (Mn, Me)S Type," J. Iron and Steel Inst., 204, p. 377.
- KIESSLING, R., B. HASSLER and C. WESTMAN (1967) "Selenide-Sulfide Inclusions and Synthetic Compounds of the (Mn, Me)(S, Se) Type," J. Iron and Steel Inst., 205, p. 531.
- KITTLE, C. (1957) Introduction to Solid State Physics, John Wiley and Sons, New York.
- KLASSEN, M. V. and NEKLYNDOVA (1942) "Plastic Deformation of Synthetic Corundum," Soviet Phys. JETP, 12, p. 519.
- KOEHLER, J. E. (1952) "The Nature of Work Hardening," Phys. Rev., 86, p. 52.
- KOLSKY, H. (1957) "Some Aspects of Mechanical Testing of Nonmetallic Solids and the Physics of Non-Destructive Testing," Brit. J. Appl. Phys., Supp. 6, p. 1.
- KRIEGE, O. H. and M. L. THEODORE (1966) "Analysis of Rare Earth Sulfides, Selenides and Tellurides," Talanta, 13, p. 265.
- KRONBERG, M. L. (1957) "Plastic Deformation of Single Crystals of Sapphire - Basal Slip and Twinning," Acta Met., 5, p. 507.

- KUZNETSOV, V. D. (1957) Surface Energy of Solids, Trans. from the Russian, Her Majesty's Stationery Office, London.
- LINDSAY, R. (1951) "Magnetic Susceptibility of MnSe," Phys. Rev., 84, p. 569.
- LOW, J. R. (1963) "Microstructural Aspects of Fracture," Fracture of Solids, John Wiley and Sons, New York.
- LYNCH, J. F. and C. G. RUDERER (1966) Engineering Properties of Selected Ceramic Materials, Am. Ceramic Soc., Columbus, Ohio.
- LYSAGHT, V. E. (1949) Indentation Hardness Testing, Reinhold, New York.
- MAKOVETSKI, G. I. and N. N. SIROTA (1963) "A Dilatometric Study of Manganese Selenide," Dokl. Akad. Nauk. BSSR, 7 p. 740. Also, Selenium and Tellurium Abstracts #1896 (1964).
- MAKOVETSKI, G. I. and N. N. SIROTA (1964) "An X-Ray Investigation of the Quasi-Binary System MnSe-MnTe," Dokl. Akad. Nauk. BSSR, 8, p. 289. Also, Selenium and Tellurium Abstracts #2701 (1965).
- MAKOVETSKI, G. I. and N. N. SIROTA (1965) "Electrical Conductivity, Electromotive Force and Energy Gap in Alloys of MnSe and MnTe," Dokl. Akad. Nauk. BSSR, 9, p. 85. Also, Chem. Abstracts #113C (1965).
- MAKOVETSKI, G. I. and N. N. SIROTA (1966) "Neutron Diffraction Examination of MnSe," Dokl. Akad. Nauk. BSSR, 10, p. 542. Also, Selenium and Tellurium Abstracts #5853 (1967).
- MARSH, D. M. (1963) "Flow and Fracture in Glass," Fracture of Solids, John Wiley and Sons, New York.
- MEBS, R. W. (1949) Written Discussion of Article by Daniels and Dunn (1949), ASM Trans., 41, p. 440.
- MEHTA, J. M., P. G. RIEWALD and L. H. VAN VLACK (1967) "The MnSe-MnS System." J. Am. Cer. Soc., 50, p. 164.
- MELANKHOLIN, N. M. and V. R. REGAL (1956) Soviet Phys. JETP, 2, p. 696.
- MILCH, L. (1909) "The Increase in Plasticity of Crystals with Rise in Temperature," Neues Jahrb. Mineral. Geol. Paläeon., p. 60.
- MILES, G. D. (1964) "Fundamental Mechanisms Influencing the Flow and Fracture of Some Ionic Crystals," Progress in Applied Materials Research, Vol. 5, Temple Press Ltd., London.

- MOORE, J. W. (1965) "Structure and Properties of Oriented Compound Eutectics," Ph.D. Thesis, University of Michigan.
- MOTT, B. W. (1956) Micro-Indentation Hardness Testing, Butterworths, London.
- NABARRO, F.R.N., Z. S. BASINSKI and D. B. HOLT (1964) "Plasticity of Pure Single Crystals," Advances in Physics, Supp. to Phil. Mag., 13, p. 193.
- OROWAN, E. (1954) Dislocations in Metals, AIME, New York.
- PANSON, A. J. and W. D. JOHNSTON (1964) "The MnTe-MnSe System," J. Inorg. and Nucl. Chem., 26, p. 701.
- PARKER, E. R. (1958) "Modern Concepts of Flow and Fracture," Trans. ASM, 58, p. 52.
- PARKER, E. R. (1963) "Plastic Flow and Fracture of Crystalline Solids," Mechanical Behavior of Crystalline Solids, NBS Monograph 59, p. 1.
- PARKER, R. (1958) "Electrical Resistivity of Compounds with Ordered Spin Arrangements," Phil. Mag., 3, p. 853.
- PARTRIDGE, P. G. and E. ROBERTS (1964) "The Microhardness Anisotropy of Magnesium and Zinc Single Crystals," J. Inst. Metals, 92, p. 50.
- PAULING, L. (1948) Nature of the Chemical Bond, Cornell University Press, Ithaca, New York
- PETTY, E. R. (1963) "The Hardness Anisotropy of Aluminum Single Crystals," J. Inst. Metals, 91, p. 54.
- PHILLIPS, W. L. (1961) "Deformation and Fracture Processes in CaF<sub>2</sub> Single Crystals," J. Am. Cer. Soc., 44, p. 499.
- ROESLER, F. C. (1956) "Indentation Hardness of Glass as an Energy Scaling Law," Proc. Roy. Soc. (London), B69, p. 55.
- SCHMID, E. and W. BOAS (1936) Crystal Plasticity, J. Springer, Berlin. Translation, Hughes, London (1950).
- SCHWARTZ, M., S. K. NASH and R. ZEMAN (1961) "Hardness Anisotropy in Single Crystal and Polycrystalline Magnesium," Trans. AIME, 221, p. 554.
- SEITZ (1951) "Speculations on the Properties of the Silver Halide Crystals," Rev. Mod. Phys., 23, p. 328.

- SHULL, C. G., W. A. STRAUSSER and E. O. WOLLAM (1951) "Neutron Diffraction by Paramagnetic and Antiferromagnetic Substances," Phys. Rev., 83, p. 332.
- SLACK, G. A. (1960) "Crystallography and Domain Walls in Antiferromagnetic NiO Crystals," J. Appl. Phys., 31, p. 1571.
- SQUIRE, C. F. (1939) "Antiferromagnetism in Some Manganous Compounds," Phys. Rev., 56, p. 922.
- STEPHANOV, A. V. and I. M. EIDUS (1956) "Temperature Dependence of the Elastic Limits of Monocrystals of NaCl and AgCl," Soviet Phys. JETP, 2, p. 377.
- STEPHANOV, A. W. and V. P. BOBRIKOV (1957) "Dependence of the Optical Elasticity Limits Determined on the Basis of the System (111) [011] Upon Temperature for Rock-Salt Crystals," Soviet Phys. Tech. Phys., 1, p. 777.
- STOKES, R. J., T. L. JOHNSTON and C. H. LI (1958) "Crack Formation in MgO Single Crystals," Phil. Mag., 3, p. 718.
- STOKES, R. J., T. L. JOHNSTON and C. H. LI (1959) "The Relationship Between Plastic Flow and the Fracture Mechanism in Magnesium Oxide Single Crystals," Phil. Mag., 4, p. 920.
- STOKES, R. J., T. L. JOHNSTON and C. H. LI (1960) "Environmental Effects on the Mechanical Properties of Ionic Solids with Particular Reference to the Joffe Effect," Trans. AIME, 218, p. 655.
- STOKES, R. J., T. L. JOHNSTON and C. H. LI (1961) "Effect of Slip Distribution on the Fracture Behavior of Magnesium Oxide Single Crystals," Phil. Mag., 6, p. 9.
- STOKES, R. J. (1962) "Dislocation Sources and the Strength of Magnesium Oxide Single Crystals," Trans. AIME, 224, p. 1227.
- STOKES, R. J. and C. H. LI (1963) "The Anisotropic Extension of Microcracks by Plastic Flow in Semi-Brittle Solids," Fracture of Solids, John Wiley and Sons, New York.
- STROH, A. N. (1954) "The Formation of Cracks as a Result of Plastic Flow," Proc. Roy. Soc. (London), A223, p. 404.
- TABOR, D. (1951) The Hardness of Metals, Clarendon Press, Oxford.
- TAMMANN, G. and W. SALGE (1927) "Octahedral Glide of NaCl at High Temperature, Decrease in Yield Point with Rising Temperature," Neues Jahrb. Mineral., Geol., Paläeon., Supp. 57, p. 117.

- TANNHAUSER, D. S., L. J. BRUNER and A. W. LAWSON (1956) "Temperature Variation of the Elastic Constants of AgBr," Phys. Rev., 102, p. 1276.
- TAYLOR, A. and B. J. KAGLE (1963) Crystallographic Data on Metal and Alloy Structures, Dover Publications, New York.
- TIEN, T. Y., L. H. VAN VLACK and R. J. MARTIN (1967) "The System MnTe-MnS," University of Michigan Office of Research Administration Report 07137-4-P.
- TOLANSKY, S. and D. G. NICKOLS (1949a) "Interferometric Examination of Hardness Test Indentations," Nature, 164, p. 103.
- TOLANSKY, S. and D. G. NICKOLS (1949b) "Interferometric Examination of Hardness Indentations in Tin," Nature, 164, p. 840.
- TOLANSKY, S. and D. G. NICKOLS (1952) "Interferometric Studies of Hardness Test Indentations: Investigations on Tungsten Carbide, Steel, Duraluminum and Tin," Phil. Mag., 43, p. 410.
- TOMBS, N. C. and H. P. ROOKSBY (1950) "Structure of Monoxides of Some Transition Elements at Low Temperatures," Nature, 165, p. 442.
- TOMBS, N. C. and H. P. ROOKSBY (1951) "Changes of Crystal Structure in Antiferromagnetic Compounds," Nature, 167, p. 364.
- VAN DER WALT, C. M. and M. J. SOLE (1967) "On the Plastic Behavior of Crystals with the NaCl Structure," Acta Met., 15, p. 459.
- VAN VLACK, L. H. (1964) Elements of Materials Science, Addison Wesley, Reading, Mass..
- VAN ZEGGEREN, F. and G. C. BENSON (1957) "Calculation of Surface Energies of Alkali Halide Crystals," J. Chem. Phys., 26, p. 1077.
- VAUGH, W. H. and J. W. DAVISSON (1959) "Surface Mobility of Dislocations and the Joffe Effect," Report of NRL Progress, April, p. 5.
- VOGEL, A. I. (1961) A Textbook of Quantitative Inorganic Analysis, Longmans, London, p. 434 and 508.
- VON MISES, R. (1928) "Mechanik der Plastischen Formänderung von Kristallen," Zeit. Angew. Math. Mech., 8, p. 161.
- WACHTMAN, J. B. and L. H. MAXWELL (1954) "Plastic Deformation of Ceramic Oxide Single Crystals, I," J. Am. Cer. Soc., 37, p. 291.

- WACHTMAN, J. B. and L. H. MAXWELL (1957) "Plastic Deformation of Ceramic Oxide Single Crystals, II," J. Am. Cer. Soc., 40, p. 377.
- WACHTMAN, J. B. and L. H. MAXWELL (1959) "Strength of Synthetic Single Crystal Sapphire and Ruby as a Function of Temperature and Oxidation," J. Am. Cer. Soc., 42, p. 432.
- WARRICK, R. J. (1963) "Plastic Deformation of Nonmetallic Phases Within Ductile Metals," Ph.D. Thesis, University of Michigan.
- WASHBURN, J., A. E. GORUM and E. R. PARKER (1959) "Causes of Cleavage Fracture in Ductile Materials," Trans. AIME, 215, p. 230.
- WESTBROOK, J. H. (1958a) "Flow in Rock Salt Structures," WADC Tech. Rpt., 58-304, ASTIA Document AD155651, General Electric Company Research Lab., p. 6.
- WESTBROOK, J. H. (1958b) "Temperature Dependence of Strength and Brittleness of Some Quartz Structures," J. Am. Cer. Soc., 41, p. 433.
- WESTWOOD, A.R.C. (1961) "On the Behavior of Magnesium Oxide Bi-Crystals," Phil. Mag., 6, p. 195.
- WILLIAMS, W. S. and R. D. SCHAAL (1962) "Elastic Deformation, Plastic Flow and Dislocations in Single Crystals of Titanium Carbide," J. Appl. Phys., 33, p. 955.
- WOLFF, G. A. et al., (1958) "Relationships of Hardness, Energy Gap and Melting Point of Diamond Type and Related Structures," Halbleiter und Phosphore, Brunswick, Vieweg.
- WYCKOFF, R.W.G. (1965) Crystal Structures, Vol. I, John Wiley and Sons, New York.



